Master: Mechanical Engineering

Track: Multi-Machine Engineering

---

# 2024.MME.8945

---

## *Improving comminution interactions inside a granulator at GreenCycl B.V. using the Discrete Element Method (DEM)*

*Author:*

R.J.P. Dekker (4599926)

*Supervisors:*

Prof. Dr. Ir. D. L. Schott (Chair)
Dr. Ir. T. Horeman
Dr. B. J. van Straten

June 27, 2024

# List of Figures

# List of Tables

# Nomenclature

| Parameter | Description | Unit |
|---|---|---|
| $A$ | Model parameter | $-$ |
| $A_{CF}$ | Area of crusher fraction | $m^2$ |
| $A_{CONTACT}$ | Normal area of overlap region | $m^3$ |
| $C_{CL}$ | Crack length | $m$ |
| $C_D$ | Drag coefficient | $-$ |
| $C_N$ | Normal damping coefficient | $N * s/m$ |
| $C_{SP}$ | Size parameter | $-$ |
| $C_T$ | Tangential damping coefficient | $N * s/m$ |
| $D$ | Damage | $-$ |
| $D_B$ | Bowl diameter at given cross-section | $m$ |
| $D_F$ | Aperture of feed screen | $cm$ |
| $D_M$ | Outer diameter of mantle at bottom shell | $m$ |
| $D_R$ | Roll diameter | $m$ |
| $D_{MAX,F}$ | Maximum size of feed particles | $m$ |
| $D_{MEAN,F}$ | Mean size of feed particles | $m$ |
| $D_{MIN,F}$ | Minimum size of feed particles | $cm$ or $m$ |
| $D_{MAX,P}$ | Maximum size of produced particles | $cm$ or $m$ |
| $D_{MEAN,P}$ | Mean size of produced particles | $cm$ or $m$ |
| $D_{MIN,P}$ | Minimum size of produced particles | $m$ |
| $D_P$ | Aperture of product screen | $cm$ |
| $D_R$ | Roll diameter | $m$ |
| $E$ | Young's modulus | $N/m^2$ |
| $E_{CS}$ | Specific comminution energy | $J/kg$ or $kWh/tonne$ |
| $E_{EFF}$ | Effective Young's modulus | $N/m^2$ |
| $E_{MAX}$ | Upper truncation value of log-normal distribution | $J/kg$ |
| $E_{NEW}$ | Mass-specific fracture energy after damage | $J/kg$ |
| $E_{OLD}$ | Mass-specific fracture energy before damage | $J/kg$ |
| $E_R$ | Radius of roll | $m$ |
| $E_T$ | Particle specific fracture energy | $J/kg$ |
| $E_{50}$ | Median of mass-specific fracture energy | $J/kg$ |
| $E^*$ | Mass-specific particle fracture energy | $J/kg$ |
| $E_\infty$ | Model parameter of fracture energy distribution model | $J/kg$ |
| $F_C$ | Compressive force between crusher and feed particle | $N$ |
| $F_G$ | Grinding force | $kN$ |
| $F_N$ | Normal force | $N$ |
| $F_{RR}$ | Radius of roll | $m$ |
| $F_S$ | Specific grinding force | $N/mm^2$ |
| $F_T$ | Tangential force | $N$ |
| $F_{80}$ | 80% passing size of feed | $\mu m$ or $cm$ |
| $F_{G,H}$ | Horizontal component of grinding force | $N$ |
| $H_C$ | Vertical length of crushing chamber | $m$ |
| $I$ | Required crusher Amperage | $A$ |
| $K_N$ | Normal stiffness | $N/m$ |
| $K_T$ | Tangential stiffness | $N/m$ |
| $L_G$ | Gap(e) size | $m$ |
| $L_R$ | Distance between rolls | $m$ |
| $L_R$ | Roll face length | $m$ |
| $L_S$ | Crusher set | $m$ |
| $L_T$ | Crusher throw | $m$ |
| $L_{MAX,C}$ | Maximum distance between crushing head and concave | $m$ |
| $L_{MAX,S}$ | Maximum set distance | $m$ |
| $L_{MIN,C}$ | Minimum distance between crushing head and concave | $m$ |

| | | |
|---|---|---|
| $L_{MIN,S}$ | Minimum set distance | $m$ |
| $M$ | Moment of torque | $Nm$ |
| $N$ | Amount of cycles per minute | $-$ |
| $P$ | Power | $W$ or $kW$ |
| $P_A$ | Actual crusher power draw | $kW$ |
| $P_C$ | Test sieve mesh size | $\mu m$ |
| $P_i$ | Breakage probability of particles of size $i$ | $-$ |
| $P_K$ | Packing characteristics | $-$ |
| $P_N$ | Crusher power draw during no load | $kW$ |
| $P_P$ | Pendulum power draw | $kW$ |
| $P_0$ | Cumulative distribution | $-$ |
| $P_{80}$ | 80% passing size of product | $\mu m$ or $cm$ |
| $Q$ | Crusher capacity | $m^3/hour$ or $tonnes/hour$ |
| $Q_{CR}$ | Comparative reduction | $tonnes/hour$ |
| $Q_F$ | Feed rate | $tonnes/hour$ |
| $Q_H$ | Crusher capacity at high frequencies | $m^3/hour$ |
| $Q_L$ | Crusher capacity at low frequencies | $m^3/hour$ |
| $Q_M$ | Maximum crusher capacity | $tonnes/hour$ |
| $Q_O$ | Optimum crusher capacity | $m^3/s^2$ |
| $Q_R$ | Crusher reduction | $tonnes/hour$ |
| $Q_S$ | Specific throughput | $tonnes/hour$ |
| $Q_V$ | Volumetric crusher capacity | $m^3/hour$ |
| $R$ | Reduction ratio | $-$ |
| $R_{DISK}$ | Effective disk radius | $m$ |
| $Re$ | Reynolds number | $-$ |
| $R_F$ | Ribbon factor | $-$ |
| $R_i$ | Distance from rolling point to center of mass | $m$ |
| $R_R$ | Radius of roll | $m$ |
| $R_{80}$ | Reduction ratio of 80% passing size | $-$ |
| $R^*$ | Effective radius | $m$ |
| $S_i$ | The lower limit of the $i$th fraction | $\mathrm{\mu}m$ |
| $S_{i+1}$ | The upper limit of the $i$th fraction | $\mathrm{\mu}m$ |
| $S_T$ | Tangential stiffness | $N/m$ |
| $T$ | Torque | $Nm$ |
| $W_A$ | Width of crushing aperture | $m$ |
| $W_{CC}$ | Width of the crushing cavity | $m$ |
| $W_J$ | Width of the jaw plates | $m$ |
| $W_I$ | Work index | $kWh/tonne$ |
| $W_R$ | Roll width | $m$ |
| $X_S$ | Crusher set | $cm$ |
| $X_0$ | Average particle outer diameter before crushing | $m$ |
| $X_1$ | Average particle outer diameter after crushing | $m$ |
| $a$ | Acceleration due to gravity | $m/s^2$ |
| $b$ | Model parameter | $-$ |
| $d_j$ | Representative particle of size class $j$ | $-$ |
| $d_0$ | Model parameter | $-$ |
| $f$ | Drag function | $-$ |
| $g$ | Gravity constant | $m/s^2$ |
| $h$ | Particle distance travelled | $m$ |
| $m_i$ | Mass flow of particles of size $i$ | $tonnes/hour$ |
| $m_s$ | Mass passing through screen per mill rotation | $gram/rotation$ |
| $p_{AVE}$ | Average mutual particle pressure | $N/m^2$ |
| $p_{MAX}$ | Maximum pressure | $kN/m^2$ |
| $p_O$ | Operating pressure | $kN/m^2$ |
| $t$ | Time | $s$ |
| $t_i$ | The $i$th element of a size distribution | $\mathrm{\mu}m$ |

| | | |
|---|---|---|
| $t_{10}$ | Proportion of material with 1/10th of parent particle size | $-$ |
| $v$ | Crusher frequency | *cycles per minute* or $1/s$ |
| $v_c$ | Critical crusher frequency | *rotations per minute* |
| $v_{FW}$ | Angular velocity crusher flywheel | $1/s$ |
| $v_{OPT}$ | Optimal crusher speed | *rotations per minute* |
| $v_P$ | Speed at circumference of roll | $m/s$ |
| $\alpha_N$ | Nip angle | $-$ |
| $\beta$ | Reduction ratio | $-$ |
| $\delta_N$ | Normal displacement | $m$ |
| $\dot{\delta}_N$ | Time derivative of normal displacement | $m/s$ |
| $\delta_T$ | Tangential displacement | $m$ |
| $\dot{\delta}_T$ | Time derivative of tangential displacement | $m/s$ |
| $\varepsilon$ | Efficiency factor | $-$ |
| $\gamma$ | Damage accumulation coefficient | $-$ |
| $\gamma_S$ | Free surface energy per unit area | $-$ |
| $\mu$ | Coefficient of friction | $-$ |
| $\mu_K$ | Kinetic coefficient of friction | $-$ |
| $\mu_R$ | Rolling friction coefficient | $-$ |
| $\mu_S$ | Static coefficient of friction | $-$ |
| $\phi$ | Model parameter | $-$ |
| $\psi$ | Angular displacement | $-$ |
| $\rho_B$ | Bulk density of material | $tonnes/m^3$ |
| $\rho_C$ | Material density inside gap | $tonnes/m^3$ |
| $\rho_S$ | Material density | $kg/m^3$ |
| $\rho_{B(F)}$ | Feed bulk density | $tonnes/m^3$ |
| $\rho_{OP}$ | Operational density | $tonnes/m^3$ |
| $\sigma$ | Standard deviation of mass-specific particle fracture energy | $J/kg$ |
| $\tau_i$ | Torque | $Nm$ |
| $\theta_C$ | Inclination angle of the cone | $-$ |
| $\theta_{IP}$ | Inter-particle breakage nip angle | $-$ |
| $\theta_N$ | Nip angle | $-$ |
| $\theta_{SP}$ | Single-particle breakage nip angle | $-$ |
| $\omega$ | Angular velocity | $rad/s$ or *rotations per minute* |
| $\omega_i$ | Angular velocity at contact point | $rad/s$ |

** Please note that the nomenclature utilized in this thesis encompasses not only standard SI-units but also non-standardized units. This decision is informed by reviewed literature, which suggests that for certain scenarios involving small particle sizes combined with high mass flow rates and power consumptions in comminution interactions, the use of non-standardized units can offer advantages over strict adherence to standardized units. Therefore, readers are encouraged to keep this flexibility in mind when referring to the nomenclature throughout this work.*

*** In this thesis, various factors and constants appear. These are marked with an asterisk and are specific to certain formulas. To prevent confusion, they are not included in the nomenclature but their meaning can be found alongside the respective formulas.*

# Preface

With mixed emotions and a hefty dose of nostalgia, I hereby sign this thesis, the culmination of a long and intensive journey through my academic career. Looking back on the past years at Delft University of Technology, I can proudly say that I have immersed myself in a world of knowledge, challenges, and growth. This education has not only pushed my intellectual boundaries but has also shaped me personally.

Throughout my time at TU Delft, I have experienced many highlights, moments that I cherish and that make my student days unforgettable. It was a period of hard work, but also of valuable friendships, inspiring educators, and extraordinary learning experiences. I am grateful for the opportunities this university has provided me and will always hold the memories of this time in my heart with warmth and appreciation.

As I complete this thesis, I would like to express my gratitude to those who have supported and inspired me during this process. First and foremost, I want to thank my supervisors Dr. ir. T. Horeman and Dr. B.J. van Straten from TU Delft for their expert guidance, critical insights, and invaluable assistance in writing this thesis. Their dedication and feedback have elevated my work to a higher level and helped me articulate my ideas clearly and effectively.

I extend my profound gratitude to Prof. Dr. ir. D.L. Schott, who coached me within the Multi-Machine Engineering track and provided valuable subject matter insights. Her expertise and guidance have played a crucial role in my academic development.

Additionally, I want to express my heartfelt gratitude to Majid el Mortadi and Joost van der Sijp for the trust they placed in me by allowing me to conduct my research at GreenCycl B.V. Their support and involvement enriched my research and stimulated my professional growth.
I am also deeply appreciative of the assistance and contributions of Raïsa Roeplal and Marcel van Benten in writing my report. Their expertise and dedication refined and strengthened my work.

Finally, I want to thank my parents for their unwavering support throughout my entire academic journey. Their encouragement and belief in me have guided me through the toughest moments and have given me the strength to persevere, even when the challenges seemed overwhelming.

This is not only the end of an academic journey but also the beginning of a new chapter full of possibilities and adventures. As I turn this page, I bid farewell to my student days with gratitude but also with excitement for what the future holds.

# Abstract

This research delves into the granulator performance within the operational framework of GreenCycl B.V. The study encompasses multiple facets, beginning with an exploration of the factors influencing particle breakage. It elucidates the impact of particle size, material properties, and other pertinent variables on particle fragmentation, alongside an exposition of various mechanisms of particle breakage.

Subsequently, the investigation extends to evaluating the effect of different crushers on particle fragmentation behavior, identifying crucial parameters and delineating their influence on particle breakage.

The crux of the research lies in employing the discrete element method (DEM) to simulate particle breakage within a granulator. Leveraging Tavares' breakage model, the study elucidates the pertinent equations and their objectives. The granulator's geometry is replicated in SolidWorks and imported into EDEM for simulation purposes.

Central to the inquiry is the overarching research question: *"How to improve the granulating performance at GreenCycl B.V.?"* This question prompts an examination of both geometric and operational parameters affecting granulator performance. Four geometries (Long Axis - 2 Cutting Blades, Long Axis - 3 Cutting Blades, Short Axis - 2 Cutting Blades, Short Axis - 3 Cutting Blades) are scrutinized, with five simulation repetitions per geometry, assessing their impact on particle generation, mass flow rate, and particle size distribution of the output. The Short Axis - 3 Cutting Blades configuration emerges as the most productive, thus warranting further investigation.

Further analysis involves exploring the influence of rotation speed (high versus low) and filling technique (simultaneous versus sequential) on particle generation, mass flow rate, and particle size distribution, with three repetitions per category. The findings indicate that a high rotation speed combined with a simultaneous filling technique yield optimal results. Despite the higher power consumption associated with high rotation speeds, the increased mass flow rate and reduced dust formation render the energy expenditure per unit mass produced relatively lower.

This study not only enhances understanding of granulator performance dynamics but also provides valuable insights for optimizing operational parameters to maximize productivity and efficiency within granulation processes at GreenCycl B.V.

# Contents

# 1 Introduction

## 1.1 Background

In a world where raw materials are becoming increasingly scarce and climate impacts are more important than ever, it is imperative that steps are taken to solve the problem of growing waste streams. These waste streams can be divided into four different categories: post-consumer waste, industrial waste, agricultural waste and hazardous waste. Different methods have been defined to process all these different waste streams. Based on the risk a particular waste stream poses to society, the waste can be considered safe for recycling. The percentage of waste that is recycled is increasing worldwide. In the Netherlands, it is now standard practice that (plastic) beverage packaging and cans are collected separately from residual waste. This waste stream ends up at an installation where it is sorted, molten and fabricated into new granulate. This granulate can be used to make new plastic products (for example by means of injection molding).

However, many steps still have to be taken in order to reach the end goal of recycling all waste and reach a fully circular economy. A major problem is the hazardous waste. Because this waste may pose a danger to society, it must be handled with great care. It is important that the waste comes into contact with people as little as possible and that the hazardous substances are not released. For this reason, the waste is transported to the waste processing company in sealed containers. Here the hazardous waste is in most cases incinerated. What remains is bottom ash and non-molten metal. The metal can be separated from the ash and can be used for new applications. The leftover bottom ash is worth much less than the raw product and can only be used for the production of asphalt and concrete. This process leads to excessive greenhouse gas emissions and further depletion of raw materials. It is therefore necessary that steps are taken to prevent the incineration of waste.

Hospitals are one of the largest producers of hazardous waste. For example, hospitals in the Netherlands release an average of 27 kilograms of waste during one operation. Therefore Dutch hospitals are responsible for 8% of the total CO2-emissions within the country. A major cause of this waste stream is the use of medical disposables. These are instruments that can only be used once for safety reasons and due to the interests of OEMs (Original Equipment Manufacturers). Most of this waste is sent to Zavin. This is the only company in the Netherlands that has permission to incinerate medical waste. However, only a small part of this waste stream consists of contaminated waste (containing blood residues, etc.). The remaining waste is also considered as contaminated for safety reasons and because of procedures within hospitals. However, contamination is not always present within the material. It is therefore important to distinguish between contaminated versus uncontaminated waste (based on hazard risk for society) and sterile versus non-sterile. For example, a large part of the medical waste is no longer sterile, but can be recycled without risk and therefore saved from the incinerator.

There has lately been a lot of interest in the concept of 'urban mining'. Urban mining is the reclaiming of raw materials from waste products sent to landfill. This, in contrast to geological mining, where raw materials are used to manufacture new products, is a sustainable way to secure an independent source of raw materials. Due to the quantity and high quality of uncontaminated hospital waste, medical waste offers a good source for urban mining.

A major waste stream within hospitals is the use of medical wrapping paper. Although the name suggests otherwise, these are cloths made of polypropylene to wrap medical instruments. These instruments are packed in the central sterilization department of hospitals. The cloths serve as a guarantee of sterility. Once the instruments are wrapped, they are steam sterilized in an autoclave and sent to the operation room. Here the wrapping paper is removed from the instruments. The paper is then immediately thrown away without coming into contact with hazardous substances. Since the wrapping paper is considered as medical waste, there could be a risk of danger and therefore the used wrapping paper is sent for incineration at Zavin.

To combat the one-time-use of medical disposables, various initiatives to recycle medical waste streams have evolved. One example of a novel company that is focusing on the recycling of medical waste is GreenCycl. GreenCycl develops circular, economically interesting solutions for healthcare. GreenCycl is the first company that has been able to recycle the specific waste stream of medical wrapping papers. The current process is as follows: cloths are stripped of tape residues, melted down, granulated and then used to make new medical products by means of injection molding to close the circle and create circularity.

GreenCycl wishes to expand its activities, so that not only polypropylene cloths can be recycled, but also other packaging material. A pilot is now being worked on in collaboration with Stryker Corporation. Stryker is an American multinational medical technology company. In order to become more sustainable, Stryker is looking for ways to recycle their products. A project that is currently being run is the recycling of PET-packaging material. The advantage of recycling solid PET instead of molt-blown polypropylene is that the material does not need to be melted down, but can be granulated directly. This saves a considerable amount of energy and promotes efficiency.

However, the granulation process is far from optimal. While blockage often occurs during the granulation of polypropylene blocks, the granulation process of PET-packaging also has its shortcomings. For example, the granulator is not able to granulate large packages without pre-shredding and the granulation process takes a fair amount of time. This Master thesis will delve into the development of comminution equipment, specifically aimed at granulators processing solidified polypropylene blocks. Research will be conducted to find the important design parameters and their influence on the efficiency of the granulation process and the quality of the resulting granulate. DEM simulations will be used to look at how the geometry and operating parameters of a granulator can be optimized to obtain the best quality granulate in the shortest possible time. A novel particle breakage model will be used for the DEM-simulations.

## 1.2 Problem Definition

Recycling is an activity that is becoming increasingly important to guarantee sustainability. Recycling conserves energy, reduces pollution and greenhouse gases and conserves natural resources. A disadvantage of recycling is the fact that it is a costly activity and generally requires a considerable amount of energy. The quality of the end product may also have different properties compared to virgin material. It is therefore important that research is conducted into how to invest as little energy as possible while still aiming for the best possible end product. Apart from the current processing of polypropylene, the current recycling process of PET-packaging material within GreenCycl and partners consists of two important steps: the reduction of the packaging material (referred to as comminution in this paper) and the melting of the resulting flakes into thermoplastic feed-stock to create new products.

Figure 1: Granulator steady-state

A major complication lies in the first processing step, the comminution. At the moment a Moditec Goliath Plus granulator is used in which the PET-packages are fed in their entirety. The granulator consists of a rotating wheel containing two large staggered blades that are used for the initial cutting. Furthermore, the rotating wheel consists of teeth cutters which are used to reduce the material into smaller sizes. However, due to the size and geometry of the PET-packages, the granulator tempts to make only one cut inside the package. After this initial cut, the material is stuck into place and the rotating staggered blade keeps following the same path through the cut already made. For this reason and due to the geometry of the material, the process will enter a steady state. Adding new material will not counteract this steady state, because the weight of the PET-packaging is too low to exert enough down-force on the cutting blades and the geometry is such that the filling opening of the granulator gets clogged. The latter can be prevented by a different type of supply geometry, which is not considered in this paper.

To achieve a granulate with a desired size and quality, it is important that a granulator is used with the highest possible efficiency. It is therefore insightful to study the effects of different geometries (e.g. cutting chamber, rotor and screen design) and operation parameters (e.g. rotation speed) on the granulator performance. The use of the Discrete Element Method (DEM) provides enhanced understanding of the processes and often reduces the number of physical experimentation required. By means of a parametric analysis and the use of novel particle breakage models integrated as API in EDEM, it is possible to simulate how a granulator can be used as efficiently as possible for a specific material type and geometry. This offers opportunities to scale up the production process and ultimately reach a fully circular economy.

## 1.3 Thesis Objective

For this thesis, the following research questions can be defined:

Main-research question:

- How to improve the granulating performance of polypropylene blocks at GreenCycl's recycling plant by analyzing comminution interactions using the Discrete Element Method (DEM)?

Sub-questions:

- What factors influence particle breakage?
- What are the critical parameters in the design of comminution equipment?
- How can particle breakage models contribute to simulating comminution interactions?
- How can particle breakage be implemented in granulator interactions?

These research questions will be answered in the course of the report. At the end of the report, the answers to the research questions are summarised in the conclusion.

## 1.4 Thesis Outline

- Chapter 1 (introduction) sets the stage by providing an overview of the recycling industry and the specific context of GreenCycl's recycling plant. It outlines the primary research objectives, emphasizing the importance of optimizing granulator interactions. Additionally, it offers a preview of the thesis structure, guiding readers through the subsequent chapters.

- Chapter 2 focuses on analyzing particle breakage mechanisms. The chapter examines loading and breakage mechanisms in granulation processes, considering the influence of material properties and environmental factors.

- Chapter 3 delves into the study of designing comminution equipment. It begins by providing an overview of various types of comminution equipment and their applications in mining processes. Subsequently, it explores the critical design parameters that significantly influence the performance. Through detailed analysis and empirical studies, the chapter examines how variations in these parameters impact granulator efficiency, particle size distributions and energy consumption.

- Chapter 4 introduces the Tavares breakage model, a key aspect of granulator performance analysis. It provides an in-depth explanation of the model's principles and equations, detailing how it simulates particle breakage behavior.

- Chapter 5 details the implementation of Tavares' breakage model within the EDEM simulation framework to study granulator breakage interactions. The chapter provides a step-by-step guide on how the model is integrated into the EDEM software, including setting up the simulation environment and defining parameters.

- Chapter 6 (results) investigates the optimization of granulator performance by analyzing the impact of operational and geometrical parameters. It assesses how factors like rotation speed, filling technique, axis length, and amount of cutting blades affect granulator output. Insights derived from simulation studies and experimental data are presented to inform optimization strategies.

- Chapter 7 (conclusion) summarizes the key findings of the research and discusses their significance. It explores the implications of the findings for granulation optimization and recycling operations, offering directions for future process optimizations at GreenCycl B.V.

- Chapter 8 proposes recommendations for future research are outlined in this chapter. It suggests exploring additional operational parameters to enhance granulator performance and improving particle breakage modeling and calibration techniques for more accurate simulations. Additionally, it advocates for addressing uncertainties and promoting sustainability practices in granulator operations.

- The appendices include any supplementary materials, such as a research paper (Appendix A), detailed technical drawings of the geometries created in SolidWorks (Appendix C) and additional information about the sensors being used (Appendix D), to support the findings presented in the thesis.

- Lastly, the references section provides a comprehensive list of all references cited throughout the thesis, allowing readers to access the sources for further exploration and verification.

Figure 2 represents a flowchart indicating the outline of this thesis in a graphical way:

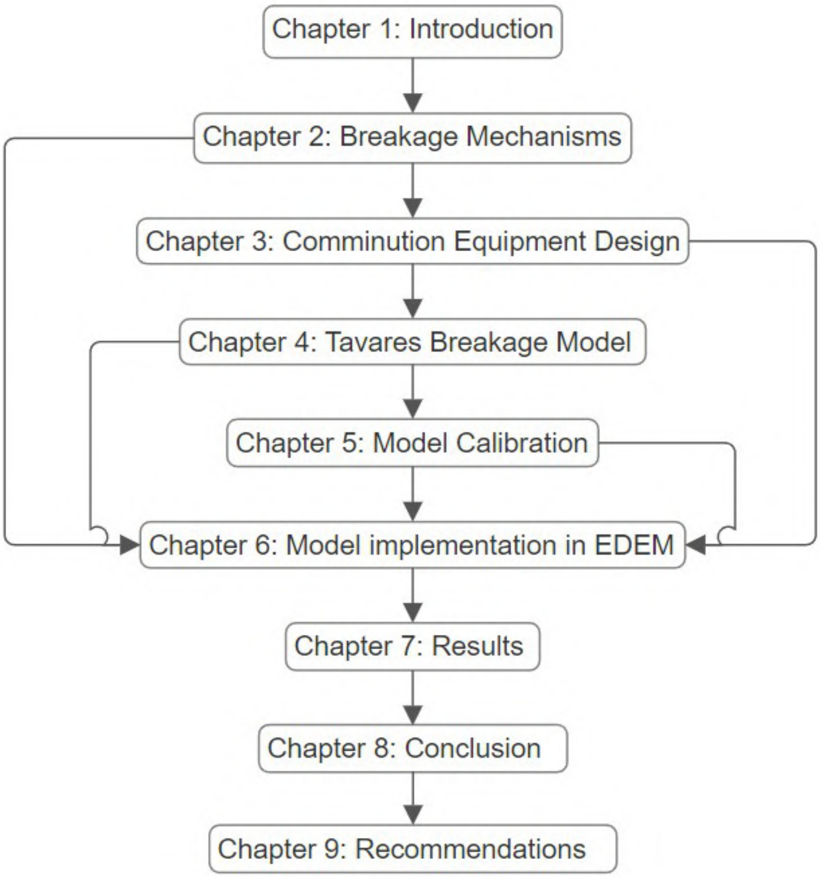

Figure 2: Thesis outline flowchart

# 2 Factors influencing particle breakage

## 2.1 The design of comminution equipment

Reducing the particle size of solid materials is an operation that has various application fields within the industry. Another word for the reduction in particle size of solid materials is: 'comminution'. This word originates from the mineral ore processing industry, but has found application in various fields of solid material size reduction. In the heavy mineral ore processing industry, particle breakage equipment is indispensable in mines where it is used to separate precious metals from waste rocks. Another area where comminution is often seen is within the field of recycling. By means of comminution, large products, such as plastic packages, can be reduced in size, which allows for more kilograms of material to be stored per available unit of volume. This makes it possible to efficiently use the often limited space available at waste processing facilities. Also, by means of reduction in particle size, different types of materials can be separated mechanically. This ensures a more homogeneous input into the sorting installation, which in turn benefits processing efficiency.

Materials consist of molecules, atoms or ions. The arrangement can be a regular pattern (i.e. crystalline) in an imaginary lattice, also known as the crystal lattice. Within a crystalline substance there can be regularity occurring over a long distance or over a short distance. The arrangement can also be completely random (i.e. amorphous).

Inside a crystalline solid (i.e. crystal), the constituents (such as atoms, molecules, or ions) are arranged in a highly ordered microscopic structure (crystal lattice) which extends in all directions. The lasting attractions between atoms or ions that enable the formation of molecules and crystals are called chemical bonds. The bonds may result from the electrostatic force between oppositely charged ions as in ionic bonds, or through the sharing of electrons as in covalent bonds. The crystal structure is not always fully repeating and may therefore contain errors. At these points an abrupt change in the arrangement of atoms takes place, which causes the material to be the weakest at these dislocations.

When a load is applied on a material, potential energy of the load will first be converted into elastic energy inside the crystal lattice of the body. The elastic energy that can be stored is finite and will eventually reach a critical value. When this value is exceeded, the attractive forces between the crystal planes will not be sufficient and a micro-crack will be formed within the inter atomic bonds. This crack can grow and lead to material failure. Regularly, inherent flaws are already present within the lattice structure that often lead to failure of the material in the direction of the flaw. This is also the case for crystals with no identifiable characteristic shape, such as amorphous materials.

Based on the propagation of cracks within a material, also known as fracture mechanics, a distinction can be made between two types of materials: brittle and ductile. When a brittle material is subject to stress, crack propagation will occur without serious plastic deformation. Brittle materials have a high strength, show a fast crack propagation and have a smooth fracture surface. Examples of brittle materials are ceramics and different types of glass. In contrast, a ductile material will first deform plastically before breaking. Ductile materials have a lower strength, will first yield before cracking and have a rough fracture surface. Examples of ductile materials are most metals.

The reduction of particle size is an energy intensive activity. Comminution operations are the largest energy consumer in many mine sites and therefore a large component of cost. In mines alone, comminution uses nearly 2% of all electrical energy generated on the planet. [4] It is therefore essential that research is conduction into optimizing comminution performance from both a material perspective and an energy consumption perspective.

## 2.2 Loading Mechanism

Over the years, various different types of comminution machines have been developed and improved. To make the right choice as to which comminution machine is most suitable for a specific application, the type of feed material, the available resources, the requirements of the end product and the efficiency of the machine must be taken into account. Depending on these requirements, the most desirable method of particle breakage needs to be determined. [5]

In order to choose the most suitable machine, a distinction can be made based on the specific loading mechanisms that introduce mechanical stress which can cause particle breakage to take place. A main distinction can be made between compression, shear, impact and strike:

- Compression: a continuous compressive force is exerted perpendicularly to the surface of a material by two rigid bodies where one or both are pushing towards each other. Since stress is applied in a slow rate, crack propagation inside the material also tempts to be slower.
- Shear: a shear force is exerted on a material in an opposite and adjacent parallel line of action. Shear can be initiated by particles moving along eachoter or along the geometry of the equipment. Another loading mechanism that is closely related to shear is: 'attrition'. Attrition is a fast acting mechanism which leads to surface-level destruction. Since attrition can be considered a fast shear loading mechanism, it is placed under the shear loading category.
- Impact: a rapid application of stresses is exerted on a particle after falling and hitting a surface. Impact stresses are caused by high momentum. Since stresses are applied rapidly, enough energy is provided at once for the particle to fail.
- Strike: as with impact, a rapid application of stresses is exerted on a particle. The main difference between impact and strike is the part of the system doing work. During impact the particle itself will have high kinetic energy which will be converted to the system, while during strike the system will convert high kinetic energy to the particle.

The aforementioned loading mechanisms in comminution machines can be divided in four loading categories based on the loading direction: compression, shear, impact and strike (figure 3). It is important to notice that tension is not mentioned as a loading mechanism. The reason is that comminution equipment does not put material directly under tension. However, most of the particle breakage is caused by tensile forces that are acting outwards at right angles to the applied compression. In case of comminution at mines, this phenomenon can be explained by the fact that the tensile strength of rocks is much less than the compressive strength. [6]

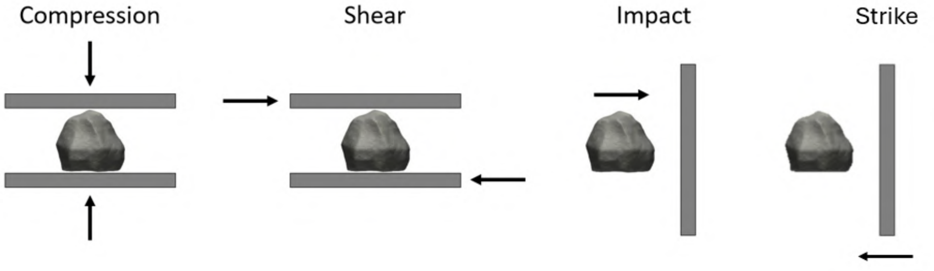

Figure 3: Loading mechanisms

## 2.3 Breakage Mechanisms

The strength that is needed to let breakage occur, depends on several factors. Based on the structure and intrinsic properties of the material, a crack will form or propagate. When sufficient energy is applied to a brittle material, the critical crack length will be reached and the initiated crack will continue to grow throughout the length of the material. The total change in energy of the system can be defined as increase in surface (free) energy minus the decrease in elastic energy. Surface energy is the energy created by the disruption of intermolecular bonds that occurs when a surface is created. Elastic energy is the energy stored when the material is elastically deformed. This energy can be recovered when the material returns to its original position. The change in the system's energy by crack propagation can therefore be defined by the following equation:

$$\Delta U = 4 \cdot \gamma_S \cdot C_{CL} - \pi \cdot C_{CL}^2 * \frac{\sigma_S^2}{E} \tag{1}$$

Where $\gamma_S$ is the free surface energy per unit area, $c_{CL}$ is the crack length, $\sigma_S$ is the stress intensity and E is the Young's Modulus.

The breakage mechanism is strongly influenced by the loading mechanism. For example, certain forms of breakage occur faster with one loading mechanism than with the other. A distinction can be made between four different types of breakage mechanisms: shattering, cleavage, chipping and abrasion. Particle breakage can generally be divided into two categories:

- Shattering: is often seen during high impact events and can be characterized by extreme fragmentation which leads to a wide range in progeny size distribution. An example is a situation in which a particle hits a surface with a considerably high impact. Shattering is therefore often seen during impact loading.
- Cleavage: takes place when the intensity of the applied energy is lower compared to shattering. The result is a progeny distribution consisting of large inner-body particles and finer particles in areas of high stress. An example is a press in which a material is clamped. At the points where the force is applied, the material will crush into small progenies, while larger progenies will be formed in the middle of the parent material. Cleavage is most commonly seen during compression loading.

Both shattering and cleavage breakage mechanisms can also occur together, which in the literature is referred to as massive fracture.

Furthermore, a distinction can be made between two different fracture modes: breakage at the surface of the particle and breakage within the body of the particle. Surface breakage occurs when the force applied to the material is not high enough to break the internal structure. This leads to small progenies being formed on the surface of the material, while the inner structure of the material stays intact. As a result, the shape and dimensions of the parent material will not differ greatly. Surface breakage can occur in two different ways:

- Chipping: when an angular load is applied on an irregularly shaped particle, several fractures form below the surface of the material, which can grow towards the surface. This will lead to the chipping off of rough corners and edges of the material. Chipping is considered a fast breakage mechanism. Chipping is most often caused by shear loads.
- Abrasion: due to the mutual movement of particles rolling and sliding over each other and against the geometry of the communication equipment, low shear stresses will be generated at the surfaces of the particles. This leads to a limited form of surface wear and can cause small progenies to release from the parent material. Abrasion is considered a slow breakage mechanism. As with chipping, abrasion is caused by shear loads.

## 2.4 Effect of breakage mechanisms on progeny sizes and shapes

The main goal of comminution operations is to reduce the initial size of particles to a desired range, so that a more or less uniform material size distribution is created, allowing further processing of the materials. By studying the size distribution of particles been subject to comminution operations, it is possible to see what effect a certain breakage mechanism has on a particle. To be able to conduct this study, it is important to take the initial particle size distribution into account. After all, a relatively large initial particle size distribution causes a different progeny size distribution compared to a relatively small progeny size distribution. Therefore, comminution data first needs to be normalised in order to make mutual comparisons. One of the first works that studied the effect of breakage mechanisms on the particle size distribution has been [7]. A considerable amount of follow-up research is based on these findings.

Research has also been done into the effect of a loading mechanism on the particle size distribution [8]. A shortcoming is the fact that the geometry of the initial particles and its influence on the progeny size and shape distribution have not been taken into account.

The breakage mechanism affects the shape and size distribution of the progenies. A distinction can be made between different breakage mechanisms and their resulting progeny shape and size distributions:

- Shattering: the high impact creates a wide size distribution of progeny particles which are characterized by their the sharp edges. These particles take on a more or less cubical shape.
- Cleavage: due to the lower intensity of the applied energy, the inner-body of the mother material will experience breakage but less fragmentation compared to shattering. However, small progenies will form in places where high stress is applied. This can be seen in figure 4a .
- Chipping: because of the formation of fractures in the inner-body of the mother material, large sharp corners in the material can be broken off. This creates a wide range of progeny sizes and shapes, while the original material takes on a more uniform shape.
- Abrasion: the result of abrasion is comparable to that of chipping. Since the stress exerted on the material is lower, the process will take a considerably larger amount of time and the progenies that break off the surface will be smaller compared to chipping. Due to the relatively low applied energy, the particle will only be damaged on the surface, while the inner-body remains intact. This results in the mother particle taking on a spherical shape, while dusty progenies are being formed at the surface. Figure 4b shows the result of abrasion.

(a) Cleavage

(b) Abrasion

Figure 4: Examples of breakage mechanisms

The blocks shown in figure 4 consist of molten down polypropylene used as a base material for the fabrication of medical wrapping paper. Due to the brittle character, the blocks will practically only deform plastically before fracture occurs, and thus not flow. A Moditec Goliath Plus 2 low-speed granulator, consisting of two cutting blades, has been used for this experiment. Since the momentum of the granulator is low due to low speed, but the energy is high, only one large fracture occurs in the inner-body of the block during the first impact of the granulator cutting blades. However, it can be noticed that smaller progenies have broken off at the place on the surface subject to the impact (figure 4a). As the grinding process continues, the blocks will come into contact with each other, with the rotating granulator wheel and with the shaft of the granulator. When the blocks do not get caught between the shaft and the rotating cutting blades, no high impact will take place. As a result, smaller fractures will occur on the surface, so that the inner-body of the parent material remains intact, while on the surface small progenies are slowly formed which lead to the material taking on a spherical shape (figure 4b).

Not only does the way in which the stress is applied influence the breakage mechanism, the effect on the breakage mechanism of material properties together with the way in which particles are mutually structured has also been point of discussion.

For instance, a stress can be exerted on a particle bed consisting of a single layer (also known as monolayer) of particles, but the stress can also be exerted on a particle bed consisting of multiple layers of particles. In this case, the breakage mechanism on the layer directly in contact with the stress will be different from the breakage mechanism of subsequent layers. For example, particles experiencing direct contact with the comminution geometry are more likely to have cubical shapes compared to the particles inside the bed. [9]

It has been argued that the internal material properties have more influence on the breakage mechanism, compared to the type of comminution equipment used for breakage. In order to create a more cubical progeny shape, breakage by means of impact instead of attrition is more likely to provide the desired results. Furthermore, cubical progenies can be achieved by means of direct breakage between particle and comminution equipment instead of cushioned mutual breakage between particles. [10]

Over the years, some form of agreement has been reached about the characteristic shapes that can be created by different ways of comminution. For example, there is a general agreement that by means of shear stresses (for example in ball mills), mainly spherical, uni-dimensionally shaped objects are produced, as can also be seen in figure 4b. Where the shape is the result from different particle-to-particle collision. On the other hand, breakage by means of compression leads to more angular shaped progenies as can be seen in figure 4a. However, a basic concept for these findings has never been established. This encourages the discussion about the influence of the nature of the material versus the type of comminution equipment on the progeny size distribution. [10]

## 2.5 Other factors influencing breakage mechanisms

A distinction can be made between different factors that influence the breakage mechanism of particles. These factors not only depend on the past of the particle (e.g. pre-treatment), but can also be both internal and external and can relate to the particle as well as to the specific comminution equipment. The most important parameters that influence the breakage mechanism of a particle are: particle size, particle shape and internal texture. For comminution equipment the most important factors are: loading mechanism, intensity of load, particle temperature during operation and usage of a liquid (i.e. wet or dry granulation). First the effect of the particle properties on the breakage mechanism will be described.

### 2.5.1 Particle size

The size of the material greatly affects its breakage mechanism. This is partly caused by the internal stresses present in the material. As explained earlier, a material consists of a structure of individual crystalline areas, also known as grains. When defects are present in this crystal structure, there is a risk of fractures to occur. Assuming that the amount of defects per number of volume is more or less the same, it can be stated that the probability to find defects is greater as the size of the material increases. Apart from the probability to find any defects, the size of any fractures following from defect breakage decreases as the material is smaller. Therefore, the average stress level in small particles is greater compared to large particles. However, it is important to remember that the overall amount of energy required to break a particle is higher for larger particles compared to smaller particles. For this reason, it can be said that when the same amount of energy is transferred to both large and small particles, the particular breakage mechanism per particle will depend on its size. Accordingly, large particles are more likely to show abrasion and chipping breakage mechanisms, while smaller particles are more likely to show shattering breakage mechanisms. As a result, if subject to the same amount of energy, large particles will more often retain a round structure, while small particles will sooner adopt an angular shape. However, there is a limit for breakage. When this critical (fracture) diameter is reached, the material will adopt a ductile rather than brittle breakage mechanism. This means that crystal planes shift rather than break, causing plastic deformation.

### 2.5.2 Particle shape

The shape of particles also has a considerable influence on the way breakage is occurring. This discrepancy is caused by the size of the surface where energy is transferred from the comminution equipment to the particle. When a particle consists of protruding sharp corners and edges, during compression or impact, the energy is most likely to accumulate here. This energy can initiate a surface fracture that will be propagated throughout the particle, leading to shattering or cleavage breakage mechanisms. Meanwhile, the energy is less likely to accumulate inside particles with a more spherical shape. Thus, the breakage mechanism will be abrasion or chipping.

### 2.5.3 Ore texture

An important property of materials is the ability to absorb energy before fracture. This term is indicated by the word: 'toughness'. It is important to distinguish between the word: 'strength' and the word: 'toughness'. While the strength indicates the ability of a material to withstand an applied load without plastically deforming, the toughness describes the total amount of energy that can be absorbed before breakage. It is important to remember that a material with a high strength does not indicate that the material also has a high toughness. For example, a brittle material such as high carbon steel will have a higher strength compared to medium carbon steel, but medium carbon steel will have a greater toughness. An insightful way to understand this phenomenon is by looking at the area under the stress-strain curve. When on the x-axis the ductility, the amount of plastic deformation before fracture, is plotted against the strength on the y-axis. It can be seen that even though the strength is lower, and so the plastic deformation occurs earlier, the material with the higher toughness will yield longer, so that the area under the curve is larger. As a result, the higher the toughness, the better a material is able to absorb energy slowly.

Because the strength and toughness of materials differ, their breakage mechanisms will also be different. The toughness is largely determined by the crystal structure of the material. As already mentioned, crystalline materials, such as rocks are composed primarily of grains of minerals, which are crystalline solids consisting of periodically arranged atoms which are chemically bonded into an orderly structure. Apart from differences in crystal patterns, some materials are more susceptible to breakage caused by weak crystal planes and the presence of micro-cracks, which are formed when the stresses exceed the local strength of grains. As a result, not only will the breakage mechanism be different, but the end products will also have a different shape.

Apart from the type of material, other factors also influence the breakage mechanism of a material. These factors can be material specific. First of all, the presence of micro-cracks. As a rule, the more micro-cracks present in the material, the greater the chance that the material will fail. This is because micro-cracks can be described as small damages inside the material. These micro-cracks can grow and lead to breakage. The occurrence of micro-cracks depends on the adhesion and toughness properties of the material.

The grain size also influences the breakage mechanism of materials. The following applies: the smaller the grain size, the stronger the material. This can be explained by the amount of space in which dislocations are able to move. The smaller the grain size, the smaller the distance over which dislocations can travel. As a result, atoms are less likely to slide over each other at low stress levels, so that the possibility of cracking is reduced.

Finally, the degree of porosity also influences the breakage mechanism of the material. The porosity is the volumetric fraction of pores in the material. The porosity of a material is expressed as the ratio of the volume of pores to the volume of bulk. Since a porous material contains a considerable amount of pores, the residual stress will be distributed over the remaining area of bulk material. This remaining area is limited and will cause stress accumulation. As a result, when comparing two materials with the same outer dimensions, the stress will be more concentrated in a porous material compared to a non-porous material. Therefore, due to the higher stress concentrations, a material with a high porosity will break faster than a material with a low porosity.

### 2.5.4 Loading mechanism intensity

The breakage mechanism does not only depend on the type of loading mechanism, but also on the intensity of the applied energy. For example, a particle can have different breakage mechanisms, while undergoing the same loading mechanism. When the applied energy is relatively low, surface fracture will mainly occur, leaving the inner-body of the material intact. If the applied energy is larger, the inner-body of the material is more likely to crack. For instance, the process can be used in which a particle with certain velocity comes into impact against a rigid body. When the magnitude of the particle velocity is relatively low, the impact energy will also be on the low side and fracture is likely to only occur at the surface of the particle. The breakage mechanism will therefore be abrasion or chipping. When the object is thrown against a geometry at a relatively high speed, the released energy will be larger and the inner-body is more likely to also be damaged. As a result, shattering will occur as a breakage mechanism. The same theory can be used to explain the fact that shattering will occur less frequently with particles consisting of a greater mass or density than with particles with a lower mass or density. This is because larger, more dense particles require a higher force to achieve the same impact speed compared to small, less dense particles. When the same amount of energy is used, larger, more dense particles will therefore have a lower impact velocity and shattering will occur less quickly compared to small, less dense particles.

### 2.5.5 Temperature

Comminution operations cause materials to heat up since kinetic energy is transformed into heat energy. Temperature can change the breakage mechanism of materials. This originates from the fact that increasing temperature lowers the critically resolved shear stress for plastic deformation or slip on planes. Therefore, a higher temperature ensures easier movement of dislocations. This is also the reason that materials will deform plastically at higher temperatures and thus become ductile. At lower temperatures, materials become brittle and are more likely to break instead of deforming plastically. Ductile materials use the input energy to deform plastically, while brittle materials use the energy to create new surfaces in the form of cleavage planes. This reasoning mainly concerns crystalline structures. Any amorphous (non-crystalline) solid in which the atoms and molecules are not organized in a definite lattice pattern can act different. Because the temperatures during conventional comminution operations do not reach high enough temperatures, these phenomena are less likely to occur. [11]

### 2.5.6 Wet or dry

To optimize the comminution operation, a processing fluid (e.g. grinding fluid) may sometimes be used. For example, water can be added during the comminution process to prevent high energy consumption and to decrease the wear of the equipment. Dry processing uses a single pass principle in which material enters, passes through and is expelled with a varying reduction in size. Wet grinding uses the process of re-circulation in which the liquid-particle slurry is exposed multiple times to the comminution equipment. Since the created viscous slurry works as a suspension, destructive breakage is less likely to occur compared to dry processing. Research has shown that the energy consumption needed to reach the desired particle size distribution is 15-50% larger for dry processing compared to wet processing. For this reason, a wet process is generally preferred. Apart from the influence on the particle breakage mechanisms, the scarcity of water at some comminution facilities (e.g. mines) also influences the possibility of wet processing. However, adding a processing fluid also affects the breakage mechanism of the particles. With the same energy consumption, dry processing will on average produce larger particles compared to wet processing. Also, the size distribution of the progenies will be larger in a dry process compared to a wet process. Furthermore, dry grinding will produce rougher surfaces compared to wet processing. Wet operations, on the other hand, produce a more even surface. Therefore, it can be said that cleavage and shattering are the dominant breakage mechanisms in dry processing and chipping and abrasion are the dominant breakage mechanisms in wet granulation. [12]

### 2.5.7 Pre-treatment

Pre-treatments are used to decrease the strength of materials. Common energy carriers used for pre-treatment are specific wavelengths (e.g. microwaves & ultrasonic waves), electricity and temperature. By means of pre-treatments, micro-cracks can be formed in the inner-body of particles. Micro-cracks act as a mechanism where stress-concentration takes place and can therefore facilitate the particle breakage and influence the final breakage mechanism. Due to the presence of micro-cracks, a material can fail sooner than if no pre-treatment has taken place. Because pre-treatment can create micro-cracks in the inner-body, it is more likely to fail and breakage mechanisms can be shattering and cleavage instead of chipping and abrasion.

### 2.5.8 Breakage effects

Within the mineral processing, where comminution equipment is mainly used, a distinction can be made between random breakage and non-random breakage. A multi-phase particle consists of minerals in different phases. The phase of a mineral refers to the specific molecular or crystal structure. This structure depends on various conditions (e.g. temperature, pressure, etc.). When breakage occurs independent of the mineralogical texture, the fracture process is considered to be random. When breakage occurs depending on the mineralogical texture, the process is called non-random. Within the class of non-random fractures, six different fracture effects can be distinguished when the particle is composed of several phases: [7]

- Selective breakage: a particle consisting of different phases of brittleness is most likely to break fastest at the mineral phase with the highest brittleness. This is caused by the fact that the more brittle the material, the more easily fracture will occur.
- Differential breakage: depending on the constitution of the parent material, the progeny size distribution will be different for a single breakage event. This composition depends on several factors and is not based only on the difference in brittleness.
- Preferential breakage: when fast fracture in brittle materials occurs earlier in specific mineral phases compared to others.
- Phase-boundary fracture: as the name suggests, this phenomenon occurs when cracks initiate across the boundary between different material phases. Compared to the previous breakage fracture effects, fracture occurs on the boundary instead of across a phase.
- Liberation by detachment: occurs when individual mineral grains are relatively loosely bounded within the finer-grained mass of material, initiating cracks.
- Boundary-region fracture: when cracks propagate in the highly-stressed region around the phase-boundary instead of directly on the phase-boundary.

#### Concluding remarks

This chapter described how different loading parameters, material parameters and environmental parameters can contribute to the breaking behavior of particles. These effects are based on findings in the ore processing industry, where comminution operations take place most often. This also implies that the phenomena described above take place during the processing of brittle crystalline materials. The fracture behavior can therefore be different for ductile and amorphous materials.

There is a general believe among scientists that the breaking behavior only depends on the ore texture of the material in question. However, in the studies described above, the way in which a load is applied (loading mechanism) together with the occurrence of pre-treatments could also have an effect on the breaking behavior of materials. However, there is yet no scientific explanation for this assumption.

# 3 Important parameters in the design of comminution equipment

Different types of machines can be used for comminution operations. Depending on the desired input size and final size of the particles, a choice can be made which machine can realize the process as optimally as possible with the right capacity and energy used. A distinction can be made between different types of comminution equipment based on different loading mechanisms. In the next paragraph, an overview of common comminution equipment will be presented together with the specific working principle and important parameters.

Generally speaking for the mining industry, the first crushing stage takes places by using jaw crushers (5a), gyratory crushers (5b) or cone crushers (5c). The gyratory crusher and cone crusher are very similar in design. The jaw crusher however has a different working principle compared to the latter. In general, the gyratory crusher is used as a primary crusher for the pulverization of the coarsest particles. After this first reduction step, other crushers such as a jaw crusher or a cone crusher can be used as secondary or tertiary crushers. Each crusher has its own advantages and disadvantages. For example, a gyratory crusher is well capable of crushing coarse material, but less capable of crushing viscous ore. A jaw crusher, on the other hand, is not able to handle large particle feeds like a gyratory crusher. Nevertheless, it is better capable to handle viscous ore. Therefore, gyratory crushers are often used in the large-scale mining industry, while jaw or cone crushers are more commonly used in the small-scale mining industry.

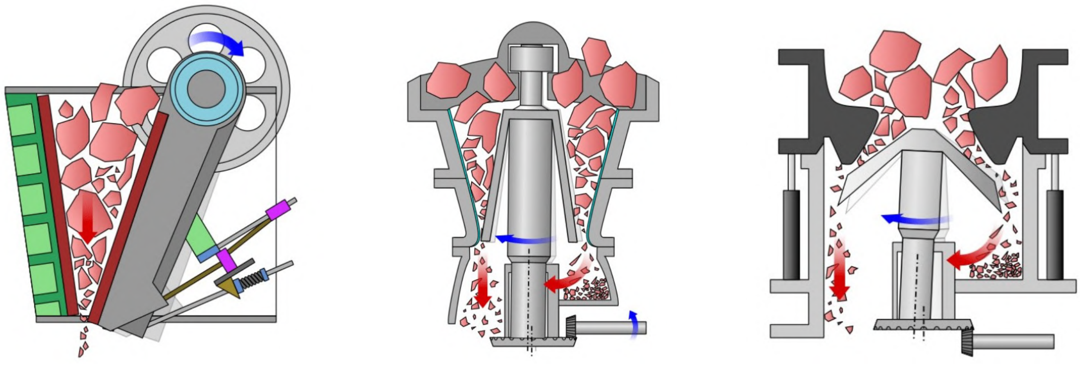
(a) Jaw crusher (b) Gyratory crusher (c) Cone crusher

Figure 5: Examples of comminution equipment [1]

The following paragraphs will discuss the differences in operating principle and important operating parameters of the most occurring comminution equipment. It is important to keep in mind that these are not the only equipment designs in which comminution can take place. Other devices include impact crushers, which use the concept of throwing particles against a solid stationary impact wall by means of a fast spinning rotor. Impact crushers make use of the impact loading mechanism. Other crushing equipment includes different types of mills such as autogenous mills and ball mills. The difference between the two is that an autogenous mill operates without the need of special grinding bodies. Instead, the coarser part of the ore simply grinds itself into smaller fractions. The loading mechanism here is abrasion. In a ball mill, on the other hand, size reduction is done by means of special grinding bodies. In this case metal balls with a general diameter of 10 millimeters are being used as grinding bodies. Impact takes place as the balls drop from near the top of the shell of the mill on the particles. The loading mechanism here is strike. Since the focus of this paper is on the first moment of contact during the granulator interactions, the following paragraphs will mainly focus on the compression loading mechanism. This principle takes place in jaw crushers, gyratory crushers and cone crushers, but not inside impact crushers and autogenous or ball mills. Therefore the working principle and important operating parameters of impact crushers and various grinding mills are considered to be outside the scope of this thesis.

## 3.1 Jaw crusher

Jaw crushers are a type of comminution equipment that use the compression loading mechanism. Jaw crushers consist of two metal plates (jaws) of which one moving plate and one fixed plate. The working principle of jaw crushers is based on the reciprocating movement of the dynamic jaw. This movement allows compression to take place between the two geometries and consists of an average of 100 to 300 cycles per minute. Material is supplied from the top and compressed between the two jaws due to the dynamic jaw moving towards the stationary jaw. When the dynamic jaw moves away, the material will fall down because of gravity. Subsequently, the material will be crushed again when the dynamic jaw moves back towards the stationary jaw. This process repeats until all the material has past the length of the geometry. The material is then discharged at the bottom of the jaw crusher.

There are two main types of jaw crushers: the Blake type jaw crusher and the Dodge type jaw crusher. The difference between the two is that in the Blake jaw crusher, the moving jaw is pivoted at the top, which causes the greatest movement to take place at the bottom. The Dodge type crusher on the other side has the moving jaw pivoted at the bottom, which causes the greatest movement to take place at the top. Since choking should be avoided at all the times, it is of major importance to allow jaw movement at the bottom of the jaw crusher. Therefore the Blake type crusher is preferred for most applications.

In the realm of crusher design and analysis, empirical relations have historically played a prominent role. These relations, derived from observational data and experimental results, offer practical insights into the complex interactions between various parameters governing crusher performance. Despite their potential limitations in dimensional consistency, empirical relations provide valuable insights into the effects of changing certain geometrical and operational parameters on crusher capacity, critical speed, and power consumption.

A review of the literature reveals that the majority of crusher relations are empirically derived, reflecting a historical trend in the field. While these empirical formulations have provided valuable tools for predicting crusher behavior under different operating conditions, there has been a noticeable lack of recent research aimed at refining or improving these relations. Despite this, the empirical relations have proven useful in understanding the impact of varying parameters on crusher performance.

To further elucidate these effects, this study includes plots showcasing the influence of changing geometrical and operational parameters on crusher capacity, critical speed, and power consumption. These plots provide a visual representation of the empirical relations, highlighting the trends and patterns observed in the data. By incorporating these visualizations, this study aims to enhance the understanding of crusher behavior and facilitate informed decision-making in crusher design and operation.

### 3.1.1 Jaw crusher dimension design

The maximum discharge diameter is determined by the size of the gap between the jaws at the bottom. Jaw crushers are driven by an eccentric shaft which produces the oscillating movement of the main shaft. The shaft is placed inside a heavy flywheel and is connected to a drive motor. Jaw crushers can be operated in both open and closed circuits. In closed circuits the oversized material will be fed back to the crusher, while in open circuits the material is not returned to the crusher. Jaw crushers operate best when being 'choke' feeded. This indicates that the feeding rate is regulated in order to keep the hopper full at all times so that the feeding rate will never be lower than the discharge rate.

There are a number of important dimensions that play a role in the design of jaw crushers. First of all the 'gape', this is the size of the feed opening. It is important that the particles that are being fed are small enough to fit through this opening. Therefore the design choice for the gape must be based on the size of the largest particle. A considerable amount of design parameters follows from this dimension [13]:

$$Gape\ size\ [m] = 1.1 * Largest\ particle\ size\ [m] \tag{2}$$

$$Vertical\ height\ of\ crusher\ [m] \approx 2 * Gape\ size\ [m] \tag{3}$$

$$1.3 * Gape\ size\ [m] < Width\ of\ jaw\ [m] < 3.0 * Gape\ size\ [m] \tag{4}$$

$$Throw\ [m] = 0.0502 * (Gape\ size\ [m])^{0.85} \tag{5}$$

Where the throw (or stroke) is defined as the difference between the open and closed positions measured at the throat of the crusher. Furthermore, the size of the opening on the discharge side is indicated with the word: 'set'. The ratio between the size of the gape and the size of the set is referred to as the reduction ratio. Typical reduction ratios for jaw crushers will be between 1:4 and 1:7. When describing the dimensions of a jaw crusher, usually only the size of the gape and the width of the jaw are being referred to. Figure 6 shows the relation between the gape size and the size of the crusher throw. It can be seen from the figure that the relation is approaching a linear course. However, the slope of the line is substantially low. In other words, for a considerable increase in the gape size, the crusher throw only increases slightly.

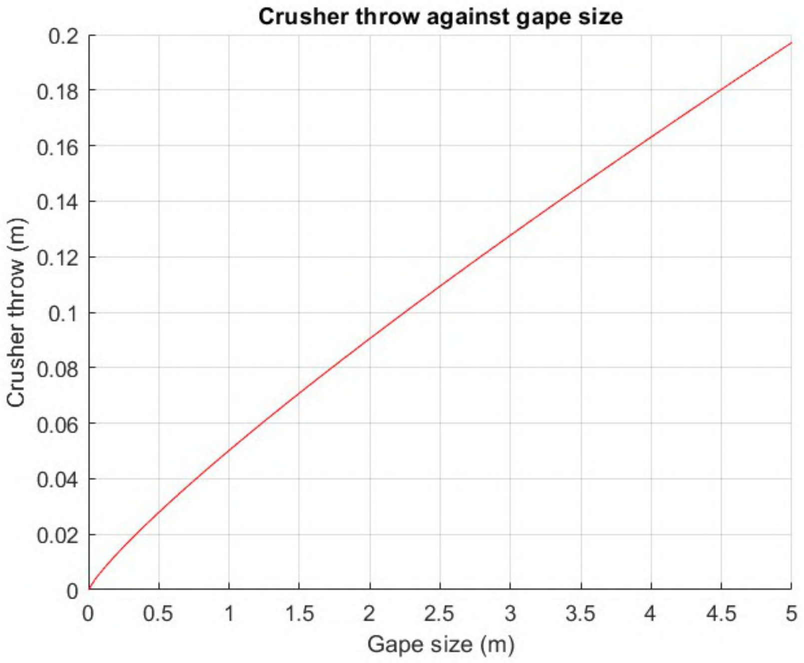

Figure 6: Crusher throw against gape size

### 3.1.2 Jaw crusher capacity

The capacity of a jaw Crusher indicates the amount of mass that flows through the set per unit of time and depends on several factors. The most important factors are: crusher geometry dimensions, the maximum amplitude of swing of the jaw (throw), the way in which material is fed in, operating parameters concerning stroke dynamics and the material being used. Over the years, a considerable amount of research has been conducted into determining the capacity of jaw crushers. For example, the authors: Hersam, Rose & English, Taggart, Broman and Michalson all attempted to approach the capacity as accurately as possible. Some models succeeded better in capturing truthful values compared to others.

**Hersam's model**
Hersam [14] formulated an emperical expression that provides an estimation for capacity. This expression is only reasonably acceptable for soft rocks and is therefore of limited use. The model will therefore not be further considered in this thesis.

**Rose and English's model**

Rose and English [15] calculated the capacity of a jaw crusher by examining the travel time and distance travelled between strokes. Rose and English based the distance travelled on the cycle frequency, on the dimensions of the set and on the angle of the pivot point. The smaller the difference between maximum and minimum opening of the set and the larger the angle of the jaw, the lower the capacity. The following equation can be defined for a jaw crusher with low stroke frequency:

$$Q_L = 60 * L_T * v * W_J * (2 * L_{MIN,S} + L_T) * \frac{R}{R-1} \tag{6}$$

$Q_L$ = crusher capacity at low frequencies $[m^3/hour]$
$L_T$ = crusher throw $[m]$
$v$ = crusher frequency $[cycles/minute]$
$W_J$ = width of jaw plates $[m]$
$L_{MIN,S}$ = minimum set distance $[m]$
$R$ = reduction ratio $[-]$

When the stroke rate passes a certain critical value, the capacity will decrease. For this reason, the previously mentioned equation will not hold for high frequencies. It can also be seen from line Y1 in figure 7 that an increase in reduction ratio leads to a decrease in capacity. This can be explained by the fact that, in order to reach a greater reduction, the machine requires more energy per amount of material. When the amount of supplied energy remains constant, the capacity will therefore decrease. A different equation is used to describe the crusher capacity at high frequencies:

$$Q_H = 132435 * W_J * (2 * L_{MIN,S} + L_T) * \frac{1}{v} \tag{7}$$

$Q_H$ = crusher capacity at high frequencies $[m^3/hour]$

The low frequency capacity curve is a linearly increasing curve. The high frequency capacity curve is an exponentially decreasing curve. The low frequency and high frequency capacity curves will therefore intersect at one point. This point defines the critical stroke frequency and the corresponding capacity. When a certain jaw crusher operates on the critical frequency, the maximum capacity can be reached. The functions for critical frequency and corresponding maximum capacity are:

$$v_C = 47 * \frac{1}{(L_T)^{0.5}} * (\frac{R-1}{R})^{0.5} \tag{8}$$

$v_C$ = crusher critical frequency $[cycles/minute]$

$$Q_M = 2820 * W_J * (L_T)^{0.5} * (2 * L_{MIN,S} + L_T) * (\frac{R}{R-1})^{0.5} \tag{9}$$

$Q_M$ = maximum crusher capacity $[tonnes/hour]$

As can be seen from line Y2 in figure 7, an increase in reduction ratio leads to an increase in critical frequency. The reason is that a greater reduction requires more energy, which can be achieved by increasing the speed of the machine.

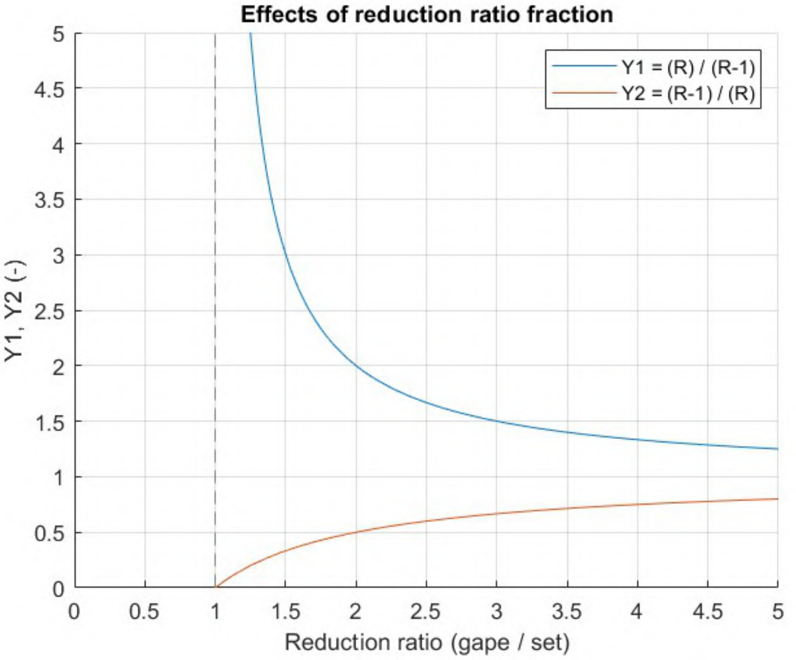

Figure 7: Effects of reduction ratio fraction

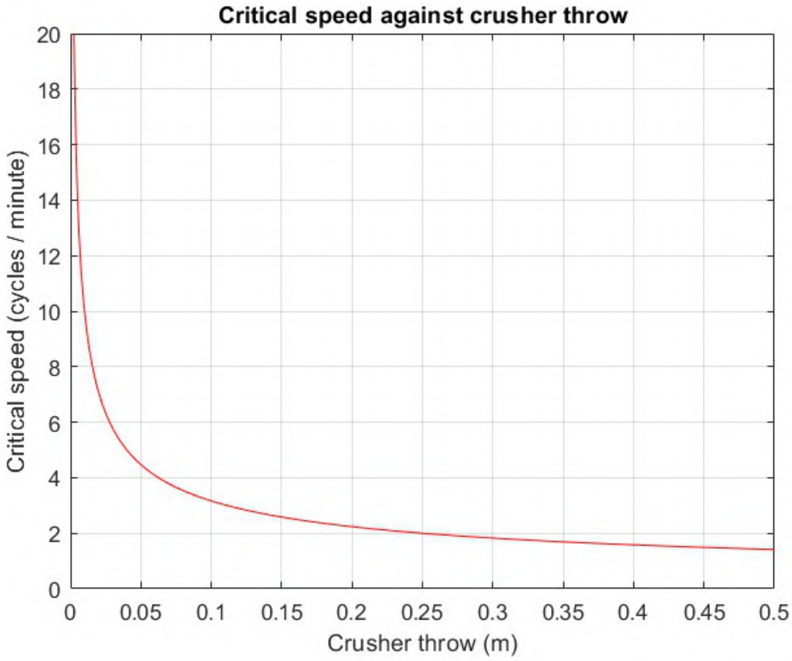

Figure 8: Critical speed against crusher throw

Figure 8 shows that the critical frequency decreases, when the crusher throw increases. The capacity not only depends on the properties of the jaw crusher itself, but also on the material being processed. The density of the material and the surface properties must also be taken into account. Furthermore, the bulk density will also change during the crushing process, so that the size distribution of the feed and the ratio between set and mean feed size must be taken into account. These relationships can be described by means of functions ($f(P_K)$, $f(\beta)$):

$$P_K = \frac{D_{MAX,F} - D_{MIN,F}}{D_{MEAN,F}} \tag{10}$$

$P_K$ = packing characteristics $[-]$
$D_{MAX,F}$ = maximum size of feed particles $[m]$
$D_{MIN,F}$ = minimum size of feed particles $[m]$
$D_{MEAN,F}$ = mean size of feed particles $[m]$

$$\beta = \frac{set}{mean\ feed\ size} \tag{11}$$

$\beta$ = reduction ratio $[-]$

The relations between $P_K$, $f(P_K)$, $\beta$ and $f(\beta)$ can be found in graphs. Using these values, the maximum capacity, taking into account material properties and change in bulk density, will be:

$$Q_M = 2820 * W_J * (L_T)^{0.5} * (2 * L_{MIN,S} + L_T) * (\frac{R}{R-1})^{0.5} * \rho_S * S_C * f(P_K) * f(\beta) \tag{12}$$

$Q_M$ = maximum crusher capacity $[tonnes/hour]$
$\rho_S$ = material density $[kg/m^3]$
$S_C^*$ = parameter related to surface characteristics $[-]$

**Taggart's model**

During his research, Taggart [16] cited an emperical relationship that was capable to describe the capacity of a crusher, by only using the dimensions of the discharge aperture:

$$Q = 930 * W_A * L_{MAX,S} \tag{13}$$

$Q$ = crusher capacity $[tonnes/hour]$
$W_A$ = width of crushing aperture $[m]$
$L_{MAX,S}$ = maximum set distance $[m]$

Another way to determine the capacity of a jaw crusher is by means of Taggart's model. Taggart uses the 80 % reduction ratio of the feed material. This is the ratio of square mesh aperature which ensures that 80 % of the feed and 80 % of the product will be passed through the crusher. Together with the limiting reduction ratio, these are the most common ratios that are being used. The limiting reduction ratio is the ratio between the maximum feed size and the maximum product size. The 80 % reduction ratio, compared to the limiting reduction ratio, will offer a solution to problems occuring due to the presence of small amounts of coarse slabby material.

The reduction ratio depends on the size of the material being fed. A decrease in the size of the input particles will lead to a smaller reduction ratio. Because more material will pass through the crusher without being crushed, the total capacity will increase. Taggart defined the following relationship to couple the overall crusher capacity to the actual amount of material being crushed:

$$R_{80} = F_{80}/P_{80} \tag{14}$$

$R_{80}$ = reduction ratio of 80 % passing size $[-]$
$F_{80}$ = 80 % passing size of feed $[cm]$
$P_{80}$ = 80 % passing size of product $[cm]$

$$Q_R = Q * R_{80} \tag{15}$$

$Q_R$ = crusher reduction $[tonnes/hour]$
$Q$ = crusher capacity $[tonnes/hour]$

The crusher reduction also depends on the crushability of the material, as well as on the moisture content and the way of feeding. Therefore a comparative reduction can be formulated as follows:

$$Q_R = k_c * k_m * k_f * Q_{CR} \tag{16}$$

$Q_R$ = crusher reduction $[tonnes/hour]$
$k_c^*$ = crushability factor $[-]$
$k_m^*$ = moisture factor $[-]$
$k_f^*$ = feed factor $[-]$
$Q_{CR}$ = comparative reduction $[tonnes/hour]$

The comparative reduction is based on a benchmark. This is the crushing operation of dry thick bedded medium-hard limestone during uniform and full capacity feeding. In this case $K = 1$, and therefore $Q_R = Q_{CR}$.

Based on the fact whether or not scalping is conducted before crushing, different relations can be formulated. Scalping is referred to as the first screening process before crushing takes place. Scalping is suggested especially before jaw crushing since an increase in capacity and lifetime of wear parts can be realised, while at the same time energy consumption can be lowered. When dealing with large particles, scalping can avoid large particles getting stuck inside the crusher. On the other hand, when dealing with small particles, scalping can avoid fines to accumulate and increase peak stresses (especially with high-moisture materials).

When scalping is taking place before crushing, the following relation can be defined for the 80 % passing size of the feed and the 80 % passing size of the product:

$$F_{80}(scalped\,feed) = F_{80}(unscalped\,feed) + 0.2 * X_S \tag{17}$$

$$F_{80}(scalped\,feed) = 0.8 * S_F * D_F + 0.2 * X_S \tag{18}$$

$$P_{80} = 0.8 * S_F * D_P \tag{19}$$

$X_S$ = crusher set $[cm]$
$S_F$ = shape factor $[-]$
$D_F$ = aperture of feed screen $[cm]$
$D_P$ = aperture of product screen $[cm]$

Equation 17 shows that the size of ore passing 80 % of unscalped ore equals the size of the same cumulative percent of scalped ore plus 0.2 times the aperture of the scalping screen. Equation 18 uses the approximation for the 80 % passing size of the unscalped feed.

Using the relationships mentioned above, the data can be compared to the existing crushing operation or dry thick bedded medium-hard limestone during uniform and full capacity feeding. This data is presented in an existing graph created by Taggart. From this comparative reduction, the required dimensions for the crusher design can be determined. Based on the gape size, the comparative reduction tonnage can be read from the graph. Equations 15 and 16 can then be used to translate this back to the crusher capacity.

### Broman's model

Broman's model [17] bases the capacity of a crusher on the amount of available space inside the crusher. The capacity depends on the size of the top surface and the height. The height can be calculated by considering the nip angle of the crusher jaw and the throw. The nip angle refers to the angle between the fixed and movable jaws at their closest point of approach. Trigonometry relations can be used to determine the height for each section within the geometry using the Tangent function. The area can then be approximated by the following equation:

$$A_{CF} = (L_{MAX,S} - \frac{L_T}{2}) * \frac{L_T}{tan(\alpha_N)} \tag{20}$$

$A_{CF}$ = area of crusher fraction $[m^2]$
$L_{MAX,S}$ = maximum set distance $[m]$
$L_T$ = crusher throw $[m]$
$\alpha_N$ = nip angle $[-]$

For the sake of completeness, this equation also takes the share of the throw on the total surface area into account. However, since this term is significantly smaller than the open side setting of the crusher, this term can be neglected. When the calculations are applied to the entire space inside the jaw crusher, the total capacity can be approximated by the following equation:

$$Q = \frac{3600 * W_{CC} * L_{MAX} * L_T * k * v_{FW}}{tan(\alpha_N)} \tag{21}$$

$Q$ = capacity $[m^3/hour]$
$W_{CC}$ = width of the crushing cavity $[m]$
$v_{FW}$ = angular velocity crusher flywheel $[1/s]$
$k^*$ = constant dependent on material being crushed (between 1.5 - 2.5) $[-]$

As can be seen in figure 9, the crusher capacity decreases as the nip angle increases. This observation can be explained by the fact that the jaw acts as a guide for the particles to move downwards. When the nip angle is too large, particles are prevented to move downwards due to friction with the jaw. Since the angle of nip has a range between 0 and 90 degrees ($\pi/2$ radians), the capacity will become 0 when the nip angle reaches 90 degrees. This is because the particles cannot fall further down, as they are not at an angle. The theoretical infinite capacity can be reached when the nip angle is 0, and the particles can move through the crusher without contact with the jaw.

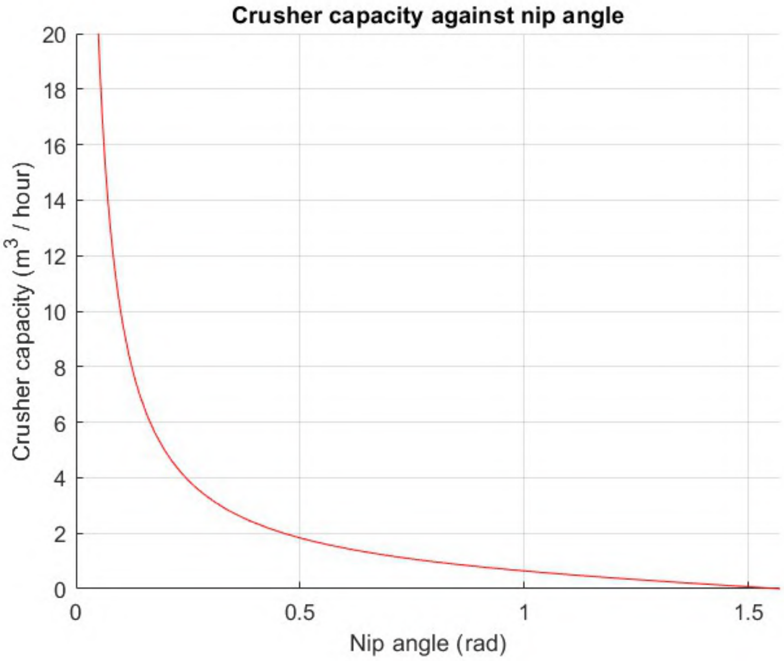

Figure 9: Crusher capacity against nip angle

It is important to keep in mind that this equation is only valid for crusher speeds below the critical speed. The definition and influence of the critical speed will be discussed in more detail at the end of this section.

### Michaelson's model

Michaelson [16] made use of the phenomenon that a complex mixture of sediment and fluid flows downslope by means of gravity. His relation is based on the width of the jaw, the minimum gape size, the throw, the speed of the material flow and a constant based on the shape of the jaw and the way of feeding. Michaelson's equation is limited to one material flow and is therefore not considered in this paper. However, equation 13 can be used as a simple approximation for the flow.

### Comparison of capacity models

All previously mentioned models tempt to estimate higher throughputs than prescribed by jaw crusher manufacturers. Especially Hersam's and Broman's model overestimate the throughput by a considerable amount. The surface characteristics of a jaw crusher play an important role in Rose and English's model. When the surface parameter is chosen too high, this leads to an overestimation of the capacity. When a lower surface parameter is used, resulting capacities tempt to agree well with the manufacturer's prescriptions. Rose and English's model takes a considerable amount of calculation steps and parameters needed. Michealson's model and the flow model quoted by Taggart show reasonable agreement with prescribed manufacturer capacities. Both models show high values for the crusher capacity, where the flow model tempts to overestimate capacity slightly more compared to Michaelson's model. However, the two models offer a straightforward way of calculating capacity. When a more detailed approach is desired, Rose and English's model can be used. This model provides values that correspond well with the capacity prescribed by manufacturers, as long as the correct value for the surface characteristics constant is used.

### Jaw crusher critical speed

The critical speed of dynamic equipment is normally referred to as the rotational speed that causes the natural frequency to be excited. This specific frequency causes the system to increase oscillating by a considerable amount without driving forces being present. In this case however, the critical speed is referred to as the operating speed in which the highest capacity can be reached. The capacity tempts to increase when the operation frequency is increased [14]. The capacity will increase until the critical operating speed is reached. When the frequency increases beyond the critical operating speed, the capacity will decrease. It is therefore important to determine the critical operating speed, in order to maximize capacity. In order to determine the critical speed, a geometric analysis will be carried out. In this analysis it will be assumed that particles inside the crusher can travel freely due to gravity in between successive compactions. By determining both the distance travelled and the time in which the distance could be travelled, the critical speed can be obtained. The geometric analysis that follows:

$$\frac{L_T}{h} = \frac{L_G - (L_{MIN,S} + L_T)}{2 * L_G} \tag{22}$$

$L_{MAX,S}$ = minimum set distance $[m]$
$L_{MIN,S}$ = maximum set distance $[m]$
$L_T$ = crusher throw (= $L_{MAX,S}$ - $L_{MIN,S}$) $[m]$
$h$ = particle distance travelled $[m]$
$L_G$ = gape size $[m]$

Here $h$ is determined by the standard formula for accelerated movements as well as the time within which this distance is covered. When $v$ is the number of cycles per minute, then the time for one complete cycle is $[60/v]$ seconds and the time for half a cycle is $[60/2v]$. Thus t will be the distance that a material travels during this period. This leads to the following equation:

$$h = \frac{1}{2} * a * t^2 = \frac{1}{2} * a * (\frac{30}{v})^2 = \frac{4414,5}{v^2} \tag{23}$$

$a$ = acceleration due to gravity $[m/s^2]$
$t$ = time $[s]$
$v$ = crusher frequency $[1/s]$

When equating $G$ to $R * L_{MIN,S}$, using equation 5 to estimate the throw and neglecting the square term, the following equation for the critical speed van be found, which is the same equation 8:

$$v_c = 47 * (L_T)^{-0,5} * (\frac{R-1}{R})^{0,5} \tag{24}$$

$R$ = reduction ratio $[-]$

Equation 24 shows two important factors influencing the critical speed. First of all the effect of the throw on the critical speed. Since the exponent above $L_T$ is negative, this indicates that when the throw is decreased, the critical speed will increase. Furthermore, it can be seen that for reduction ratios higher than 1 (which should always be the case), the term increases. In other words, when the reduction ratio is increased, the crusher will have a higher critical speed.

However, equation 24 tempts to give an underestimation of the critical speed when the size of the gape is too small or too large. Therefore, Rose and English [15] and Kelly and Spotiswood [18] came up with a different relation to determine the optimal speed of the crusher. This relation is only based on the gape size and contains a margin of error:

$$v_{OPT} = 280 * e^{-0{,}212 * L_G^3} \pm 20\% \tag{25}$$

$v_{OPT}$ = optimal crusher speed [$rotations\ per\ minute$]
$L_G$ = gape size [$m$]

As can be seen from figure 10, the optimal crusher speed decreases when the gape size increases. The plot includes the main curve in red and the 20 % error margin bounded by the two dotted black lines. The optimal speed remains approximately the same for a gap size between 0 and 0.5 metres. Between 0.5 and 1 meter, the optimal speed of the crusher will have a steeper decreasing slope. At a gape size of 1 meter the steepest slope is reached and this slope is maintained until a gape size of around 2 meters is reached. From 2 to 3 metres, the optimal speed decreases less quickly and reaches the value 0 with a gape size of approximately 3 metres.

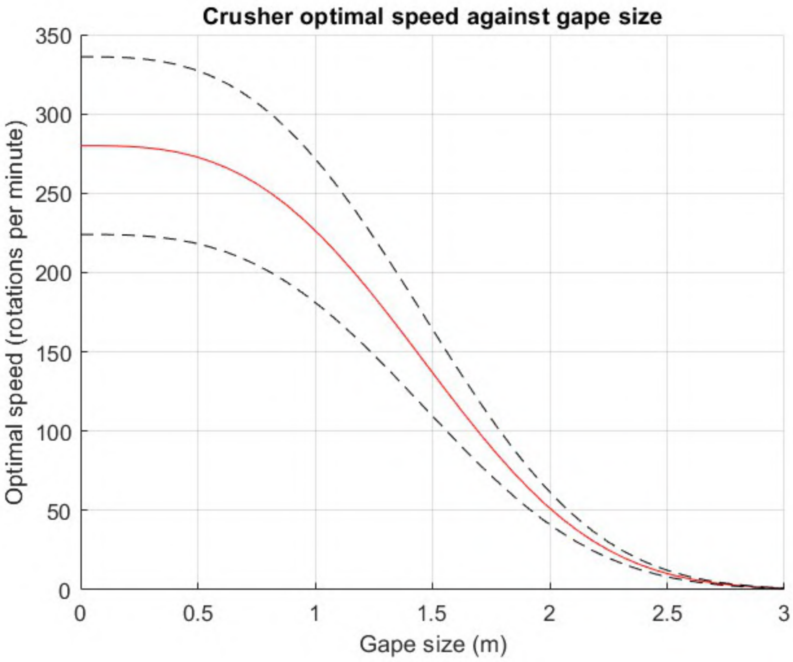

Figure 10: Crusher optimal speed against gape size

Apart from the model mentioned previously, different researchers described other equations to calculate the critical crusher speed based on different geometrical parameters. For example, Broman [17] stated that the critical speed is a function of the throw and the nip angle:

$$v_c = \frac{66{,}6}{\sqrt{\frac{L_T}{tan(\alpha_N)}}} \tag{26}$$

$v_c$ = critical crusher speed [$rotations\ per\ minute$]
$L_T$ = crusher throw [$m$]
$\alpha_N$ = nip angle [$-$]

### Jaw crusher power consumption

An important parameter in crusher design is the estimated power consumption. Several scientists have conducted research to find an estimate for this power consumption. The particle size distribution plays an important role in almost all research. Both the size of the particles and the ratio between feed size and product size are included in the equations.

Most methods that are being used to approximate the power consumption use Bond's work index. Numerically, the work index represents the energy [kWh / short tonne] required to reduce the material of one short tonne from a theoretically infinite feed size to a size at which 80 % of the material passes through a sieve with an aperture of 100 [µm] in both directions. Bond's standard procedure uses a dry grinding process inside a closed circuit ball mill to achieve a circulating load of 250 %. The method can be transferred to metric tons by multiplying with a factor of 1,1. The Bond work index for the procedure is calculated using the following equation [19]:

$$W_I = 1,1 * \frac{44,5}{{P_c}^{0,23} * m_s^{0,82} * (\frac{10}{\sqrt{P_{80}}} - \frac{10}{\sqrt{F_{80}}})} \tag{27}$$

$W_I$ = work index $[kWh/tonne]$
$P_c$ = test sieve mesh size $[\mu m]$
$m_s$ = mass of material passing through screen per mill rotation $[gram/rotation]$
$P_{80}$ = 80 % passing size of product [µ$m$]
$F_{80}$ = 80 % passing size of feed [µ$m$]

Rose and English [15] derived a method to estimate the power consumption by using Bond's work index. This led to the following equation:

$$P = 10 * W_I * Q * (\frac{1}{\sqrt{P_{80}}} - \frac{1}{\sqrt{F_{80}}}) \tag{28}$$

$P$ = power $[kW]$
$Q$ = crusher capacity $[tonnes/hour]$

Based on a large set of data gathered, $F_{80}$ was found to be approximately equal to 0,7 times the largest particle size in the feed. The relationship established also includes the fact that feed particles inside a jaw crusher should never be larger than 0,9 times the size of the gape. Therefore the following equation for $F_{80}$ can be formulated:

$$F_{80} = 0,9 * L_G * 0,7 = 0,63 * L_G \tag{29}$$

$L_G$ = gape size $[m]$

The largest particle size being discharged from the bottom of the crusher will take place when the set is fully opened. Again, taking into account that $P_{80}$ will be equal to 0,7 times the largest particle size in the product stream, the following equation can be formulated for $P_{80}$ :

$$P_{80} = 0,7 * (L_{MIN,S} + L_T) \tag{30}$$

$L_{MIN,S}$ = minimum set distance $[m]$
$L_T$ = crusher throw $[m]$

Using the fact that maximum power draw will take place during running at the critical speed, equation 12 to determine the maximum capacity, together with equation 29 and equation 30 can be filled into equation 28 to determine the maximum power draw during operation at the critical speed:

$$P_{MAX}=67{,}4*W_J*W_I*L_T^{0{,}5}*(L_{MIN,S}+\frac{L_T}{2})*(\frac{R}{R-1})^{0{,}5}*\rho_S*(\frac{\sqrt{L_G}-1{,}054*\sqrt{L_{MIN,S}+L_T}}{\sqrt{L_G}*\sqrt{L_{MIN,S}-L_T}})*\rho_S*S_C*f(P_K)*f(\beta) \qquad (31)$$

Lynch [20] derived a method to calculate the power consumption based on the ratio of material being crushed and the amount of material passing through without being crushed. This indicates that the power supply depends on the fraction of material that is being crushed. In order to determine an estimation for the power consumption, the following size parameter has been defined:

$$C_{SP} = 25,4 * \sum_{i=1}^{n} \frac{t_i}{S_i + S_{i+1}} \qquad (32)$$

$C_{SP}$ = size parameter $[-]$
$t_i$ = the $i$th element of a size distribution $[\text{µ}m]$
$S_i$ = the lower limit of the $i$th fraction $[\text{µ}m]$
$S_{i+1}$ = the upper limit of the $i$th fraction $[\text{µ}m]$

This equation takes multiple size distributions of the feed particles into account. By determining the amount of material crushed per material fraction and multiplying it with the overall percentage of mass retained within the fraction, values for the $i$th element of a size distribution can be found. Dividing this by the sum of the lower and upper limit of the size interval, summing overall fractions and multiplying by a constant, leads to a value for size parameter $C$. When a value has been found for the size parameter $C$, the following equation can be formulated for the overall required Amperage for the crusher:

$$I = 0,0035 * C_{SP}^2 + 0,0822 * C_{SP} + 14,2 \pm 1,8 \ [A] \qquad (33)$$

I = required crusher Amperage $[A]$

When both the Amperage and the Voltage of the crusher are known, their values can be multiplied in order to determine the overall power consumption. The required Amperage (and thus the power consumption) depends on both the reduction ratio and the initial particle size distribution of the feed. A higher reduction ratio and a larger particle size distribution lead to a higher value for the size parameter $C$. As can be seen in figure 11, an increased value for the size parameter will lead to a higher required Amperage and thus an elevation in power consumption.

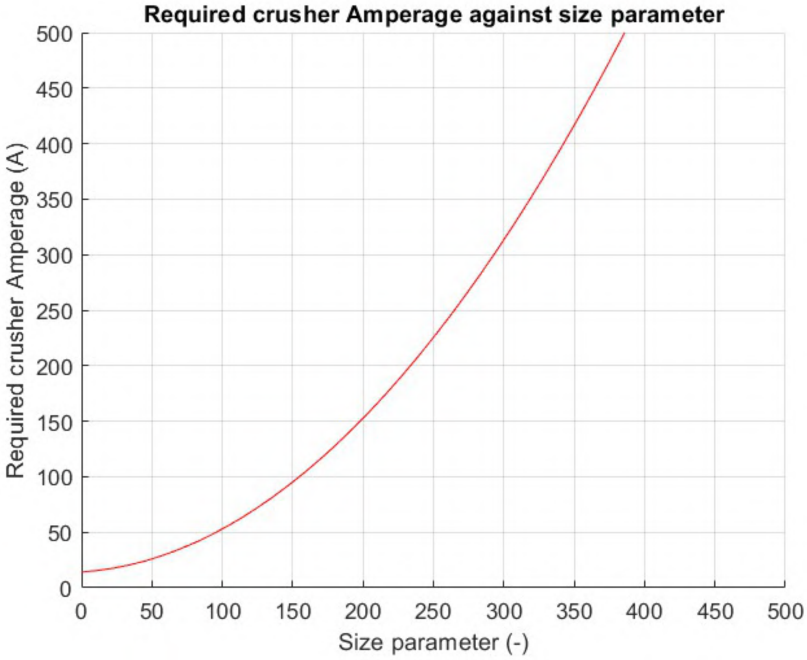

Figure 11: Required crusher Amperage against size parameter

Finally, Morrel [21], Anderson and Napier Munn [22] determined a model to estimate the power consumption of a jaw crusher. Even though previous models showed corresponding results to true crusher power consumptions, the models are not fully representational. The reason for this is the fact that they make use of Bond's work index (equation 67). This expression is based on the concept of a tumbling mill. However, forces inside a tumbling mill are different than those inside crushers. Therefore, Morell, Anderson and Napier Munn based their power consumption calculations on a pendulum test under load and no load. The equation is based on the fact that the crusher power draw is a function of the energy required to run both under load and under no load. The power draw is also dependent on the particle size distribution of the feed. By dividing the overall particle size distribution in different intervals, the following equation determines the pendulum power draw in order to cause breakage of the $i$th interval:

$$P_P = \sum_{i=1}^{j} Ecs_{T(10)} * P_i * m_i \tag{34}$$

$P_P$ = pendulum power draw (dependant on running time) $[kW]$
$Ecs_{T(10)}$ = energy required to crush particles of size $i$ ($Ecs$ at $T_{10}$ percent) $[kW/tonne]$
$P_i$ = breakage probability of particles of size $i$ [-]
$m_i$ = mass flow of particles of size $i$ $[tonnes/hour]$

The actual crusher power draw is based on a combination of energy consumed during idle movement and a certain scale factor times the power consumption required for breakage. When these two values are added together, an estimation can be made for the actual power draw during loading. This will lead to the following equation, where $S_f$ can be determined by crusher regression data:

$$P_A = S_f * \sum_{i=1}^{j} Ecs_{T(10)} * P_i * m_i + P_N \tag{35}$$

$P_A$ = actual crusher power draw [kW]
$S_f$ = scaling factor depending on crusher [-]
$P_N$ = crusher power draw during no load [kW]

## 3.2 Gyratory and cone crusher

Another large series of equipment to conduct comminution operations using the compression loading mechanism are gyratory crushers (figure 5b) and cone crushers (figure 5c). As mentioned earlier, gyratory and cone crushers have a similar design. Both crusher types are used to break down large rocks into smaller progenies. When the required throughput is 900 tonnes per hour or more, gyratory crushers are always the preferable option. Gyratory crushers have larger crushing chambers and operate at lower speeds compared to cone crushers. Gyratory crushers are mainly used for direct feed from a mine to reduce large pieces of material into smaller progenies, since they are better capable of dealing with a less uniform particle size distribution compared to cone crushers. In many cases, a so-called grizzly screen is added before the feed into the crusher. This screen ensures that chunks larger than the gape do not get stuck in the crusher chamber. Gyratory crushers are, due to their purpose, designed in a more robust form compared to cone crushers. Cone crushers are mainly used as a subsequent reduction step to further reduce the size of the already crushed particles. Due to the conical shape of cone crushers, smaller rocks can be crushed, since travelling time through the crushing chamber will be increased.

A gyratory crusher consists of a high strength cylindrical frame (concave) in which a cone is located. This cone consists of a main shaft with a mantle and is driven by a motor that is connected to an actuating mechanism by means of various gears. The actuating movement causes a size change of the crushing chambers. Since the gap between the mantle and concaves decreases, size reduction of the material will take place during downwards movement. To withstand the great crushing forces, the concaves of the chamber are covered with wear-resisting plates consisting of hardened steel. The actuating cone is attached to a so-called spider at the top, which acts as a pivot point and ensures that the cone remains in position.

The gyratroy crusher is equipped with a so-called: 'hydro set', which ensures that the height of the main shaft can be adjusted. Since the mantle has a conical shape, the size of the discharge gap can be adjusted as the height of the mantle is changed. This allows the maximum output size to be set as desired. The shaft undergoes an ellipsoidal motion which is caused by an eccentric bushing. Due to the off-centre fabrication of the bushing, the lower shaft will rotate in an elliptical manner, which causes an open-close fluctuation of the throw, and thus a crushing action.

A cone crusher is similar in design compared to a gyratory crusher. The cone crusher consists of a moving mantle, which, like a gyratory crusher, moves in an off-centered motion inside a concave. As a result, the gap at the bottom of the crushing chamber keeps changing in size. This size varies from the smallest (closed side setting) to the largest (open side setting). As a result, the maximum final size of the progenies is determined by the open side setting. A cone crusher consists of a mantle with a lower inclination compared to a gyratory crusher. Other differences between the two are the travelling speed of the mantle and the location of the pivot point. Since a cone crusher has a higher speed and a greater arc of gyration, the chances of a material to be crushed at least once when passing through the crushing chamber increase. The steep slope of the cone crushers also causes the pivot point to be below the distributor plate, while in a gyratory crusher, the pivot point will be the spider cap. This causes the cone crusher to have movement around the surface of the mantle, while for a gyratory crusher, this movement is mainly taking place at the bottom of the mantle. Therefore gyratory crushers are designed to crush only the largest amounts of material, while letting pass most material uncrushed. Cone crushers are designed as a further reduction step, where the particle size distribution of the end product will be more uniform.

A distinction can be made between primary, secondary, tertiary and quaternary crushers. In general, the first reduction step takes place by means of a gyratory crusher, ensuring that only the largest particles of the stream are reduced. Secondary crushing then takes place by means of cone crushers. These are equipped with stepped liners to ensure optimum nip angles are maintained throughout the chamber, thus preventing excess material slippage. Tertiary and quaternary crushing takes place by means of cone crushers with a short head and a large nip angle, ensuring that the time of residence of the material in the crusher chamber is increased and the material is therefore further reduced. Depending on the size of the set, the maximum output size can be determined.

Based on the stage of the crushing process, an open or closed circuit is chosen. With an open circuit, the material only passes through the crushing chamber once. In a closed system, the material is sieved after crushing and the larger pieces of material that are not able to pass through the screen are returned to the crusher. During primary crushing, an open system is chosen so that only the largest pieces of material will be crushed. A grizzly screen is generally placed before the primary crusher, so that large pieces of material are prevented from getting stuck in the crusher. A closed circuit is used for the follow-up crushing stages. The secondary crusher is connected in series with the primary crusher, so that the material can flow through immediately.

### 3.2.1 Gyratory and cone crusher dimension design

The most important parameters for determining the dimensions of a gyratory crusher are [23]:

$$Gape\ size = 1.1 * Largest\ particle\ size \qquad (for\ crushers\ with\ d\ < 2\ [m]) \tag{36}$$

$$Ratio\ of\ mantle\ diameter\ to\ gape = 1.3 - 1.7 : 10 \tag{37}$$

$$Outer\ circumference\ crusher = \begin{cases} 8 - 10 * gape\ size, & \text{if } d < 0.66\ [m] \\ 6.5 - 7.5 * gape\ size, & \text{if } d > 0.66\ [m] \end{cases} \tag{38}$$

$d$ = diameter of largest particle in size distribution $[m]$

The performance of gyratory and cone crushers depends on several factors. First of all, the composition of the material is important. For example, a distinction can be made between rocks with a different kind of hardness. Depending on the hardness, a work index can be determined. This work index indicates how much energy is required per quantity of material for reduction to take place. This concept has already been discussed in the previous section. Other factors that affect crusher performance are moisture and fines content. Because crushing normally takes place under dry conditions, adding moisture is unnecessary. However, water can be used to remove encrusted materials from the crusher geometry. It is important that the amount of moisture and fines does not exceed 10 % of the total mass. Finally, the crusher performance is influenced by feed parameters such as the way of feeding (choke feed compared to non-continuous feed) and the particle size distribution of the feed. The particle size distribution of the feed also depends on whether an open or closed circuit is used.

An important parameter in the operational performance of a gyratory or cone crusher is the speed at which the crushing head is excited (also known as gyrating speed). The gyrating speed is inversely proportional to the size of the particles fed into the crusher [24], [25]. In other words, the larger the feed size, the lower the gyration speed of the head. This also explains the reason why gyratory crushers (primary) operate at lower gyrating speeds compared to cone crushers (secondary). To produce a particle size distribution with largest particle size $d$, a minimum crusher speed is required. This speed can be determined by the following formula [26]:

$$v \geq \frac{665\ (sin(\theta_C) - \mu * cos(\theta_C))}{\sqrt{D}_{MAX,P}} \tag{39}$$

$v$ = crusher frequency [$cycles\ per\ minute$]
$\theta_C$ = inclination angle of the cone [$-$]
$\mu$ = friction coefficient [$-$]
$D_{MAX,P}$ = maximum size of crusher product [$cm$]

It follows from the equation that the smaller the required maximum particle size, the higher the critical speed will have to be. Furthermore, figure 12 shows the minimum rotation speed required to produce particles of a certain maximum size versus the inclination angle of the cone to the horizontal. A value of $\mu = 0,25$ has been chosen. It can be seen that the larger the inclination angle, the higher the critical speed. An explanation for this is the fact that a steeper slope causes particles to fall down faster. This increases the flow, but leads to the crushing operation to take place less efficiently. By increasing the critical speed, more crushing cycles will take place per unit of time. As a result, a higher critical speed is required for a larger inclination angle.

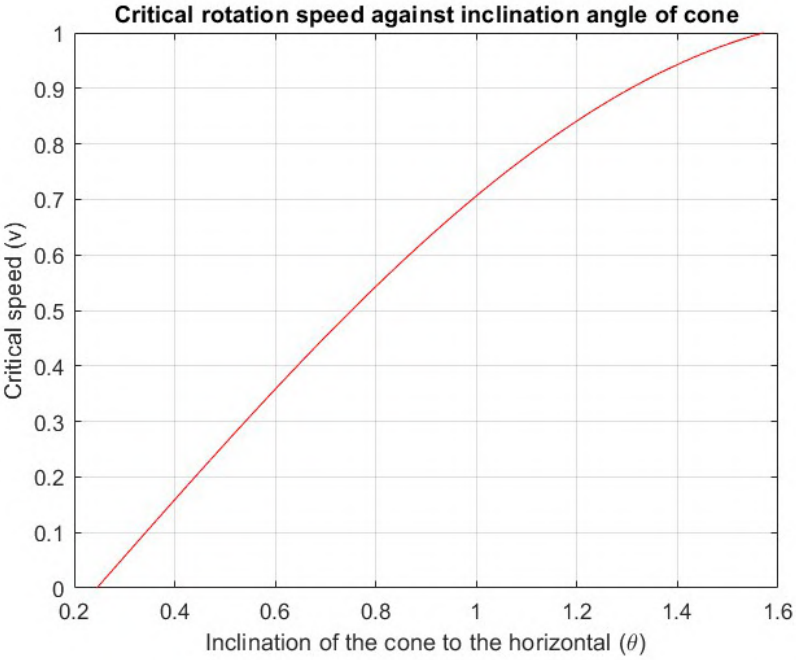

Figure 12: Critical speed against inclination angle of cone

### 3.2.2 Gyratory & cone crusher capacity

The loading mechanisms between a jaw crusher and a gyratory or cone crusher are similar. The only difference is that the geometry where crushing takes place is different. For example, the material is crushed between two plates (wedges) in a jaw crusher. In a gyratory or cone crusher, the geometry can be seen as a spiral in which crushing takes place. In addition, the entire surface of a jaw crusher is used during a cycle. Since the crushing head of a gyratory and cone crusher gyrates, crushing takes places at only one half of the geometry. Because the crushing principles are the same, the models to calculate crushing capacity are similar to those described in the previous section.

### Hersam's model

One of the formulated models is the empirical relationship described by Hersam [27]. This expression is only partially applicable for gyratory and cone crushers, because the results do not correspond to the actual crusher capacity. It is expected that the constant related to the crusher characteristics is the cause of this discrepancy. Hersam's model will therefore not further be described.

### Gauldie's model

Gauldie [24], [25] formulated an equation to calculate the crusher optimum capacity based on the distance between crusher head and concave, the angle of inclination of the crushing head and the distance traveled by the material during a single crushing cycle:

$$Q_O = 0.35 * \pi * sin(\theta_C) * (L_{MAX,C} + L_{MIN,C}) * g * H_C * (sin(\theta_C) - \mu * cos(\theta_C))^{0.5} \tag{40}$$

$Q_O$ = optimum crusher capacity $[m^3/s^2]$
$\theta_C$ = inclination angle of the cone $[-]$
$L_{MAX,C}$ = maximum distance between crushing head and concave $[m]$
$L_{MIN,C}$ = minimum distance between crushing head and concave $[m]$
$g$ = gravity constant $[m/s^2]$
$H_C$ = vertical length of crushing chamber $[m]$

This method is strenuous to apply because the angle of inclination of the crushing head is difficult to determine in practice.

### Broman's model

Similarly for calculating the capacity of jaw crushers, Broman [17] has developed a model for calculating the capacity of gyratory crushers and cone crushers. It is important for the validity of the model to keep in mind that the crushing frequency does not exceed a critical value, since this will lead to a decrease in capacity. The formula is based on the dimensions of the crusher, the crushing cycle time and the distance covered during one crushing cycle:

$$Q_V = \frac{(D_M - L_{MIN,C}) * \pi * L_{MIN,C} * L_T * 60 * N * K}{tan(\theta_C)} \tag{41}$$

$Q_V$ = volumetric crusher capacity $[m^3/hour]$
$D_M$ = outer diameter of mantle at bottom shell $[m]$
$L_{MIN,C}$ = minimum distance between crushing head and concave $[m]$
$L_T$ = crusher throw $[m]$
$N$ = amount of cycles per minute $[-]$
$K^*$ = material constant (varies between 2 and 3) $[-]$
$\theta_C$ = inclination angle of the cone $[-]$

Similar to the calculation of the jaw crusher capacity, this formula takes into account the open and closed side settings at the discharge opening of the crusher, the speed of actuation, a material constant and the angle of the crushing body.

**Rose and English's model**

The model developed by Rose and English for calculating the capacity of jaw crushers [15] can, with a few modifications, also be applied to gyratory and cone crushers:

$$Q = \frac{W_I * D_B * \rho_S * \sqrt{L_{MAX,C} - L_{MIN,C}} * (L_{MAX,C} + L_{MIN,C}) * K}{2 * \sqrt{\frac{R}{R-1}}} \tag{42}$$

$Q$ = crusher capacity $[m^3/hour]$
$W_I$ = work index $[kWh/tonne]$
$D_B$ = bowl diameter at given cross-section $[m]$
$\rho_S$ = material density $[kg/m^3]$
$L_{MAX,C}$ = maximum distance between crushing head and concave $[m]$
$L_{MIN,C}$ = minimum distance between crushing head and concave $[m]$
$K^*$ [0.5 - 1.0] = statistical factor $[-]$ (0.5 for soft materials and 1.0 for harder materials)
$R$ = reduction ratio $[-]$

### 3.2.3 Gyratory & cone crusher power consumption

The total power consumption depends on the capacity and the amount of energy required per amount of material (work index). It is also important whether the crusher operates in primary or secondary mode. Normally the following rule of thumb applies to crushers:

$$P = Q * W_I * K \tag{43}$$

Here $P$ is the crusher power $[kW]$, $Q$ is the crusher capacity $[tonnes/hour]$, $W_I$ is the work index $[kWh/tonne]$ and $K^*$ is a constant. $K = 0.75$ $[-]$ for primary crushers and $K = 1$ $[-]$ for secondary crushers.

To determine a better estimation of the power consumption, the capacity of the crusher, the work index of the material and the comminution parameters are important. As described earlier, the work index indicates the relationship between the amount of energy put into a particle of a known size and, the reduced particle size after the comminution operation. Therefore the work index specifies how hard a certain material is and indicates the resistance of the material to a crushing operation. The comminution parameters indicate the feed size to the crusher at which 80% of the material passes through a sieve with the given opening size and the product size at which 80% of the material passes through a sieve with the given product size.

**Rose and English's model**

Rose and English [28] used the same format to calculate the power consumption of gyratory and cone crushers as they used to calculate the power consumption of jaw crushers. Both equations include the same parameters, where only the arrangement is different. This concerns the following equation, which is the same as equation 28:

$$P = W_I * Q * \frac{\sqrt{F_{80}} - \sqrt{P_{80}}}{\sqrt{F_{80}}} * \sqrt{\frac{100}{P_{80}}} \tag{44}$$

$P$ = power $[kW]$
$W_I$ = work index $[kWh/tonne]$
$Q$ = crusher capacity $[tonnes/hour]$
$F_{80}$ = 80 % passing size of feed $[\mu m]$
$P_{80}$ = 80 % passing size of product $[\mu m]$

Figure 13 shows the effect of different particle sizes on the power consumption. It can be noticed that high size values for the feed and low size values for the product lead to the highest power consumption. This can be explained by the fact that the power consumption scales with the amount of reduction:

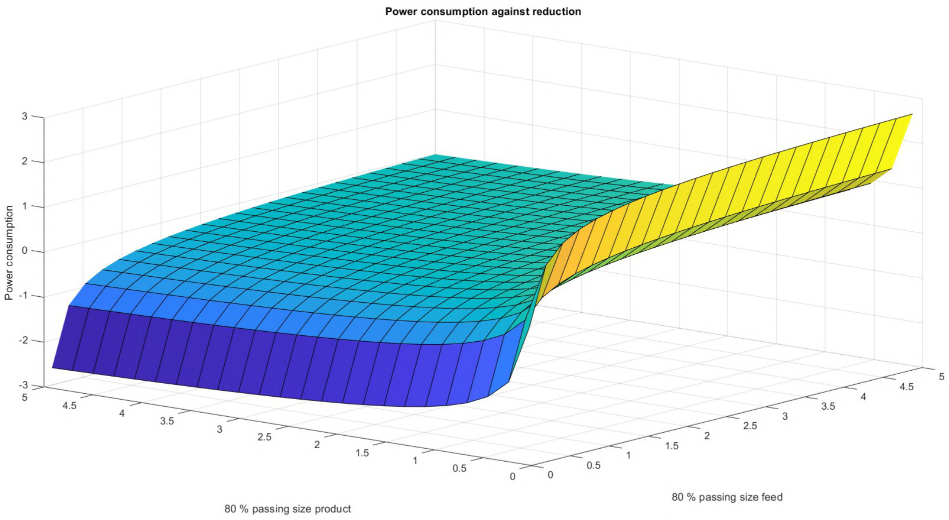

Figure 13: Power consumption against reduction

To calculate the power consumption, the capacity calculated with equation 42 can be used directly. When the work index is not known in advance, a rough estimate can be made by using a value for the average impact strength in the following equation [29]:

$$W_I = \frac{0.0485}{\rho_S} \tag{45}$$

$W_I$ = work index $[kWh/tonne]$
$Numerator^*$ = 0.04585 = average impact strength $[J/m]$
$\rho_S$ = material density $[kg/m^3]$

It is remarkable to notice that the work index is dependent on the density of the material and decreases when the density of the material increases.

### Motz's model

Motz [29] also derived an equation to estimate the power requirements of gyratory and cone crushers. Motz came up with a similar model as Rose and English which also depends on the work index and comminution parameters $F_{80}$ en $P_{80}$. The equation has been written in a different form, but is the same as equation 28 and equation 44:

$$P = \frac{10 * W_I * Q * (\sqrt{F_{80}} - \sqrt{P_{80}})}{\sqrt{F_{80} * P_{80}}} \tag{46}$$

## 3.3 Roll crusher

The last category of comminution equipment that use the compression loading mechanism are roll crushers. Roll crushers are commonly used as secondary crushers. In general, roll crushers consist of two rolls that face each other and rotate in opposite directions. One roll is attached to a driving mechanism by a gearbox or belt, while the other roll is moving by friction.

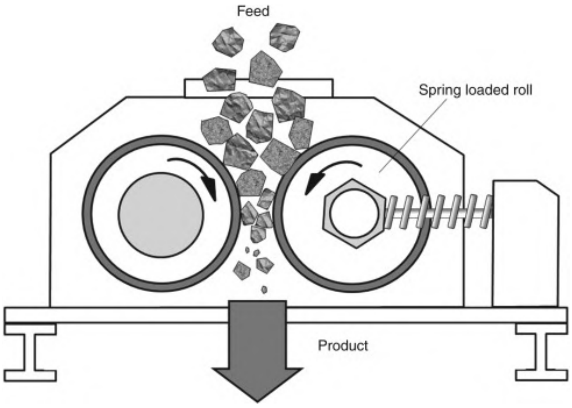

Figure 14: Roll crusher

The power consumption of the roll crusher generally depends on the capacity, the reduction ratio, the work index and the moisture content of the material. Depending on the desired particle fineness, rolls can be rigidly fixed or spring mounted. Since rigidly fixed rolls do not allow any movement of the rolls during crushing, finer particle sizes can be reached. Rolls can have different surfaces, depending on the material being crushed and the desired product size. For example, the surface can be smooth, grooved, toothed or corrugated. Toothed and corrugated surfaces are mainly used for crushing larger materials into smaller chunks, due to their ability of deep particle penetration. Also, non-smooth surfaces are more capable of nipping a particle inside the crusher due to increased friction between particle and roll surface. Smooth or grooved surfaces are mainly used for granulating and grinding operations of material chunks into fine particles.

During crushing, the material is fed at the top by means of a chute to ensure a good distribution of material on the surface of the rolls so that it covers two-thirds of the roll surface. It is important that the crusher is not choke fed, since this will cause an irregular particle size distribution. The material moves through the crusher by means of gravitational force. The particles smaller than the set will flow through the space between the rolls without being crushed. The particles larger than the set will first be crushed between the rolls, until they are small enough to fall through the set. After crushing, special scrapers are installed to remove any sticky material from the rolls. A sieve can be installed under the set to collect large particles to use as a feed for a new cycle through the crusher. Other combinations of roll crusher designs are also used where there is only one rotating roll rotating against a fixed plate. A separate, but very important category within the roll crushers is formed by the high pressure grinding rolls (HPGR's). In HPGR's, introduced by Schonert [30], [31], the rolls are pressed together with great forces, in order to let crushing take place more efficiently. More information about the operation and important design parameters of HPGR's will be given later in this paragraph.

### Roll crusher nip angle

An important parameter in roll crusher design is the nip angle. The nip angle is defined as the angle between the horizontal and the point where the feed comes into contact with the roll crusher surface. The nip angle depends on the size of the crusher and the surface characteristics and usually varies between 20° and 30°. The nip angle is important to ensure that the crusher is able to grab feed material and pull it in between the two crushing rolls. If the nip angle is not large enough, the material will not be pulled in properly, causing it to keep bouncing on the rolls. This causes a reduction in efficiency because the capacity will decrease and the supply to the crusher can become clogged. Together with the amount of friction and the roll geometric parameters, the nip angle is important to determine the maximum particle size.

### 3.3.1 Roll crusher dimension design

A distinction can be made between small roll crushers that rotate at high speeds and large, heavy duty roll crushers that rotate at lower speeds. For smaller crushers, the diameter of the roll varies from 228 $[mm]$ to 760 $[mm]$ and the face length is between 250 $[mm]$ and 460 $[mm]$. For larger heavy duty crushers, the diameter of the roll varies from 900 $[mm]$ to 1000 $[mm]$ and the face length is between 300 $[mm]$ and 610 $[mm]$.

In order to determine the geometry of the roll, it is important to know the particle size distribution of the feed. The radius of the roll can be calculated based on the distance between the rolls, the largest feed particle size and the nip angle of a particle that is about to be nipped (figure 15).

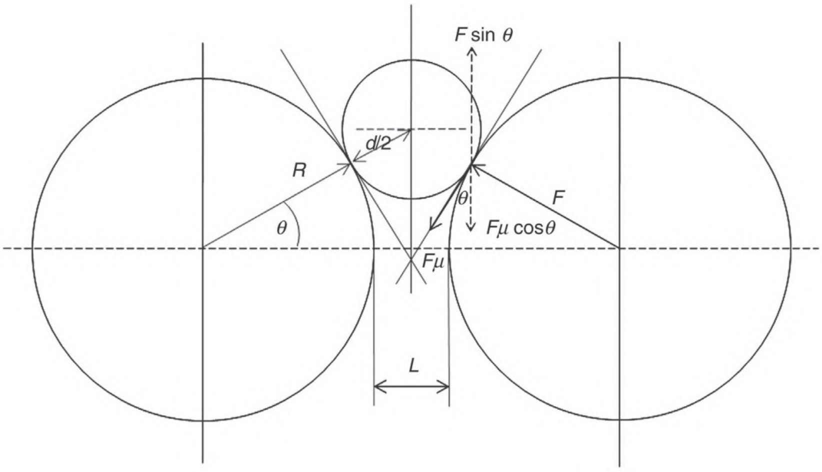

Figure 15: Roll crusher schematic view [2]

The following calculation to determine the radius of the roll is based on geometrical relations and will assume a smooth roll surface and spherical feed particles [2]:

$$\cos(\theta_N) = \frac{2 * R_R + L_R}{2 * R_R + d_{MAX}} \tag{47}$$

$$R_R = \frac{L_R - d_{MAX} * cos(\theta_N)}{2 * (cos(\theta_N) - 1)} \qquad for \qquad \theta \neq 2 * \pi * n \tag{48}$$

$R_R$ = radius of roll $[m]$
$L_R$ = distance between rolls $[m]$
$d_{MAX}$ = largest particle size $[m]$
$\theta_N$ = nip angle $[-]$

As can be seen from equation 48, in order to calculate the roll radius, the nip angle ($\theta_N$) is needed. However, the nip angle on its turn follows from the static coefficient of friction ($\mu_S$) between the feed material and the surface of the roll crusher. To be able to calculate the static coefficient of friction, the compressive force ($F_C$) between the geometry of the roll and the feed particle must be determined. This can be calculated by multiplying the compressive force of the crusher (in normal direction to the crusher surface) by the static coefficient of friction. When only the vertical components of this frictional force are considered and gravity is neglected, the following geometric relation follows during equilibrium just after nipping:

$$F_C * sin(\theta_N) = F_C * \mu_S * cos(\theta_N) \tag{49}$$

$$\theta_N = tan^{-1}(\mu_S) \tag{50}$$

$F_C$ = compressive force between crusher and feed particle [N]
$\theta_N$ = nip angle [-]
$\mu_S$ = static coefficient of friction [-]

According to equation 50 and following from the fact that most dry materials have coefficient of friction values ranging from 0.3 to 0.6, common values for nip angles will range from 17 ° to 31 °. [32]

However, since roll crushing is a dynamic operation, the static friction coefficient is not fully representative for the whole process. Therefore, the kinetic coefficient of friction ($\mu_K$) also needs to be taken into account. According to Wills [33], the kinetic coefficient of friction is dependent on the static coefficient of friction and the speed of the rotating rolls. Wills defined the following relation:

$$\mu_K = \frac{1 + 1.12 * v}{1 + 6 * v} * \mu_S \tag{51}$$

$\mu_K$ = kinetic coefficient of friction $[-]$
$v$ = crusher frequency $[rotations\ per\ minute]$

It can be seen from the equation that the value of $\mu_K$ decreases moderately if the rotating speed of the crusher is increased. When using an average static friction coefficient of 0.45, and calculating $\mu_K$ for 100 $[rpm]$ and 300 $[rpm]$, the value of $\mu_K$ changes from 0.0846 (at 100 $[rpm]$) to 0.0842 (at 300 $[rpm]$). Figure 16 shows the multiplier against the rotation speed of the rolls. It can be seen that for a rotation speed of 0, the kinetic coefficient of friction is equal to the static coefficient of friction. For low rotation speeds (less than one cycle per minute), the multiplier rapidly decreases to a value of 0.3. For speeds between 1 and 6 rotations per minute, the multiplier gradually decreases to a value of approximately 0.2. This asymptotic value will also be maintained for higher speeds.

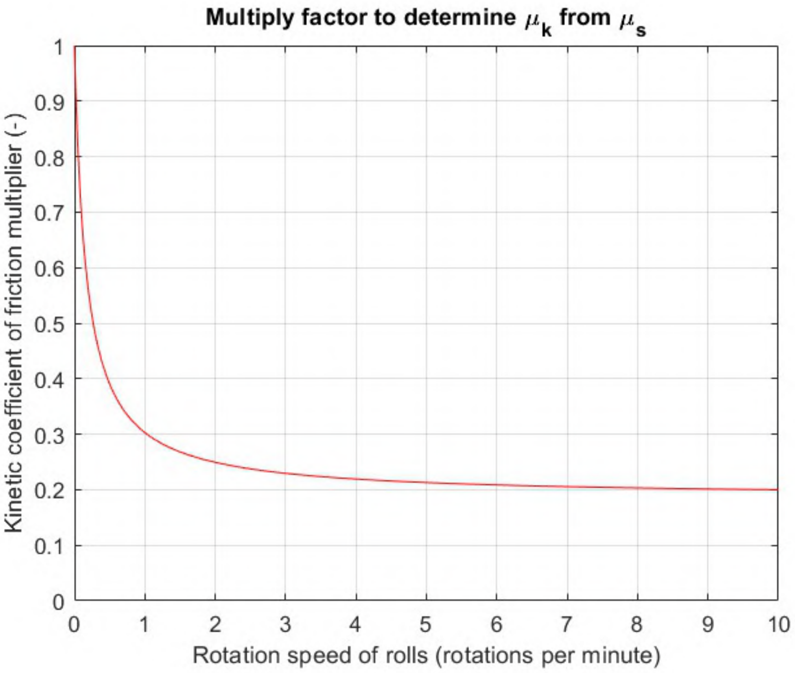

Figure 16: Friction coefficient multiplier

## Roll crusher capacity

In order to determine the suitable roll crusher for a desired operation, it is important that the capacity is known. The capacity of a roll crusher depends on its dimensions and its rotational speed. To guarantee the most efficient performance, the crusher needs to be continuously fed. It is important that the crusher is not being choke fed, since this can change the output to be irregularly sized. The feed also needs to have a moisture content that is as low as possible, so that clogging of the crusher can be prevented. However, a small amount of water can be added to the crusher, so that the surfaces can be kept clean. The use of a small amount of water is also beneficial when a fine product is desired. During continuous feed and operation, Wills [33] stated that the capacity of the crusher can be approximated by the following formula:

$$Q = 60 * \pi * D_R * W_R * \omega * L_S * \rho_B \tag{52}$$

$Q$ = crusher capacity $[tonnes/hour]$
$D_R$ = roll diameter $[m]$
$W_R$ = roll width $[m]$
$\omega$ = rotational speed $[rotations\ per\ minute]$
$L_S$ = crusher set $[m]$
$\rho_B$ = bulk density of material $[tonnes/m^3]$

Choke feeding is assumed in this formula. This equation also assumes that the product is distributed over the entire surface. In other words, the product is distributed in a strip over the entire length of the roll and the entire width of the set as a solid. Because the product is theoretically not evenly and completely distributed over the entire surface, the so-called ribbon factor is used. The ribbon factor gives the ratio between the theoretical maximum solid amount of material passing through the crusher according to the formula and the actual amount of material flowing through [34]. The ribbon factor has a major influence on the actual capacity and can amount as little as 25 % of the theoretical capacity. The following equation is used to describe the ribbon factor:

$$R_F = 0.0095 * \frac{Q_F}{v_p * L_S * W_R} \tag{53}$$

$R_F$ = ribbon factor $[-]$
$Q_F$ = feed rate $[tonnes/hour]$
$v_P$ = speed at circumference of roll $[m/s]$
$L_S$ = crusher set $[m]$
$W_R$ = roll width $[m]$

A modified equation to calculate the capacity of a roll crusher based on equation 52 has been defined by Otte [35]. This equation uses an efficiency factor ($\varepsilon$) that is dependent of the gap size and the desired product size. The value of the efficiency factor is usually between 0.15 and 0.30. The efficiency factor is multiplied by the bulk density to determine the density of the product, also known as operational density. The following equation has been defined by Otte:

$$Q = 3600 * \varepsilon * W_R * v_P * \rho_B * L_S \tag{54}$$

$\varepsilon$ = efficiency factor $[-]$
$\rho_B$ = bulk density of material $[tonnes/m^3]$
$\varepsilon * \rho_B$ = operational density $[tonnes/m^3]$

## 3.4 High Pressure Grinding Rolls

During the conventional roll crushing procedure, crushing mainly takes place due to the impact of particles getting caught between two rolls that force the particles to break by means of compression at the surface. This compressive force can be passed on between particles on an interparticle level and can cause breakage through friction. When the compressive force is increased to a considerable level, as is happening inside HPGR's, even more friction between particles will occur, so that breakage not only takes place at the surfaces of the roll crusher, but also in the middle of the gap between the rolls. Schönert [30], [36] has conducted research into the specific energy required for breakage to occur for various loading mechanisms. It emerged from this research that, in order to achieve the same particle size distribution, more energy is required for an impact loading mechanism compared to a compression loading mechanism. The same research also showed that an increasing particle size causes a decrease in energy consumption.

Based on this research, it can be explained why HPGR's gained popularity. Since the rolls operate under high pressure, the impact and compression loading mechanisms at the surface of the rolls will be supplemented with the more efficient friction compression loading mechanism between particles. During feeding of the material, it can be observed that the loading mechanism is similar to that of conventional roll crushers using a single driven roll. The material enters and initial fractures are caused due to high impact. Subsequently, the material larger than the gap size is crushed by means of compression. Since the compression forces are high, empty spaces between large particles are filled by smaller particles. As the empty spaces are now occupied by smaller particles, the compressive load caused by the rolls is passed on and friction between the particles takes place. This friction ensures that breakage also takes place on an interparticle level. As a result, the amount of energy per kilogram of produced material can be reduced. Another major advantage of HPGR's is the fact that HPGR's are able to produce fine products. This allows HPGR's to be used for various purposes. Being able to crush and grind, HPGR's can be placed after the first pre-crushing step for grinding purposes, but can also serve as a replacement for cone crushers.

Unlike conventional roll crushers that use springs for compression, HPGR's use a roll driven by four hydraulical cylinders. Due to the high friction forces, rolls are studded or provided with liners. Depending on the hardness of the material being processed, a consideration can be made as to how the surface is designed and which hardness of material is used for the rolls. Rolls with a higher surface hardness are better in processing hard material, but also wear out faster. Rolls with a lower surface hardness are less resistant to processing hard material, but last longer due to a lower brittleness. Typical dimensions of HPGR's are roll diameters ranging from 700 $[mm]$ to 2800 $[mm]$ and face lengths ranging from 140 $[mm]$ to 1680 $[mm]$ [35]. HPGR's are capable of reaching a crushing trhroughput of more than 750 $[tonnes/hour]$.

The most important design parameters to determine the operation of HPGR's are the roll dimensions, the nip angle, the gap size, the speed of the rolls and the roll pressure. Furthermore, material parameters such as the ore size and ore texture are meaningful. The following paragraphs will describe how each parameter can be estimated and calculated.

### HPGR operating pressure

Beisner [37] stated that the operating pressure of HPGR's must be higher than 50 $[MPa]$. Other researchers [38] defined the minimum required compressive force should be in the order of 100 $[kN/m]$. In general, the applied pressure is in the order of 200 $[MPa]$. However, higher pressures are also possible when working with harder materials. Schönert [31] described the operating pressure using the following formula:

$$p_O = \frac{F_G}{L_R * D_R} \tag{55}$$

$p_O$ = operating pressure $[kN/m^2]$
$F_G$ = grinding force $[kN]$
$L_R$ = roll face length $[m]$
$D_R$ = roll diameter $[m]$

Equation 55 refers to the mean pressure distribution. However, the operating pressure is never the same throughout the gap and depends on the nip angle between particles. The greater the nip angle, the lower the maximum pressure. The diameter and length of the rolls also influence the maximum pressure. The larger these dimensions, the better the pressure can be distributed, and thus the lower the maximum pressure will be. This relationship can be expressed with the following formula:

$$p_{MAX} = \frac{F_G}{K * D_R * L_R * \theta_{IP}} \tag{56}$$

$p_{MAX}$ = maximum pressure $[MPa]$
$K^*$ = material constant (ranging from 0.18 to 0.23) $[-]$
$\theta_{IP}$ = inter-particle breakage nip angle $[-]$

Because the material constant is difficult to determine in practice, various researchers [39] came up with another formula which does not use the aforementioned material constant. This equation is however not considering the maximum pressure and only gives an estimation for the average pressure that particles exert on each other:

$$p_{AVE} = \frac{F_G}{500 * L_R * D_R * \theta_{IP}} \tag{57}$$

$p_{AVE}$ = average mutual particle pressure $[MPa]$

### HPGR nip angle

During the comminution process in roll crushers, a distinction can be made between two phases. First, the material is nipped by the top of the rollers. This area is also called the breakage zone. Here, breakage of particles larger than the gap takes place. Because the breakage taking place here is between the geometry of the crusher and a single particle, this phenomenon is called single particle breakage. When the material enters the gap of the machine, crushing takes place by means of compression. Both the force of the crusher on the particles and the force of particles on each other cause crushing. This can be referred to as inter-particle breakage. Similar formulas can be used to define both forms of breakage. For single particle breakage the following equation has been derived [39]:

$$\theta_{SP} = cos^{-1}(1 - (\frac{D_{MAX,F}}{L_G} - 1) * \frac{L_G}{1000 * D_R}) \tag{58}$$

$\theta_{SP}$= single-particle breakage nip angle $[-]$
$D_{MAX,F}$ = maximum feed size $[mm]$
$L_G$ = gap size $[mm]$
$D_R$ = roll diameter $[m]$

For inter-particle breakage the following equation applies:

$$\theta_{IP} = cos^{-1}(1 - (\frac{\rho_C}{\rho_{B(F)}} - 1) * \frac{L_G}{1000 * D_R}) \tag{59}$$

$\theta_{IP}$= inter-particle breakage nip angle [-]
$\rho_C$ = material density inside gap $[tonnes/m^3]$
$\rho_{B(F)}$ = feed bulk density $[tonnes/m^3]$

**HPGR roll gap**

In order to determine the particle size distribution of the product and the corresponding largest particle size in the product stream, the size of the roll gap must be determined. The size of this gap depends on the roll speed, the roll geometry, the compression force of the roll and material parameters (e.g. moisture content) and material sizes. Different researchers [40] have defined the following equation which can be used to determine the size of the working gap:

$$L_G = (k_1 * v_p^2 * \frac{2}{g * D_R} + k_2 * v_p * \sqrt{\frac{2}{g * D_R}} + k_3) * (1 + k_4 * log(F_S)) * D_R \tag{60}$$

$L_G$ = gap size $[m]$
$v_p$ = speed at circumference of roll $[m/s]$
$g$ = gravity constant $[m/s^2]$
$D_R$ = roll diameter $[m]$
$F_S$ = specific grinding force $[N/mm^2]$
$k_x^*$ = material constant $[-]$

**Roll speed**

The roll speed is of great importance in order to guarantee the crusher throughput. A low rotational speed allows for more control, but causes a lack of production. A speed that is too high causes particles to be deflected from the crushing zone, which is dangerous and also reduces the capacity. Depending on the operational parameters, a suitable operation speed can be chosen. However, it is important that the maximum speed is not exceeded. Klymowsky [39] defined the maximum speed of the roll to be dependent on the roll diameter and defined it as follows:

$$Roll\ crusher\ maximum\ speed = \begin{cases} v_P \leq 1.35 * \sqrt{D_R}, & \text{if } D_R < 2 \text{ [m]} \\ v_P \leq D_R, & \text{if } D_R > 2 \text{ [m]} \end{cases} \tag{61}$$

**HPGR feed and product size**

In general, the gap size should be of the same order of magnitude as the feed. As a result, no blockages will occur due to material particles being too large. Also, a material stream consisting of particles being much smaller than the gap is undesired, since particles will flow through the crusher without being crushed. The allowable ratio between feed and crusher gap depends on the roll surface characteristics. When a smooth surface is used, the maximum supply particle size may be up to 3 times as large as the working gap. In case studded rolls are used, the size of the supply must not exceed the working gap. Based on the results of experiments, it has been found that at constant grinding forces, the speed of the rolls has little effect on the breakage rates. Furthermore, it has been found that a corrugated (channelled) roll surface has a greater effect on the grinding performance and thus provides a greater throughput compared to a regular smooth roll surface.

### HPGR capacity

The capacity of an HPGR depends on the dimensions of the gap, the speed at which the material moves through the gap and the density of the material. The capacity can therefore be expressed with the following formula:

$$Q = 3.6 * L_G * L_R * v_P * \rho_S \tag{62}$$

$Q$ = crusher capacity $[tonnes/hour]$
$L_G$ = gap size $[mm]$
$L_R$ = roll length $[m]$
$v_P$ = speed at circumference of roll $[m/s]$
$\rho_S$ = material density $[kg/m^3]$

### Knobloch and Morrell's capacity model

Another way to describe the capacity is by using the specific throughput rate as has been done by Seebach and Knobloch [41] and by Morrell [21]. Here the specific throughput rate is proportional to the $L_G/D_R$ (gap width divided by roll diameter) ratio. The advantage of this description is the fact that the varying working gap is not directly included in the calculation:

$$Q = Q_S * D_R * L_G * v_P * \rho_S \tag{63}$$

$Q_S$ = specific throughput $[tonnes/hour]$
$D_R$ = roll diameter $[m]$

### Otte's capacity model

The capacity of HPGR's can also be determined by using the gap size and the operational density of the material as has been done by Otte [35]. As mentioned earlier, the operational density is the bulk density of the material after crushing. The following formula is used to express the capacity in terms of the operational density:

$$Q = L_R * L_G * v_P * \rho_{OP} \tag{64}$$

$Q$ = crusher capacity $[tonnes/hour]$
$\rho_{OP}$ = operational density $[tonnes/m^3]$

### Morrell's capacity model

Morrell came up with a model to calculate the specific roll crusher capacity by using the specific grinding force. The specific grinding force is equal to the total grinding force determined by the area of the roll that is actively crushing ($W * D_R$). The equations make use of a constant depending on the roll speed that has been determined experimentally and a constant depending on the material being crushed. The following equations are used to calculate the constant $k$ and the specific throughput:

$$Q_S = k * (1 + C * log(\frac{F_G}{1000 * L_G * D_R})) \tag{65}$$

$Q_s$ = crusher specific throughput $[tonnes/hour]$
$k*$ = constant depending on roll speed $[-]$
$C*$ = material constant $[-]$
$F_G$ = grinding force $[kN]$

$$k = C_1 * v_P^2 + C_2 * v_P + C_3 \tag{66}$$

$C^*_{1,2,3}$ = material constants $[-]$

### HPGR power consumption

As mentioned in previous paragraphs, the required power is a multiplication of the capacity and the amount of energy required per amount of material. Bond's work index appeared in previous sections (jaw crusher, gyratory and cone crusher) to give a good reflection of this energy requirement. However, several studies [42] have shown that Bond's work index is less applicable to roll crushers.

There are three physical laws that describe the energy required for size reduction: Bond's law, Rittinger's law and Kick's law. All laws are based on different assumptions. Bond's law assumes that the work required to reduce the particle size from a large feed is proportional to the square root of the surface to volume ratio. Bond's law can be defined by the following equation:

$$P = k * (\sqrt{\frac{1}{X_0}} - \sqrt{\frac{1}{X_1}}) \tag{67}$$

$P$ = power $[kW]$
$k*$ = constant dependent on surface tension, crushing efficiency (ratio of increase in surface energy to total energy administered to the material) and mechanical efficiency (ratio of energy transferred to material to total energy consumption)
$X_0$ = average particle outer diameter before crushing $[m]$
$X_1$ = average particle outer diameter after crushing $[m]$

Rittlinger's law states that the energy required for a reduction in particle size of a material is directly proportional to the increase in surface area [43]. Rittlinger's law can be defined by the following equation [44]:

$$P = k * (\frac{1}{X_1} - \frac{1}{X_0}) \tag{68}$$

Here the parameter k also depends on the surface tension and both efficiencies mentioned in equation 67.

Lastly, Kick's law states that the amount of energy required to reduce the size of a material by a certain proportion is constant [43]. Kick's law can be defined by the following equation:

$$P = k * log(\frac{X_0}{X_1}) \tag{69}$$

It can be noticed that all three laws are based on two general principles:

- The energy required for size reduction is proportional to the differential decrease in size ($d\tilde{E} \propto -d * D$).
- The energy required for size reduction is inversely proportional to the size to some power ($d\tilde{E} \propto \frac{1}{D^n}$).

This can be written to the general formulation:

$$\frac{\tilde{E}}{d * D} = -\frac{C}{D^n} \tag{70}$$

The only difference between the previously mentioned equations is that the power $n$ varies. Bond's law has been appropriate to model the power consumption of comminution equipment mentioned in earlier paragraphs. However, in the case of HPGR's, Rittinger's law appears to give a more accurate estimation of power consumption.

The power required to allow rotation of the roll depends on the amount of torque needed, the required angular velocity and the diameter of the roll. The following equation can be used to determine the required power and is based on fundamental physics [40]:

$$P = \frac{2 * T * \omega}{D_R} \tag{71}$$

$P$ = power $[kW]$
$T$ = torque $[Nm]$
$\omega$ = angular velocity $[rad/s]$

The torque is the cross product of the distance vector and the force vector. The distance vector is the distance from the core of the roll to the point of application of the force (i.e. the diameter of the roll). The force vector can be denoted as a product of the horizontal force exerted on the roll by the material and the angular displacement caused by it. This will lead to the following formula:

$$T = \psi * F_{G,H} * D_R \tag{72}$$

$\psi$ = angular displacement [-]
$F_{G,H}$ = horizontal component grinding force [N]

The angular displacement depends on the speed at the circumference of the roll and the specific grinding force. Morrell [40] has conducted experiments and found the following relation to determine the angular displacement:

$$\psi = (a * v_P^2 + b * v_P + c) * (1 + k * F_S) \tag{73}$$

Combining equation 71, 72 and 73, the following equation to determine the power consumption of an HPGR:

$$P = 2 * \omega * F_{G,H} * (a * v_P^2 + b * v_P + c) * (1 + k * F_S) \tag{74}$$

### Concluding remarks

This chapter described the influence of various operational parameters on the overall crusher performance. Mutual relationships have been examined for three types of crushers (jaw, gyratory/cone and roll) that use the compression load mechanism. Different studies have been compared to define functions to determine the values of three important crusher characteristics. This concerns the critical operation speed, the capacity and the power consumption. A distinction has been made between general rules of thumb for the design of crushers based on substantiated scientific models. These models range from considerably extensive parameter and dimension considerations to somewhat cumbersome empirical relations. Therefore, the results are not always aligned. In general, Rose and English's models take into account the most variables and therefore have the highest accuracy. However, there is a common thread among all studies. All models assume that the capacity is based on the geometry of the crusher and its critical speed. By multiplying the capacity by the reduction ratio and the work index, the power consumption can be calculated. To further increase the accuracy, some studies also take into account the material properties of the processed material. A number of important relationships emerged from the studies mentioned earlier, which will be used in the following chapters. The most important results can be summarised as:

- The required throw increases when the gape size increases.
- The required critical speed decreases as the throw increases.
- The required critical speed decreases when the gap size increases.
- The required critcal speed increases when the inclination angle of a cone inside a cone or gyratory crusher increases.
- The capacity decreases when the nip angle increases.
- The capacity increases when the set size increases.
- The capacity increases when the pressure in a roll crusher increases.
- The required power consumption increases when a higher degree of reduction is required.

The information gained in this chapter provides guidance to set up the simulation and calibration experiments in the following chapters. Since the most important design parameters and their relationship to the critical speed, the capacity and the power consumption are now known, it can be checked whether the results of the simulations using the novel model agree with the research that has been proven to be true.

# 4 Contribution of particle breakage models to simulating comminution interactions

The discrete element method is a numerical method to compute and simulate the motion and mutual interaction between a large number of small particles. The use of DEM simulation software such as Rocky DEM and Altair EDEM can be used in a variety of situations and has proven its veracity over the years. The applicability of DEM software is also increasing. A good example is a new field in which DEM simulation software can be used: simulating particle breakage behavior. When simulating bulk material handling and size reduction procedures, breakage representation in the discrete element method (DEM) is critical to accurately capture particle fragmentation and degradation.

The founder of the breakage model used as an API in both Rocky DEM and Altiar EDEM is Professor Luis Marcelo Marques Tavares. The basis for the model was formed during his PhD research. Over the years, together with a team from the Federal University of Rio de Janeiro, more research has been done and a working model has been developed. The model is able to capture the fracture behavior and stress accumulation of brittle materials. The model uses the Laguerre-Voronoi tessellation algorithm (also known as power diagram or sectional Dirichlet tesselation) to simulate breaking behavior as realistically as possible. By combining probabilistic relations and material properties, the breaking behavior based on energy dissipation during breakage events can be calculated. This preserves both mass and volume.

First, the material breakage parameters of the relevant material are defined. An important value is the particle specific fracture energy ($E_T$). The particle specific fracture energy is defined as the amount of energy necessary to create one unit area of a crack. The particle specific fracture energy is an upper-truncated continuous log-normal probability distribution of a random variable whose logarithm is normally distributed. The median of the fracture energy is dependent on the particle size distribution. In general, the smaller the particles, the higher the required specific fracture energy. Tavares [45] defined the following relationship between the particle size distribution and the median fracture energy:

$$E_{50} = E_{\infty} * (1 + (\frac{d_0}{d_j})^{\phi}) \tag{75}$$

$E_{50}$ = median of mass-specific fracture energy $[J/kg]$
$E_{\infty}$ = model parameter of fracture energy distribution model $[J/kg]$
$d_0$ = model parameter $[mm]$
$d_j$ = representative particle of size class $j$ $[mm]$
$\phi$ = model parameter $[-]$

The cumulative distribution is based on the fact that a particle of a specific size will break after being charged with different contact specific energies ($E_{CS}$). In other words, the cumulative distribution will give the probability that a particle from a sample will fracture when subject to an impact of energy $E^*$. Tavares [45] defined the cumulative form of the breakage probability distribution which can be written as:

$$P_0(E_{CS}) = \frac{1}{2} * (1 + erf(\frac{ln(E^*) - ln(E_{50})}{\sqrt{2 * \sigma}}) \tag{76}$$

$P_0$ = cumulative distribution $[-]$
$E^*$ = mass-specific particle fracture energy $[J/kg]$
$\sigma$ = standard deviation of mass-specific particle fracture energy $[J/kg]$

The ratio between the specific impact energy and the specific particle fracture energy can be defined as:

$$E^* = \frac{E_{MAX} * E_T}{E_{MAX} - E_T} \tag{77}$$

$E_{MAX}$ = upper truncation value of log-normal distribution (= 4 * $E_{50}$) $[J/kg]$
$E_T$ = particle specific fracture energy $[J/kg]$

When a particle is in contact with other particles or with the crusher geometry, stresses will arise. These contact specific energies ($E_{CS}$) may or may not exceed the energy required for breakage. When the stresses are not high enough to cause breakage, damage can still be made to the material. This damage will accumulate and make breakage easier in the future, making particles more amenable to fracture after previous contacts. Tavares [46] used to following equation to define the sustained damage to a particle after undergoing a stress which did not lead to breakage:

$$D = (\frac{2 * \gamma}{2 * \gamma - 5 * D + 5} * \frac{E_{CS}}{E_T})^{\frac{2 * \gamma}{5}} \tag{78}$$

$D$ = damage (values between 0 to 1) $[-]$
$\gamma$ = damage accumulation coefficient $[-]$
$E_{CS}$ = contact specific energy $[J/kg]$

An increase in the damage factor leads to a decrease in the particle specific fracture energy. The following equation indicates the relationship between the specific fracture energy before and after damage:

$$E_{NEW} = E_{OLD} * (1 - D) \tag{79}$$

$E_{NEW}$ = mass-specific fracture energy after damage $[J/kg]$
$E_{OLD}$ = mass-specific fracture energy before damage $[J/kg]$

When the contact specific energy has a value higher than the specific fracture energy of a particle, breakage will occur. The fragments that will arise from the breaking process will, as mentioned earlier, be based on the Laguerre-Voronoi algorithm.

The Laguerre-voronoi algorithm is based on a partition of the Euclidean plane into polygonal cells defined from a set of circles. The sides of these cells are formed by a line caused by the tangent of the point were the two circles make contact. When the tangent lines of multiple contact points are extended, cells will be created. The boundaries of these cells are characterized by the fact that the distance between the centers of two circles forming the tangent is the same everywhere on the line. At the point where three lines intersect, the distance between the intersection point and the centers of the three adjacent circles is equal.

Figure 17 shows this phenomenon. Three particles are sketched in the figure. The geometrical center of all particles is indicated by a red dot. When three circles of equal radius are drawn from the three centers, they will eventually make contact. The tangents at the contact points are indicated as black lines. The distance between a point on the tangent and the geometrical centers of the two particles is the same throughout the line. At the point where the three tangents intersect, the distance between the intersection and the geometric centers of all particles is equal.

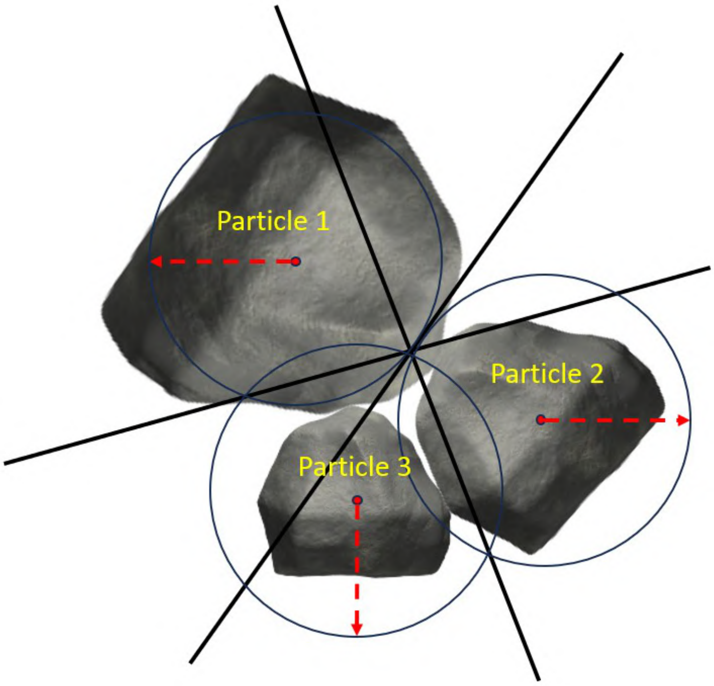

Figure 17: Laguerre-Voronoi

An important value to conduct the simulation is the $t_{10}$ parameter. Tavares [3] defined the $t_{10}$ variable as the fraction of the progeny that is smaller than $1/10th$ of the parent particle. The $t_{10}$ value is taken from the approximately linear portion of the progeny size distribution. Each progeny size distribution has a unique value of $t_{10}$ and all $t_n$ values are related to that individual distribution. The relationship between the input (or comminution) energy and the $t_{10}$ parameter has been described by:

$$t_{10} = A * (1 - e^{-b*E_{CS}}) \tag{80}$$

$t_{10}$ = proportion of material passing a screen with aperture of $1/10th$ of the parent particle size $[-]$
$A$ = model parameter $[-]$
$b$ = model parameter $[-]$
$E_{CS}$ = specific comminution energy $[J/kg]$ or $[kWh/tonne]$

The full particle size distribution can be described through the following function that takes into account the $t_{10}$ value which has been calculated in equation 80. The following equation assumes that a particle is a fraction $n$ smaller than the parent particle after breakage:

$$t_n(t_{10}) = \frac{100}{\int_0^1 x^{\alpha_n - 1} * (1-x)^{\beta_n - 1}\, dx} * \int_0^{t_{10}/100} x^{\alpha_n - 1} * (1-x)^{\beta_n - 1}\, dx \tag{81}$$

Lastly, two other parameters are important to conduct the simulation using Tavares' breakage model. First of all, this concerns the minimum specific energy ($E_{min}$). The minimum specific energy is the minimum energy required for particle damage (not breakage) to take place. This also implies that when an energy smaller than $E_{min}$ is exerted on a particle, no contact information is registered by the model. The second important parameter concerns the minimum particle size. This parameter determines the smallest size particles can have after breakage. In other words, this is the smallest value of the progeny particle size distribution.

### Concluding remarks

Concluding this chapter, it is evident that the equations outlined herein provide a fundamental framework for understanding Tavares' breakage model and its relevance in elucidating comminution processes. Through the elucidation of breakage rate equations, selection and breakage functions, population balance equations, and considerations of particle strength and energy consumption, valuable insights into the dynamics of particle breakage emerge. However, it is important to understand that while these equations offer a theoretical foundation, their practical applicability hinges upon their validation and calibration against empirical data. Furthermore, the adaptable nature of these models necessitates continual refinement to suit the complexities of diverse materials and operational settings. Notably, these equations find practical utility in simulation software such as EDEM, where they facilitate the modeling of breakage interactions within granular systems.

# 5 Implementation of particle breakage models in granulator interactions

## 5.1 Discrete Element Method (DEM)

The discrete element method (DEM), also known as the distinct element method, is a group of numerical methods that are able to compute the motions and forces arising from interactions between a large number of particles within a geometry. The discrete element method was originally developed by Cundall and Strack [47] to model granular assemblies. Over the years, the use of DEM has emerged in an increasing amount of studies and simulation software has been developed in which the behavior of a large group of particles can be modeled. Both open-source and commercial DEM software programs are widely available. It has been proven that the use of DEM can be effective, but one should pay close attention to its limitations and pitfalls. First of all, a description will be given of the functioning of the DEM algorithm and factors that can influence the functioning of the simulation will be mentioned. Then a description will be given how a breakage interaction can be implemented in DEM software.

### 5.1.1 DEM algorithm

First, the user needs to define the concerned particles and their properties. This includes the particle shape, the dimensions of the particle and its particle size distribution. Then, material dependent properties such as the Poisson ratio, the solid density, the Young's modulus and the shear modulus will be defined. Also, properties that are important for mutual interactions between particles and geometry (e.g. coefficient of restitution, coefficient of static friction and coefficient of rolling friction) will be defined. Based on this data, the software itself is able to calculate the mass, the volume and the moments of inertia around the X-, Y- and Z-axis.

A geometry in which the interactions take place must also be defined. This geometry will indicate the boundaries of the area where the collisions can take place. The geometry can be imported as a CAD model from various software programs. Based on the desired orientation, the different parts of the geometry can undergo translation or rotation to make the assembly fit together correctly. A movement (rotation or translation) can also be assigned for dynamic parts. Additionally, the geometry needs to be given the correct properties and particle interaction parameters.

Because the DEM software has to perform a considerable amount of calculations and therefore requires a lot of CPU and/or GPU capacity, the simulation time will be decreased when the geometry is simplified as much as possible. Figure 18a shows the original manufacturer design of the cutting chamber of the Moditec Goliath Plus 3. The image clearly shows that there are many details in the design, which will have little influence on the granulating performance and thus on the outcome of the simulation. To make the simulation time as short as possible, figure 18b shows the simplification of the smaller Goliath Plus 2 version present at GreenCycl B.V. in which only the most essential parts are included. This model has been made using SolidWorks. Because the manufacturer was not willing to share working drawings of the true dimensions, is has been chosen to determine the dimensions by own measurements.

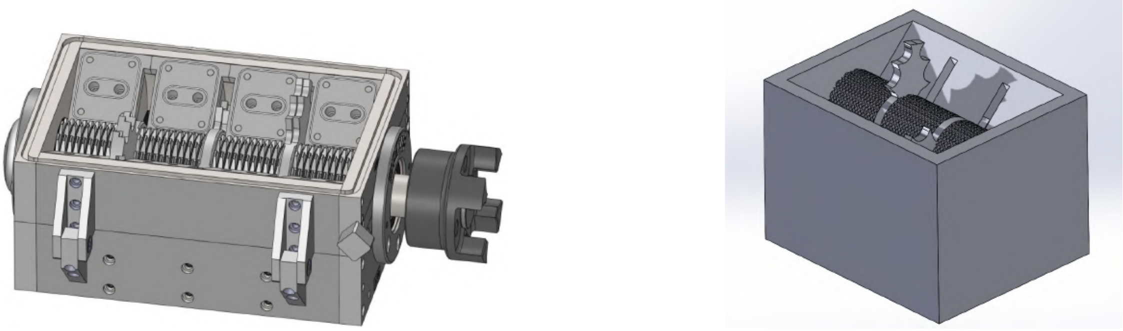

(a) Goliath Plus 3 manufacturer CAD model

(b) Goliath Plus 2 simplified SW model

Figure 18: Detailed model provided by manufacturer (18a) and simplification made using SolidWorks (18b)

Apart from the solid boundary geometry, a volume must also be created in which the particle generation can take place. This volume is called a factory in jargon. The factory can, just like the aforementioned geometries, be imported as a CAD model, or can be created using DEM software. Since the factory is a virtual geometry instead of a physical geometry, it will have a mass of 0 $[kg]$ and a moment of inertia of 0 $[kg * m^2]$ around all axes. The user can define where, how and when the particles should be generated. For example, a generation rate can be chosen based on a total number of particles or based on a total desired mass. Also, the position, the initial speed and the orientation can be set as desired.

When the user has specific requirements for particle generation, a plug-in factory can be used. The plug-in factory can be loaded as a file into DEM software and can be used to account for specific particle generation when the standard functions of DEM software are not sufficient. An example of a plug-in factory is the breakage model of Professor Luis Marcelo Tavares. Here a particle replacement takes place based on the material properties and the impact forces between particles themselves and between particles and the defined geometry. This particle replacement is initiated by the defined plug-in factory.

### 5.1.2 Chosen contact models

After defining the particles, the geometry and the factory, a suitable contact model needs to be be chosen. Different contact models can be chosen for all three types of interactions (particle to particle, particle to geometry and particle body force). A contact model describes how elements react when they come into contact with each other. Contact models consist of a base model and a friction model. The base model defines the physical collision between particles and the geometry. Base models mostly consist of spring forces and damping forces in both the normal and tangential direction of the particles. The rolling friction model accounts for the resistance of particles against rolling. One can also chose to use additional models provided by DEM software, or plug-in models such as the breakage model of Professor Luis Marcelo Tavares. To ascertain which contact model is optimal, an initial assessment will be conducted on existing models and their respective advantages and disadvantages. More information about the existing contact models can be found in Appendix B.

By means of thorough study of all models, a well-considered choice can be made regarding which model is best suited for this particular situation. This comprehensive understanding of the strengths and limitations of each model ensures that the selected combination, namely the Hertz-Mindlin (no slip) model with standard rolling friction and the Tavares URFJ Breakage model, is tailored to the specific requirements of the research on particle breakage simulation in EDEM. This approach enhances the robustness and reliability for the following reasons:

- Physical Accuracy: the Hertz-Mindlin model is one of the most commonly used contact models in the Discrete Element Method (DEM). It is based on the classical Hertz theory of contact mechanics, which calculates the contact forces between particles based on their geometry and material properties. Incorporating the no-slip aspect of this model accounts for the degree of friction between particles, which is crucial for realistic simulations of particle movements.

- Rolling Friction: the addition of standard rolling friction in the Hertz-Mindlin model is crucial for systems where particles roll alongside sliding. This rolling friction property helps simulate realistic particle behaviors, especially in situations where rolling plays a significant role, such as in granular materials.

- Tavares URFJ Breakage Model: the Tavares URFJ Breakage model is specifically developed to model particle breakage in granular materials. This model takes into account various factors influencing particle breakage, such as material properties, loads, and particle size. By integrating this model, one can accurately track the fracture behavior of particles in simulations, which is essential for a deep understanding of material deformation and fragmentation.

- Validation and Applicability: both models are well-validated and widely used in the literature for similar studies. Using established models enhances the credibility and reproducibility, making it easier to compare and verify results with previous studies.

By combining the Hertz-Mindlin (no slip) model with standard rolling friction with the Tavares URFJ Breakage model, one can achieve an accurate and realistic simulation of particle breakage, which is crucial for understanding complex phenomena in granular materials. This combination provides a solid foundation and is likely to yield valuable insights into the dynamics of particles in such systems.

## 5.2 Simulation settings

After completing the design of the environment in the creator tree, the simulation settings can be set. One of the most important parameters to determine is the correct time step.

The time step of a simulation is the amount of time between iterations (also known as calculation steps). DEM simulations require a large number of elements and various equations to be solved for every single time step. Therefore, the overall computation time is largely dependent on the chosen time step. The time step needs to be chosen carefully, since it affects the accuracy and reliability of the simulation. When the time step is chosen to be large, the overall computation time will decrease. On the other hand, this will also affect the accuracy of the simulation. The reason is that some contacts might not be captured, which leads to particles falling through the geometry and not be able to interact with each other. However, when the time step is chosen to be short, the computation time will increase. This is accompanied by better accuracy, allowing contacts to be captured more precise.

To help determine the correct time step, the critical time step is used. The critical time step is also referred to as the smallest time step which ensures that the speed of propagating waves within an element is less than what it can theoretically transmit. The critical time step can be determined by means of two approaches. The first approach uses the oscillation period of a single degree of freedom system. The second approach uses the Rayleigh wave speed. This is the time it takes for a shear wave to propagate through a solid particle. The Rayleigh time step ensures that the time step size is small enough to capture wave propagation accurately and prevent numerical instability (a rapid divergence of the calculated solution from the true solution). When using a simulation with a range of particle sizes, the Rayleigh time step is calculated based on the smallest particle size. This means that during a single time step, disturbances cannot propagate further than the immediate neighbors. The Rayleigh time step is computed based on the smallest particle size when running a simulation with a variety of particle sizes. As a result, disturbances cannot spread past their close neighbors during a single time step.

When starting a simulation, a suitable time step needs to be chosen. A suitable time step is often selected as a fraction of the Rayleigh time step value. A range varying between 10 % – 40 % of the Rayleigh time step is generally chosen. The choice depends highly on the amount of particle energy. The larger the particle forces, the more intense the collisions will be and therefore the lower the necessary required time step. The default advised value is 20 % of the Rayleigh time step. This ensures an accurate simulation without making the simulation time too lengthy.

When the collision force is high enough to break a particle, the particle will turn into fragments smaller than its original size. This causes the preset Rayleigh time step based on the dimensions of the smallest particle at t=0 to no longer be accurate.

To prevent this effect, DEM software offers the option to choose an auto time step. Choosing an auto time step ensures that the software takes the smallest particle size into account for every single time step. The Rayleigh time step will be adjusted based on the smallest dimensions of the particles in the previous time step. This will ensure that the simulation remains as accurate as possible for time steps above t=0.

DEM software also allows to chose a time integration technique. This technique calculates the unknown values in the current time step based on the known values from the previous time step. There are two types of time integration techniques that can be used based on the problem and the requirements of the end user: an implicit and an explicit method.

The explicit method calculates the status of a system at a future time based on the status of a system that is currently known. The implicit method calculates the status of a system at a future time based on the status of a system at present and future times.

The Euler method, also known as the forward Euler method, is a first-order numerical approach for resolving ordinary differential equations (ODE's) with a specified initial value. The Euler method is the most straightforward explicit approach for integrating ordinary differential equations in a numerical way. The Euler method calculates the position in the next time step by using the current position and adds the current velocity. The velocity is calculated by adding the current velocity and the acceleration. First-order means that only the first derivative of the given function appears in the equation, and higher derivatives are absent. The Position Verlet and the Velocity Verlet are both integration methods from the second order. Second order means that the second derivative of the given function appears in the equation. Using a second order integration method adds an extra computational time of approximately 10 %.

The order of an ordinary differential equation can be extended until infinity, however increases computation time significantly. Higher order integration methods are currently not supported in DEM software.

Since numerical methods give an approximation of the results reached by using exact methods, a truncation error will be introduced. A distinction can be made between two different types of truncation errors: local truncation errors and global truncation errors. Local truncation errors are caused by the difference between the exact value and the approximate value within one time step. Global truncation errors are introduced by adding all rounding errors for every time step.

The more time steps are introduced, the lower the truncation error will be and the lower the total error will be. However, when too many time steps are introduced, the rounding error will increase. The rounding error initially looks similar to the truncation error. The rounding error can be seen as the negative aspect of including a small time step. The more time steps are introduced, the more rounding errors will accumulate into a total error. It is therefore important to choose a time step that is low enough to limit truncation errors, but at the same time high enough to not introduce excessive rounding errors.

Apart from the Euler method, DEM software also offers the possibility to perform simulations using the so-called Verlet algorithm. Verlet integration is a numerical method that is used to integrate Newton's equations of motion. Verlet integration is numerically more stable than Euler Integration. In other words, small perturbations of initial data result in small changes in the numerical solution. Furthermore, Verlet integration eliminates the need to explicitly store the particle's velocity. By using Verlet integration, one can make an estimation of a particle's future position based on the particle's previous position, negating the requirement for the velocity variable. Therefore, Verlet integration stores the particle's present position, its previous position, and its acceleration instead of directly storing and managing its velocity. In DEM software, one can choose between a Position Verlet integration and a Velocity Verlet integration. While Position Verlet integration only uses the known positions and acceleration of a particle, Velocity Verlet integration requires the initial positions and initial velocities.

After determining the desired time step and the integration method, the simulation time can be determined. Because DEM simulations require a relatively large amount of computational power, the simulation time is generally set relatively short. The calculation time usually grows approximately linearly with the simulation time. However, in the case of particle breakage simulations, the calculation time will increase as the simulation progresses. This can be explained by the fact that the total amount of particles increases due to collisions. As a result, trajectory calculations must be done for more particles per time step. It is therefore important not to increase the simulation time longer than necessary.

To save storage space, one can choose the interval after which the software should save the calculated values. It is important to remember that the data saving interval is not the same as the time step. The storage interval does not affect the overall accuracy of the simulation. By choosing a small time step and a large storage interval, contacts can still be modeled correctly, without the simulation taking up a considerable amount of space. Furthermore, DEM software also offers the opportunity to compress data and to selectively save certain information.

Eventually, in the simulator engine the user can choose whether to use only the CPU (Central Processing Unit) for the simulation or whether to opt for a coupling between CPU and GPU (Graphics Processing Unit).

Ultimately, in the simulator engine one can choose whether to use only the CPU for the simulation or whether to opt for a coupling between CPU (Central Processing Unit) and GPU (Graphics Processing Unit). A device's CPU acts as its head and tells other components what to do. The GPU (graphics processing unit) is a specialized processor that can quickly execute commands for editing and displaying images. Users can use the Graphics Processing Unit (GPU) on their PC's to execute EDEM simulations by means of the EDEM GPU solver engine. GPU's have many thousands of computational cores, in contrast to standard desktop CPU's. The Discrete Element Method (DEM) is especially well-suited for scaling over these large numbers of cores. This implies that users may now conduct larger simulations than what was previously feasible on a CPU alone, since the EDEM GPU solver can execute simulations faster.

The GPU solver uses two types of programming languages: OpenCL and CUDA:

- OpenCL is a programming language, framework and platform developed by Apple for performing complex parallel calculations on the CPU and GPU, amongst other matters. OpenCL can be used with both AMD hardware and NVIDIA hardware. The OpenCL solver is an outdated model.
- CUDA, which stands for Compute Unified Device Architecture, is a GPGPU technology that allows the programmer to use the C programming language to run algorithms on the GPU. CUDA is recommended as a solver and can be used to simulate multi-sphere, sphero-cylinder and polyhedral particles. A disadvantage of CUDA is that it can currently only be used in combination with NVIDIA hardware.

Finally, it is important that the number of cores on which the simulation will be ran is selected. A CPU's processing ability is affected by the number of cores. Therefore, the more cores a CPU has, the greater computational power it will have. DEM software offers the option to choose the amount of cores within the range of 1 to 12 cores. By linking the CPU solver to the GPU solver, the computational power can be increased. This is because GPU's contain many thousands of computational cores. This makes the DEM software particularly suited for scaling across the high number of available cores. Therefore, the EDEM GPU solver can run simulations faster. This allows users to be able to run larger simulations compared to only using CPU power.

## 5.3 Creating the geometry

As mentioned in the beginning of the report, a Moditec Goliath Plus 2 low-speed granulator, consisting of two cutting blades, has been considered. The two cutting blades are attached to a rotating axis. The axis consists of grooves and ridges. The two large cutting blades are used to initialize the first fragmentation of the largest particles present within the granulator. Figure 19a shows the top view of the granulator present at GreenCycl's facility. Figure 19b shows the side view of the Moditec Goliath Plus 2 low-speed granulator.

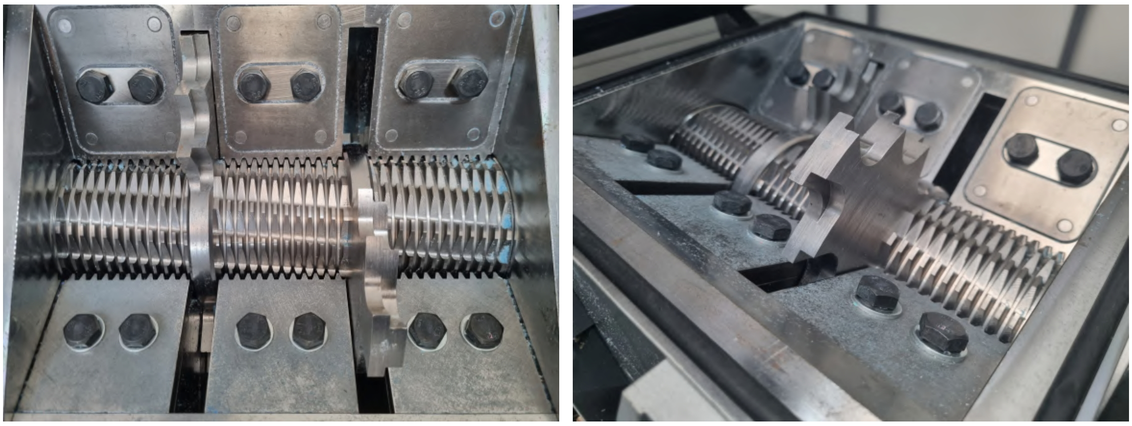

(a) Granulator top view

(b) Granulator side view

Figure 19: Examples of breakage mechanisms

The rotating shaft consists of sharp corners, in which smaller progonies can get stuck. When the trapped particles hit the solid geometry, they will also be reduced in size. When the progonies reach a size that is small enough to no longer get stuck between the rotating axis and the geometry, they will be carried along with the rotating axis and fall down by means of gravitational force.

The rotating axis can be divided into five parts connected to eachother. These consist of three shaft parts and two cutting blades. When the shaft is viewed from one side to the other, the parts are arranged in the following order: shaft, cutting blade, shaft, cutting blade, shaft. The three axle parts are equal in shape and dimensions. The two cutting blades also have the same shape and dimensions. The only difference between the two cutting blades is the fact that the one blade is rotated 90 degrees away from the other. The image below (figure 20) is a render of the rotating axis made in SolidWorks.

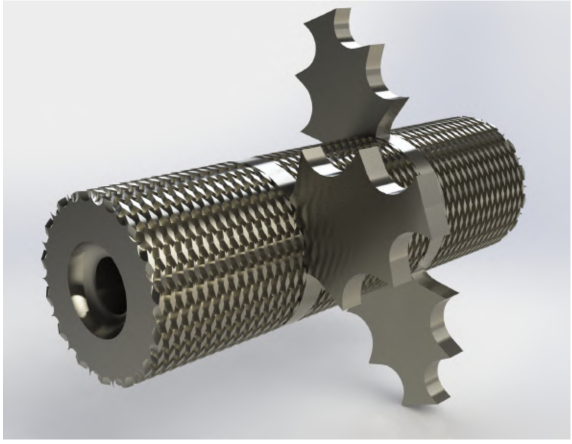

Figure 20: Rotating axis render

The rotating axis is placed inside a casing. This casing consists of two slots in a sloping side. When the material is broken and carried into the slots by the blades on the shaft, the material will move under the rotating axis and will be carried upwards by the blades. When the material is small enough, it will be carried down by the shaft and is disposed from the bottom of the machine. This allows a maximum output size to be guaranteed. A disadvantage is that material can be granulated into powder, which can be disadvantageous in subsequent process steps. The granulated material is collected in a dispenser. The image below (figure 21) is a render of the casing including the two slots that allow the blades to rotate through the geometry. The granulated material is collected in a dispenser.

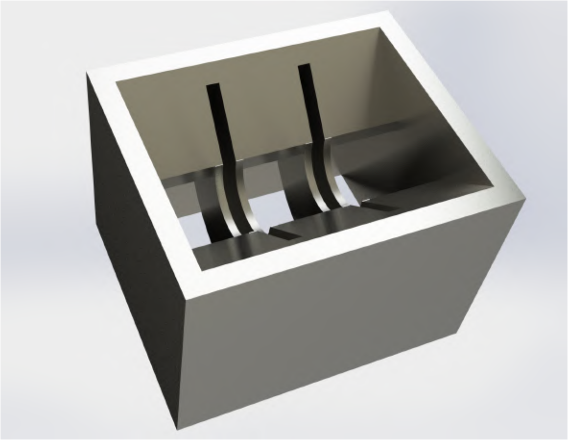

Figure 21: Casing render

When the axis is placed in the casing, an assembly can be made. This assembly is a simplification of the current Moditec Goliath Plus 2 low-speed granulator, but contains all the elements and necessary main dimensions needed to capture the foremost breakage interactions. Adding more details will greatly increase the simulation time, while the effect on the particle size distribution will be negligible. Figure 22 shows a render of the entire assembly.

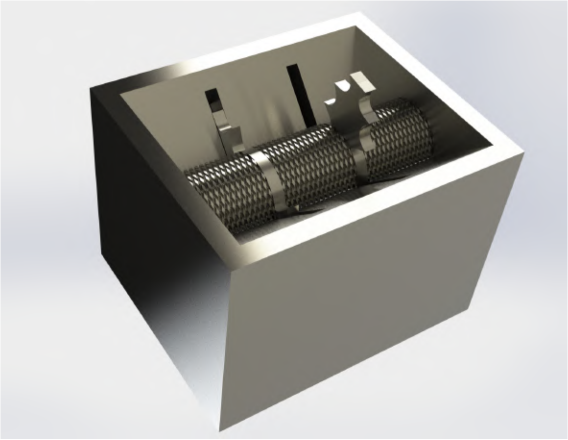

Figure 22: Casing and rotating axis render

Since the geometry is now fully defined, it can be saved. DEM software does not allow importing SolidWorks parts and/or assemblies. Therefore, the parts are stored individually as CAD geometries. The next chapter will describe how the geometry and movements are being set inside the DEM environment.

## 5.4 Importing the geometry into EDEM

After converting the SolidWorks files to CAD geometries, they can be imported one by one into EDEM. When the parts have been imported, the correct positions relative to each other must be set. A translation and/or rotation can then be set for every single part. To prevent the particles from shooting 'out' of the geometry during the breakage process, a virtual funnel has been added above the axis and casing. This will obstruct particles from leaving the simulation environment, similar to what can be seen inside the Moditec Goliath Plus 2 granulator.

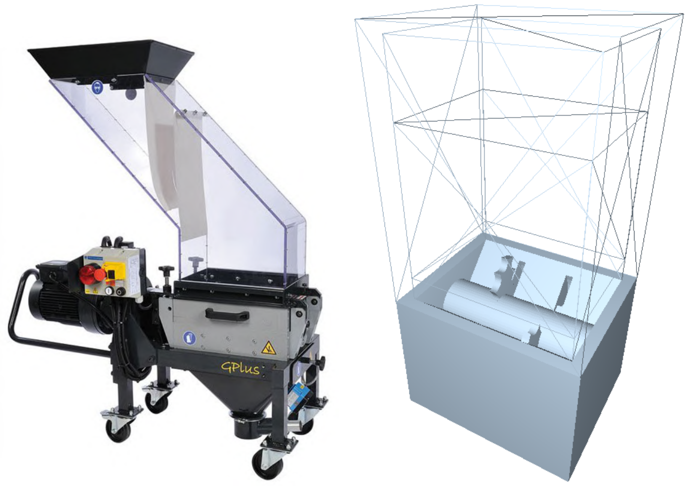

(a) Moditec Goliath Plus 2 [48]   (b) Imported CAD files in EDEM

Figure 23: Moditec Goliath Plus 2 granulator (figure 23a) and imported simplified design in EDEM (figure 23b)

As can be seen in figure 23b, the rotating axis is modeled as a cylinder without teeth. This has to do with the fact that calculating the interactions between the particles and the teeth requires a considerable amount of computing capacity, while not having a large effect on the overall breakage performance. When developing a DEM simulation, it is crucial to strike a balance between capturing the essential features of the system and maintaining a level of simplification that allows for reasonable computational efficiency. For this reason it was decided not to add any details to the rotating axis, but to leave a small space between the axis and the fixed geometry. This allows particles that are small enough to fall down and leave the simulation environment.

## 5.5 Calibration of particle breakage models

First of all, the upper limit and the lower limit of the particle size distribution must be known. The upper limit is formed by the largest particle that is introduced as feed in the simulation. The lower limit is formed by the smallest size a particle will receive after a breakage event. The smaller the final particles, the longer the simulation will take. Since DEM simulations are generally known to be time-consuming, a wise trade-off must be made between the desired resolution and the simulation time. Based on this consideration, a suitable minimum particle size can be determined.

After the upper limit and the lower limit of the particle size distribution have been determined, one can proceed with defining the correct values that influence the specific breakage behavior of a material. The input parameters for the simulation differ per material. It is therefore necessary that the model is first calibrated. Through calibration testing and curve fitting, these parameters can be estimated. The variance $\sigma^2$ and the model parameters $E_\infty$, $d_0$, $\phi$, $A(\%)$, $b'$ and $\gamma$ can be determined in this way.

There are several ways to perform model calibration. In general, single-particle breakage tests are performed to determine the breaking behavior of materials, to calculate the energy required for this and to map the effect of various parameters (e.g. particle shape and particle size) on the breaking process. Since loading takes place long enough to achieve internal equilibrium of stresses inside the particle, the described models are quasi-static. Some examples of equipment to conduct calibration with are a drop weight test (figure 24a) and a pendulum test (figure 24b). In the drop weight test a particle that is placed on top of a hard surface is struck by a falling weight. In the pendulum test a particle is hit by two moving hammers. Using classic mechanics the energy of both impacts can be calculated. Each test is specific for a restricted range in amount of deformation. Tests can be categorized by the way in which stress is applied to a particle and by the number of contact points at which fractures can occur. This concerns single impacts tests (figure 24a), double impact tests (figure 24b) and compression tests that make use of uniaxial compression presses.

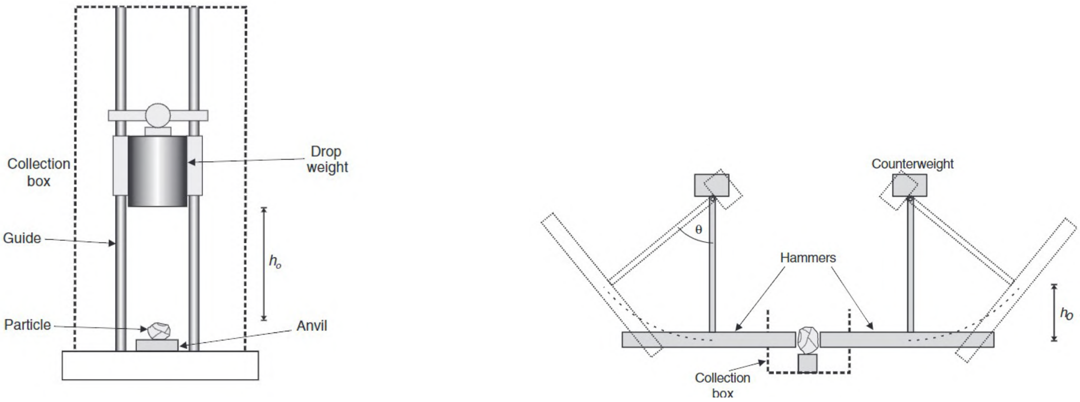

(a) Drop weight tester

(b) Pendulum tester

Figure 24: Examples of analog breakage testing equipment [3]

The deformation of the material is generally described by means of the Hertzian contact model. This model takes into account the localized stresses that arise when two curved surfaces come into contact and gradually deform as a result of applied loads. The modulus of elasticity of the material in contact will determine the amount of deformation that occurs.

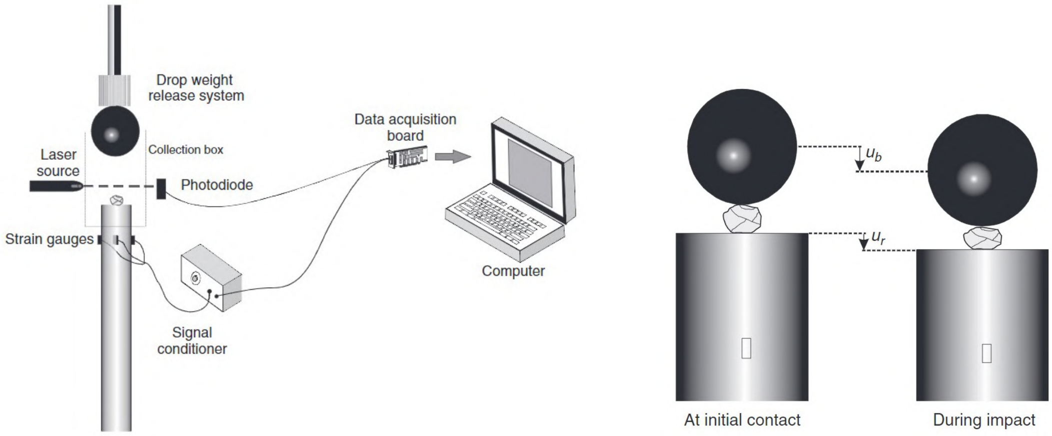

(a) Impact load cell tester set-up

(b) Impact load cell tester close up

Figure 25: Examples of digital breakage testing equipment [3]

In order to be able to trust the result of a simulation, one needs to make sure that the simulation mimics reality as accurately as possible. Calibration tests are very important to guarantee that simulation results agree with reality. In Tavares' breakage model, various working parameters have been determined by means of breakage tests and by measuring the resulting particle size distributions that can be entered into the simulation for different materials. However, the determined data concerns mostly minerals. Given the brittle nature of the polypropylene blocks used for this experiment, it is assumed that the simulation will give no issues using this material as an input.

### Concluding remarks

Calibration tests are crucial to validate simulation models by comparing simulated particle size distributions with experimental data, ensuring accuracy in predicting granulator behavior. They provide a basis for refining simulation parameters and enhancing the fidelity of predictions, crucial for optimizing granulation processes. However, due to the time-consuming nature of breakage experiments and the complexity of determining the particle size distribution, calibration by means of infield experiments has not been pursued. Instead, the focus of this study is on demonstrating the functionality of particle breakage within a dynamic geometry simulated using Tavares' breakage model in EDEM. It is important to note that there has been no previous research conducted on the effectiveness of the breakage model used for a granulator; previous research has primarily centered around crushers, as described earlier. In order to achieve a reliable level of calibration, the simulation is run, and the output results are compared with real-world granulator interactions thus allowing the results to be calibrated with reality in this way.

## 5.6 Testing the simulation

Testing the Discrete Element Method (DEM) simulation is a crucial step to ensure that the model accurately represents the physical system and produces reliable results. The results of the simulation are therefore compared to observations from conducting experiments with the Moditec Goliath Plus 2 granulator. Figure 26 shows the result of conducting a DEM simulation using the created environment. To ensure that the simulation shows clear results without making the simulation time extremely long, a high rotation speed of the axis was chosen. This allows the breakage effect of an interaction between particles and granulator geometry to be noticed within seconds.

Furthermore, a gravitational force significantly higher than reality has been selected. This decision serves the purpose of acting as a damping force and preventing particles from shooting away within the simulation. This approach is justified as it ensures more stable simulations and reduces the risk of numerical instabilities, thus enabling a more accurate representation of breakage mechanics in the simulated environment.

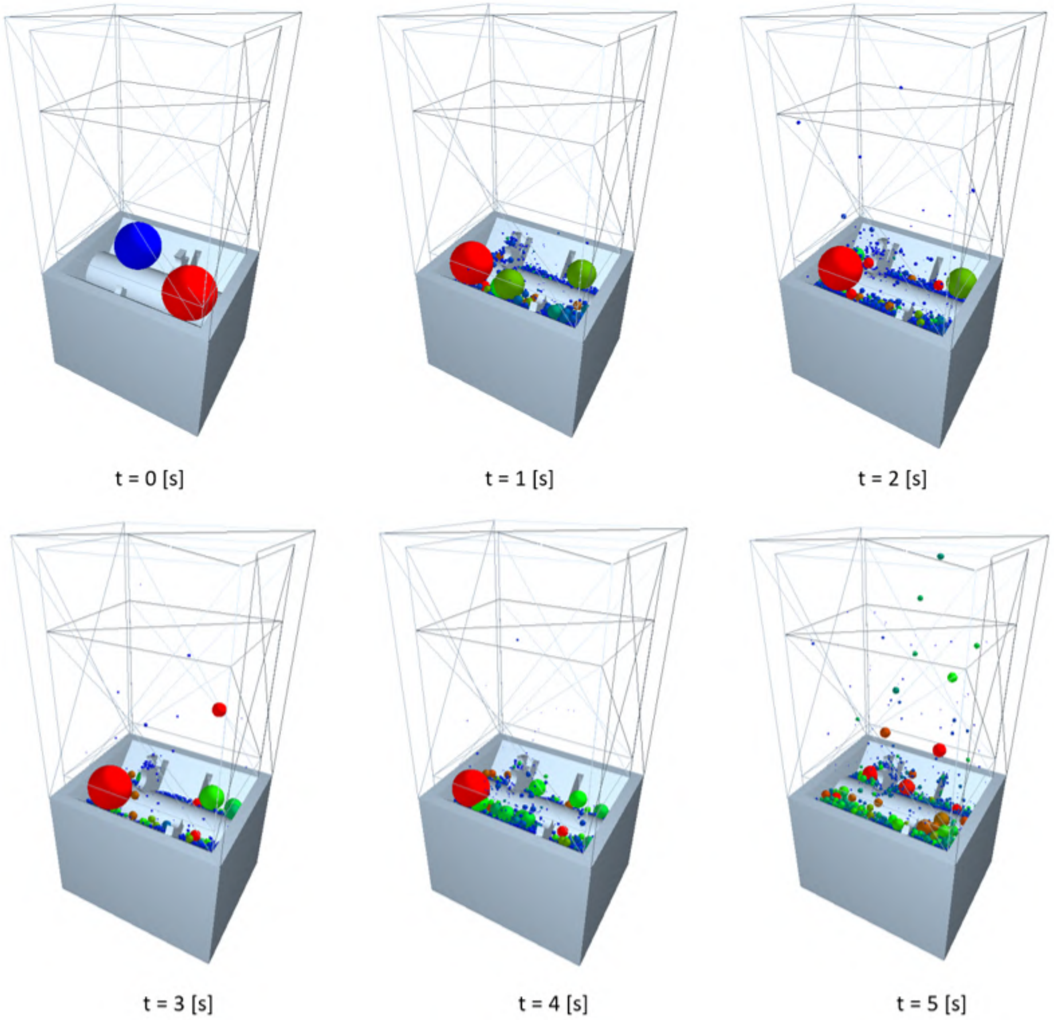

Figure 26: Test simulation 0-5 [s]

As can be seen in figure 26, the particles behave approximately the same in the simulation as in the Moditec Goliath Plus 2 granulator. At time t=0 [$s$], two particles are generated. These particles represent the polypropylene bricks. For the current breakage model, only spherical particles can be used. At time t=1 [$s$], the breakage of the first particle takes place. In subsequent time steps it can be seen that the large particles move to the side of the granulator. This results in a movement of the cutting blades along the particles, so that they initially remain the same size. However, the particles in the center of the granulator are broken down further. This leads to a broad particle size distribution. Only at t=5 [$s$] the largest particle on the side is also being broken. This behavior is consistent with the behavior observed within GreenCycl's facility (see Figure 1).

## 5.7 Design of experiments

The most common types of experimental designs in Design of Experiments (DOE) are often determined by the specific objectives of the study, available resources, and the nature of the factors being investigated. Some of the most commonly used experimental designs of experiments include:

- **Full Factorial Design**: full Factorial Design is a comprehensive experimental design that systematically examines all possible combinations of factor levels for each factor in a study. The notation for a full factorial design is often expressed as $2^k$, where $k$ is the number of factors, and 2 represents the number of levels for each factor (usually high and low). Based on the amount of levels, this number can vary.
- **Fractional Factorial Design**: fractional Factorial Design is a type of experimental design that examines only a fraction of the possible combinations and is denoted as $2^{k-p}$. Again, $k$ is the total number of factors in the full factorial design, and $p$ is the fraction by which the design is reduced. The fraction $2^{k-p}$ indicates that only a subset of the $2^k$ runs in the full factorial design will be carried out. This reduces the number of required experimental runs while still providing information about main effects and certain interactions.

For this research, a full factorial design has been selected. The key performance indicators (KPI's) are divided into the categories: geometrical and operational. Geometrical KPI's consist of the amount of cutting blades and the length of the shaft, while operational KPI's include rotation speed and feeding mechanism. Based on this, it has been decided to conduct five repetitions per geometry. If the repetition results show good agreement, the decision will be made to proceed with simulating the influence of changing the operational parameters. For this purpose, three runs will be conducted per KPI.

| Run | Cutting Blades | Length of Axis | Rotation Speed | Feeding Mechanism |
|---|---|---|---|---|
| 1 | 2 | Short | High | Simultaneous |
| 2 | 2 | Short | High | Simultaneous |
| 3 | 2 | Long | High | Simultaneous |
| 4 | 2 | Long | High | Simultaneous |
| 5 | 3 | Short | High | Simultaneous |
| 6 | 3 | Short | High | Simultaneous |
| 7 | 3 | Long | High | Simultaneous |
| 8 | 3 | Long | High | Simultaneous |
| 9 | 2 | Short | High | Simultaneous |
| 10 | 2 | Short | High | Simultaneous |
| 11 | 2 | Long | High | Simultaneous |
| 12 | 2 | Long | High | Simultaneous |
| 13 | 3 | Short | High | Simultaneous |
| 14 | 3 | Short | High | Simultaneous |
| 15 | 3 | Long | High | Simultaneous |
| 16 | 3 | Long | High | Simultaneous |
| 17 | 2 | Short | High | Simultaneous |
| 18 | 3 | Short | High | Simultaneous |
| 19 | 2 | Long | High | Simultaneous |
| 20 | 3 | Long | High | Simultaneous |
| 21 | 3 | Short | Low | Simultaneous |
| 22 | 3 | Short | Low | Simultaneous |
| 23 | 3 | Short | Low | Simultaneous |
| 24 | 3 | Short | High | Sequential |
| 25 | 3 | Short | High | Sequential |
| 26 | 3 | Short | High | Sequential |

Table 2: Full factorial design of experiments

Due to the presence of an HP Omen 30L GT13-1635nd equipped with an NVIDIA GeForce RTX 3080 (10 GB) GPU, it has been decided to conduct the simulations according to a full factorial design, leveraging the high computational capacity available. However, when simulation capacity or time are more limited, an alternative option is to opt for a fractional factorial design. In such cases, table 3 can be utilized. Nevertheless, to ease the computational load and given the increase in rotation speed, there has been opted for a simulation time of 3 [$s$] per run.

| **Run** | **A (Blades)** | **B (Axis)** | **C (Speed)** | **D (Feeding)** |
|---|---|---|---|---|
| 1 | - | - | - | - |
| 2 | + | - | - | - |
| 3 | - | + | - | - |
| 4 | + | + | - | - |
| 5 | - | - | + | + |
| 6 | + | - | + | + |
| 7 | - | + | + | + |
| 8 | + | + | + | + |

Table 3: Fractional factorial design of experiments

The key performance indicators (KPI's) chosen for the simulation encompass critical aspects of the breakage process and material handling efficiency. The particle breakage rate serves as a fundamental metric, quantifying the rate at which particles fracture within the system across different parameter configurations. Complementing this, the mass flow out of the system offers insight into the overall throughput and efficiency of material processing. Additionally, the analysis of particle size distribution in the exiting material provides crucial data on the quality and consistency of the processed output. By evaluating these KPI's collectively, a comprehensive understanding of the system's performance under varied conditions emerges, enabling informed decisions aimed at optimizing the breakage process for enhanced productivity and product quality.

With this information, some general predictions can be made based on the provided data:

- Runs 5, 6, 7, and 8 have high rotation speed, which tends to increase the mass flow out of the system.
- Runs 2, 4, 6, and 8 have 3 cutting blades, which tends to increase the mass flow out of the system.
- Runs 3, 4, 7, and 8 have a long axis, which tends to decrease the mass flow out of the system.
- Runs 5, 6, 7, and 8 use the simultaneous filling principle, which tends to increase the mass flow out of the system.

Considering these trends, the following predictions can be made:

- Run 3 (2 cutting blades, long axis, low rotation speed and sequential filling) might have the lowest mass flow out of the system among these runs.
- Run 6 (3 cutting blades, short axis, high rotation speed and simultaneous filling) might have the largest mass flow out of the system among these runs.

The predictions shown above are based on the general trends that have been provided. However, one needs to keep in mind that actual results may depend on specific interactions between these factors, and experimental validation is crucial for accurate predictions.

## 5.8 Simulation settings

Table 4 below shows the material and interaction properties used for this research. The reader should bear in mind that the coefficient of restitution and the coefficient of friction values have been left at their default settings because they are not relevant to the study. Compensations have been made by tuning the gravity as the particle damping force.

| **Parameter (Symbol)** | **Interaction** | **Brick** | **Brick Dummy** | **Granulator** |
|---|---|---|---|---|
| Particle shapes $(-)$ | – | Spherical | Spherical | – |
| Particle size $(d_p)$ | – | 75 $[mm]$ | 75 $[mm]$ | – |
| Density $(\rho)$ | – | 900 $[kg/m^3]$ | 900 $[kg/m^3]$ | 7850 $[kg/m^3]$ |
| Poisson's ratio $(\nu)$ | – | 0.45 $[-]$ | 0.45 $[-]$ | 0.30 $[-]$ |
| Young's modulus $(E)$ | – | $1.021 \times 10^9$ $[Pa]$ | $1.021 \times 10^9$ $[Pa]$ | $2.1 \times 10^{11}$ $[Pa]$ |
| Restitution coefficient (e) | B-B | 0.50 $[-]$ | 0.50 $[-]$ | – |
| | B-G | 0.50 $[-]$ | 0.50 $[-]$ | – |
| Static friction coefficient $(\mu_s)$ | B-B | 0.50 $[-]$ | 0.50 $[-]$ | – |
| | B-G | 0.50 $[-]$ | 0.50 $[-]$ | – |
| Rolling friction coefficient $(\mu_r)$ | B-B | 0.50 $[-]$ | 0.50 $[-]$ | – |
| | B-G | 0.50 $[-]$ | 0.50 $[-]$ | – |

Table 4: Values assigned to model parameters

** Abbreviations: B-B = brick-brick, B-G = brick-granulator.*

For the specific input values of parameters in Tavares' breakage model, the overview of mineral ores, where these parameters are already determined, was utilized. Since there hasn't been any calibration done for polypropylene yet, the median values from this overview were considered and used as inputs in Tavares' breakage model in EDEM.

Table 5 displays the key formulas utilized in the Hertz-Mindlin contact model to determine interactions between contact surfaces.

| **Parameter** | **Symbol** | **Equation** |
|---|---|---|
| Normal interaction force, elastic component | $F_{e;n_{ij}}$ | $\frac{4}{3} * E^* * \sqrt{R^*} * (\delta^n)^{\frac{3}{2}}$ |
| Normal interaction force, dissipative component | $F_{d;n_{ij}}$ | $-2 * \sqrt{\frac{5}{6}} * \beta * \sqrt{S^n * m} * v_{n_{\text{rel}}}$ |
| Tangential interaction force, elastic component | $F_{e;t_{ij}}$ | $-S^t * \delta_t$ |
| Tangential interaction force, dissipative component | $F_{d;t_{ij}}$ | $-2 * \sqrt{\frac{5}{6}} * \beta * \sqrt{S^t * m} * v_{t_{\text{rel}}}$ |
| Normal stiffness | $S_n$ | $2 * E^* * \sqrt{R^* * \delta^n}$ |
| Tangential stiffness | $S_t$ | $8 * G^* * \sqrt{R^* * \delta^n}$ |
| Effective radius | $R^*$ | $\left(\frac{1}{R_i} + \frac{1}{R_j}\right)^{-1}$ |
| Effective Young's modulus | $E^*$ | $\left(\frac{1-\nu_i}{E_i} + \frac{1-\nu_j}{E_j}\right)^{-1}$ |
| Effective shear modulus | $G^*$ | $\left(\frac{2-\nu_i}{G_i} + \frac{2-\nu_j}{G_j}\right)^{-1}$ |
| Effective mass | $m^*$ | $\left(\frac{1}{m_i} + \frac{1}{m_j}\right)^{-1}$ |
| Damping ratio | $b$ | $\frac{\ln e}{\sqrt{(\ln e)^2+\pi^2}}$ |

Table 5: Hertz-Mindlin No-Slip Force Models

**Legend:** $\delta_n$: Normal overlap, $\delta_t$: Tangential overlap, $v_{n_{\text{rel}}}$: Relative normal velocity, $v_{t_{\text{rel}}}$: Relative tangential velocity, $\nu$: Poisson ratio, $e$: Restitution coefficient.

# 6 Results & Discussion

The results will be divided into three parts. The first part will examine the effect of geometrical parameters on the granulating performance. For this purpose, the individual performance of the four different geometries will first be assessed. This will be done by examining the number of generated particles, the total mass loss from the system, the mass flow at the exit of the system and the particle size distribution at the exit of the system. In the second part, the performance of the four different geometries will be compared and the best performing geometry will be chosen. This geometry will be used in the third part to investigate the influence of operational parameters such as rotation speed of the axis and filling technique. Based on this, an overview will be provided to determine the best performing geometry with the most efficient operational parameters.

## 6.1 Effect of geometrical parameters on granulating performance

This section will focus on the effect of geometrical parameters on the performance of the granulation process. The geometries are arranged in the following order:

- Long Axis - 2 Cutting Blades
- Long Axis - 3 Cutting Blades
- Short Axis - 2 Cutting Blades
- Short Axis - 3 Cutting Blades

For each simulation, five repetitions are conducted to examine both the granulation speed and the amount and composition of the output.

### 6.1.1 Geometry 1: Long Axis - 2 Cutting Blades

The first geometry consists of a long rotating axis with two cutting blades attached to it. More details about this geometry can be found in appendix C.

**Total amount of generated particles**

In figure 27, the total number of generated particles over time is plotted for geometry 1 using five repetitions. In figure 27a, the individual repetitions are plotted, while in figure 27b, the average of the five repetitions are plotted. It is noticeable that four out of the five repetitions closely resemble each other, while one of the repetitions lags behind. This is due to the fact that the particles are smaller than the space between the two rotating cutting blades. As a result, there may be moments when the particles do not pass between the rotating cutting blades and the casing. Consequently, few new particles are generated, causing the line to remain almost horizontal.

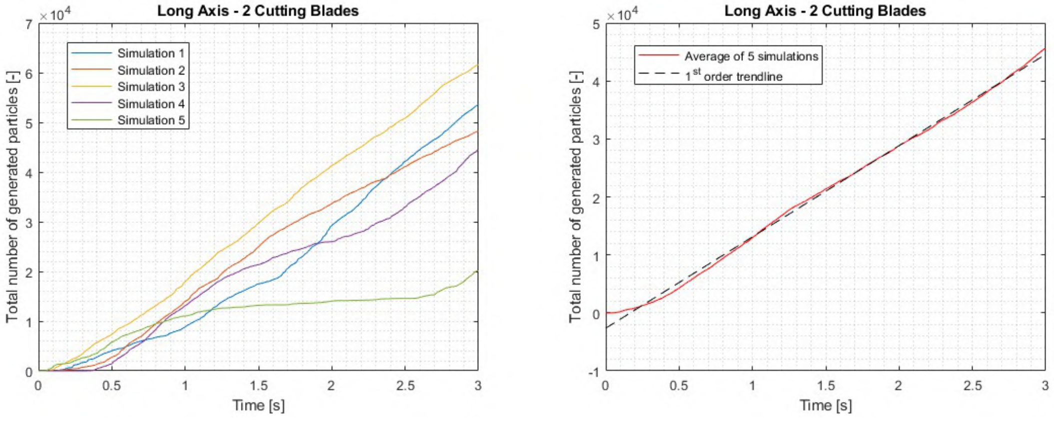

(a) Individual repetitions

(b) Average of five repetitions

Figure 27: Number of generated particles for geometry 1

From t = 2.5 $[s]$ onward, an increase in the number of particles is observed again, indicating that the particles are being granulated once more. As seen in figure 27b, the quantity of generated particles increases approximately linearly.

### Total loss of mass in system

Figure 28 indicates the total loss of mass for geometry 1. As can be seen in figure 28a, the data from four out of the five repetitions align well. However, in one of the five repetitions, a steep slope is observed at t = 0.07 $[s]$. This slope can be explained by a loss of ability to capture the total mass during a high impact collision. EDEM is unable to compensate for this in the next time step. In figure 28b the average of the five repetitions is shown. Here it can be observed that the steep slope of one repetition is balanced out by the other four runs and therefore only has a slight impact. Based on the data, the total loss of mass is observed to be around 0.5 $[kg]$ in 3 seconds time. It can also be noticed that the total loss of mass from the system has a linear relation.

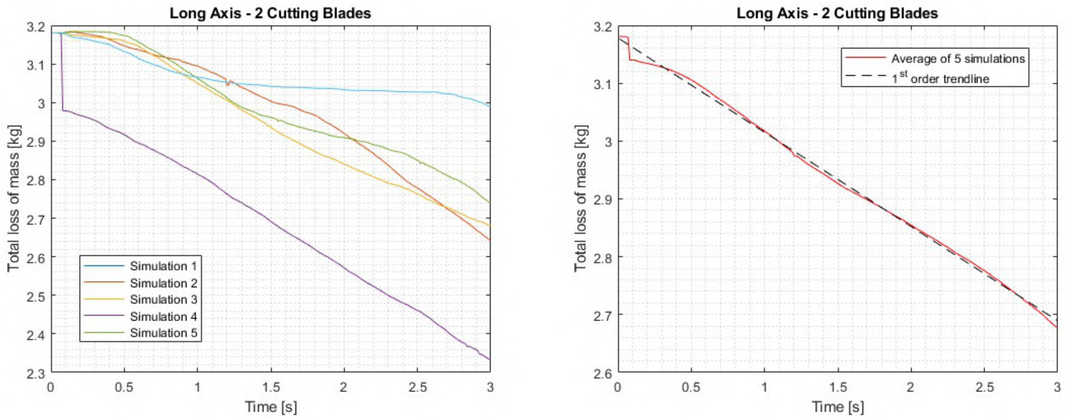

(a) Individual repetitions

(b) Average of five repetitions

Figure 28: Total loss of mass for geometry 1

### Determining mass flow rate from total loss of mass

By taking the derivative of the total loss of mass in the system, the mass flow rate can be determined. In figure 29a, the derivative of the average of the total loss of mass from figure 28b is shown. It is notable that there is a significant peak at t = 0.07 $[s]$. This can be explained by the large jump in the total mass inside the system mentioned earlier. This is accompanied by a peak in the mass flow rate.

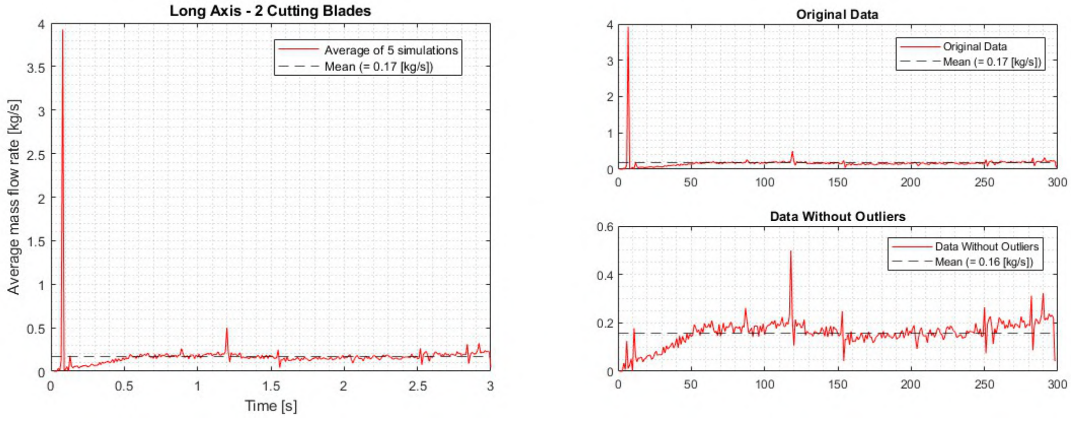

(a) Unfiltered data

(b) Filtered data

Figure 29: Differentiated mass flow rate for geometry 1

To compensate for this, the outlier has been filtered out of the system (figure 29b). It can be noticed that this does not have a significant effect on the average value of the mass flow rate. It changes from 0.17 [$kg/s$] (unfiltered) to 0.16 [$kg/s$] (filtered). This is because this phenomenon occurs only at one time step, and thus, the peak is high but very narrow. Nevertheless, removing the outlier provides a more accurate and representative result.

### Determining mass flow rate using sensor in EDEM

Mass should only be able to exit the system through the bottom by passing through the slots next to the rotating axis. When the time step is chosen to be too large, it is possible for mass to escape through the walls of the geometry. Therefore, it is important to compare the total loss of mass and the corresponding mass flow rate from the system viewed as a whole with the mass flow rate measured at the bottom of the granulator.

Figure 30 presents the result for five repetitions of installing a mass flow sensor at the bottom of the geometry. It must be noted that the mass flow rate is indicated as negative in the graph because, in the simulations, the y-direction is defined upwards, causing the mass to counteract this direction due to gravity. It can be observed that the data from the five different repetitions, with a few outliers aside, closely matches an average value of approximately 0.20 [$kg/s$].

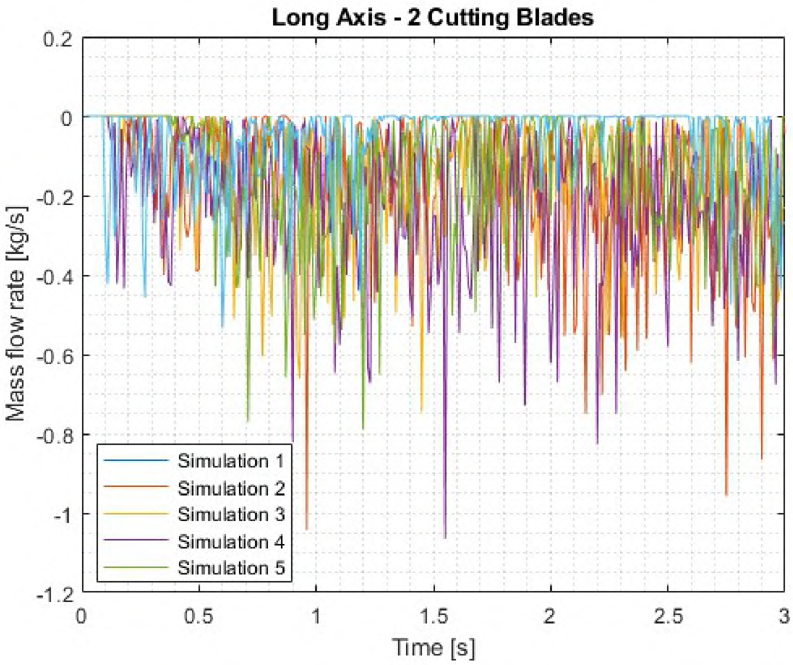

Figure 30: Sensed mass flow rate for individual repetitions for geometry 1

To clarify the average mass flow rate measured by the sensor, figure 31a includes the averages of the five repetitions. Because the mass flow rate fluctuates significantly, a filtered signal is also shown (Figure 31b). For this purpose, a Savitzky-Golay filter was applied. This is a digital filter used for signal smoothing by fitting a polynomial within a sliding window of adjacent data points, preserving signal features while reducing noise. When the average value is taken from the filtered signal (0.15 [$kg/s$]), it can be observed that it closely matches the differentiated total loss of mass value (0.16 [$kg/s$]). This confirms that the time step is well chosen and that the mass indeed exits the system through the opening at the bottom.

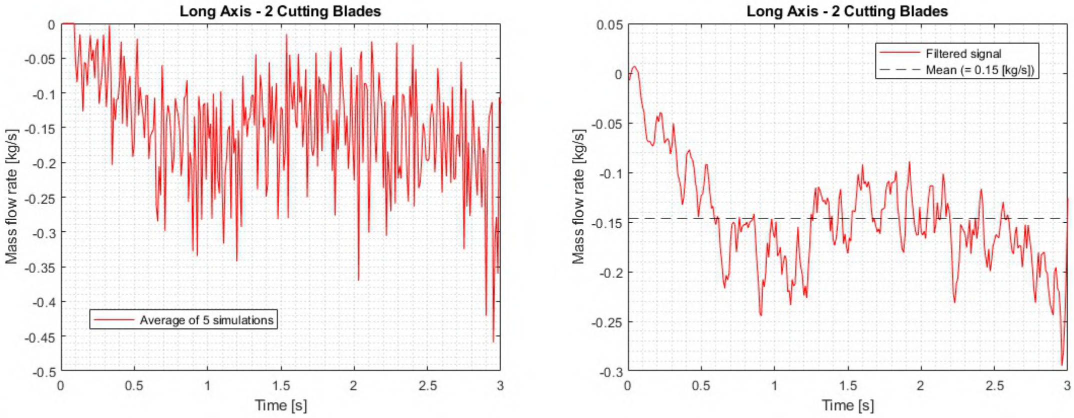

(a) Unfiltered data

(b) Filtered data

Figure 31: Sensed mass flow rate for geometry 1

### Comparing particle size distribution at exit

Figure 32 shows the ratio between the sizes of particles exiting the granulator at the bottom. Since the slots through which the particles pass have a diameter of 5 $[mm]$, this is the maximum particle size that can be detected in the outgoing flow. Because particles with a diameter smaller than 3 $[mm]$ are considered undesired for injection molding, the total mass of these particles has also been tracked. The ratio between the total particle flow and the percentage of fines (particles with a diameter smaller than 3 $[mm]$) is 20.81 %. Additionally, it can be seen that both the total particle flow and the flow of fines increase linearly.

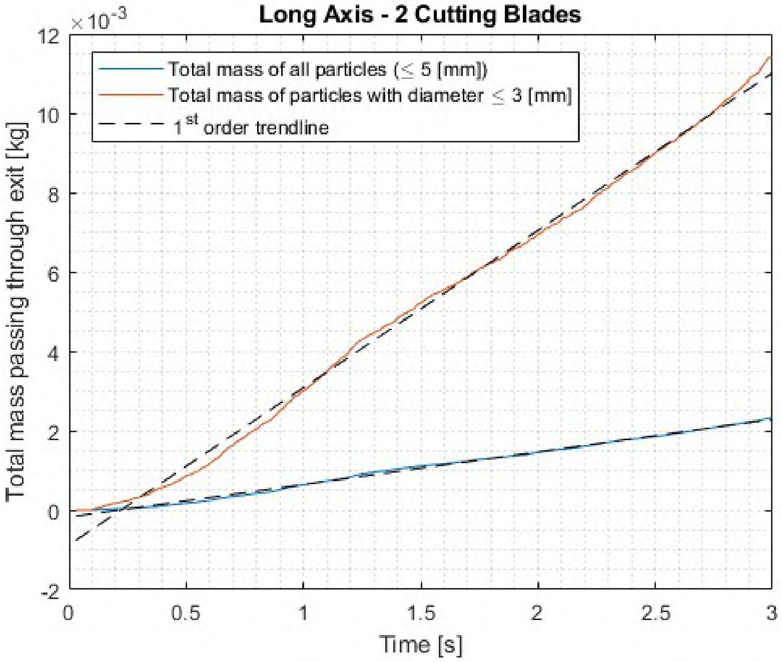

Figure 32: Particle size distribution of exiting material for geometry 1

### 6.1.2 Geometry 2: Long Axis - 3 Cutting Blades

The second geometry consists of a long rotating axis with three cutting blades attached to it. More details about this geometry can be found in appendix C.

#### Total amount of generated particles

Figure 33a displays the total number of generated particles. As depicted, three out of the five repetitions exhibit close agreement. However, in the remaining two repetitions, the number of generated particles is notably higher. This discrepancy is attributed to the onset of initial particle breakage. While one repetition initiates as early as t = 0.5 [*s*], others commence around t = 1.5 [*s*]. Moreover, in figure 33b, it is evident that, contrary to geometry 1, the particle generation rate increases exponentially. This phenomenon likely stems from the presence of additional cutting blades, resulting in a rapid proliferation of particles following the initial cut.

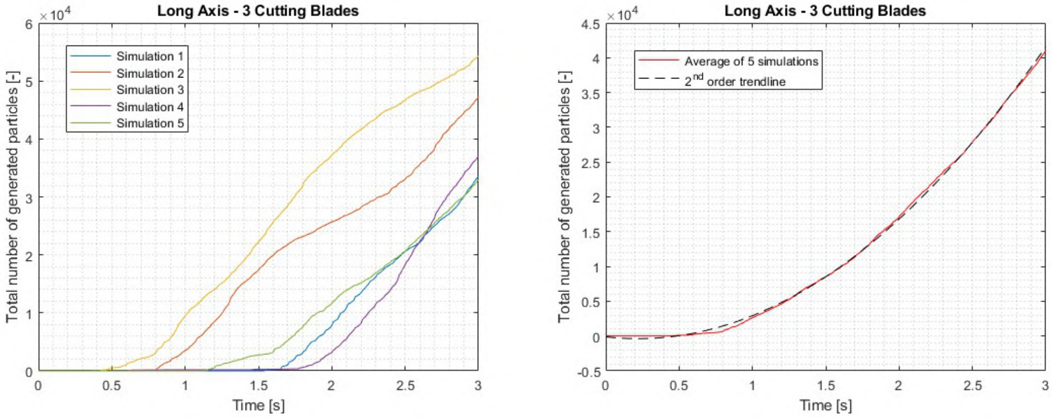

(a) Individual repetitions

(b) Average of five repetitions

Figure 33: Number of generated particles for geometry 2

#### Total loss of mass in system

As can be seen in figure 34a, the total mass loss from the system corresponds to the number of generated particles. The difference compared to geometry 1 is that the number of generated particles in geometry 2 almost immediately translates into the number of particles leaving the system. This relationship is less evident in geometry 1. This suggests that particles are better evacuated in a geometry with a long shaft and three cutting blades compared to one with a long shaft and two cutting blades. Furthermore, in figure 34b, it is observed that the average of five repetitions of the total mass in the system also decreases exponentially. This is in contrast to geometry 1, where the total mass decreases approximately linearly.

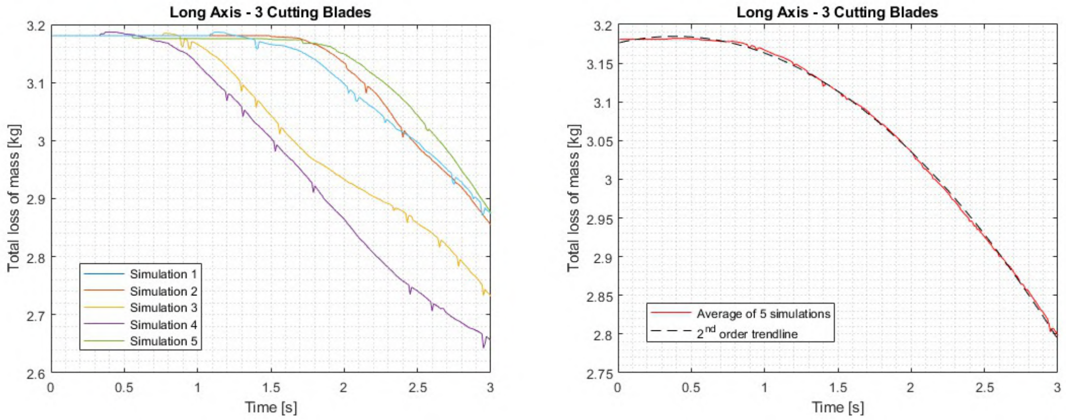

(a) Individual repetitions

(b) Average of five repitions

Figure 34: Total loss of mass for geometry 2

### Determining mass flow rate from total loss of mass

When the derivative is taken from the total loss of mass, the mass flow rate can be calculated. As seen in figure 35, the mass flow fluctuates around an average value (0.15 $[kg/s]$). This value is comparable to the filtered mass flow of geometry 1 ($= 0.16$ $[kg/s]$). The peaks can be explained by the fact that multiple particles can leave the system simultaneously, and this process occurs randomly. However, it is noticeable that the peaks are becoming increasingly larger. This is due to the fact that as time progresses, more particles become small enough to leave the system. This also means that the mass flow will slowly increase. However, for this study, only the average mass flow over 3 $[s]$ has been considered.

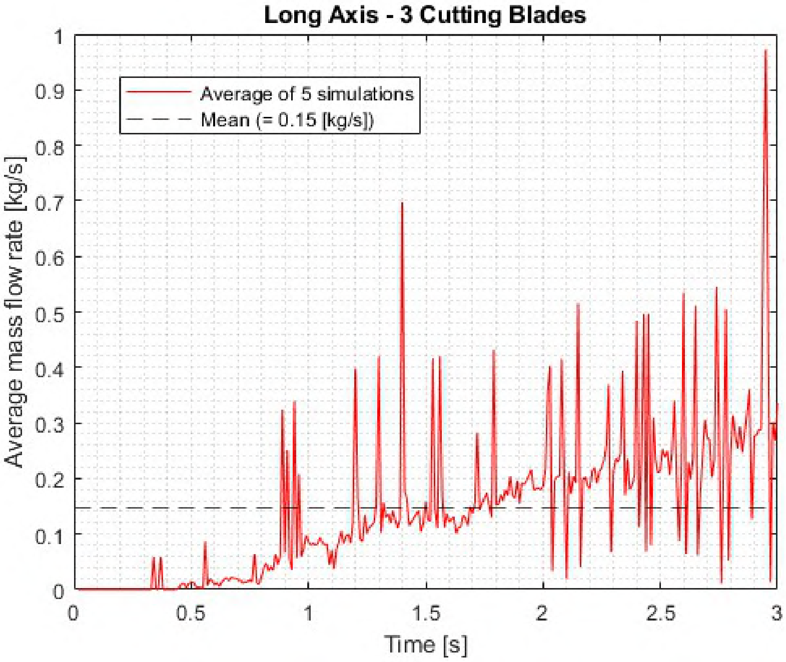

Figure 35: Differentiated mass flow rate for geometry 2

### Determining mass flow rate from sensor in EDEM

When the mass flow rate is approximated by considering a sensor response, the result is shown in figure 36. The figure contains two outliers: one at t = 1.35 [$s$] and one at t = 3 [$s$]. These outliers correspond to the differentiated total mass, indicating that the mass flow out of the system indeed occurs through the slots at the bottom of the granulator.

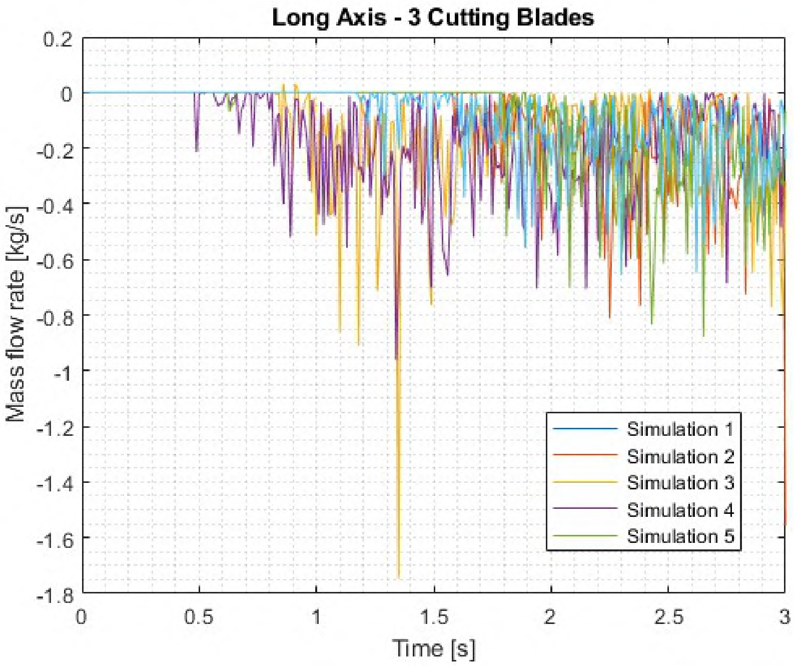

Figure 36: Sensed mass flow rate for individual repetitions for geometry 2

When the average of the five repetitions is taken, figure 37a follows. Because the signal contains a considerable amount of noise, a Savitzky-Golay filter has also been applied. The filtered signal can be found in figure 37b. Also in this figure, it can be observed that the average of five repetitions exhibits a decreasing trend. It is notable that the difference between the differentiated total mass and the mass flow rate is larger compared to geometry 1. One possible explanation for this is the instability of the mass flow rate with respect to geometry 1.

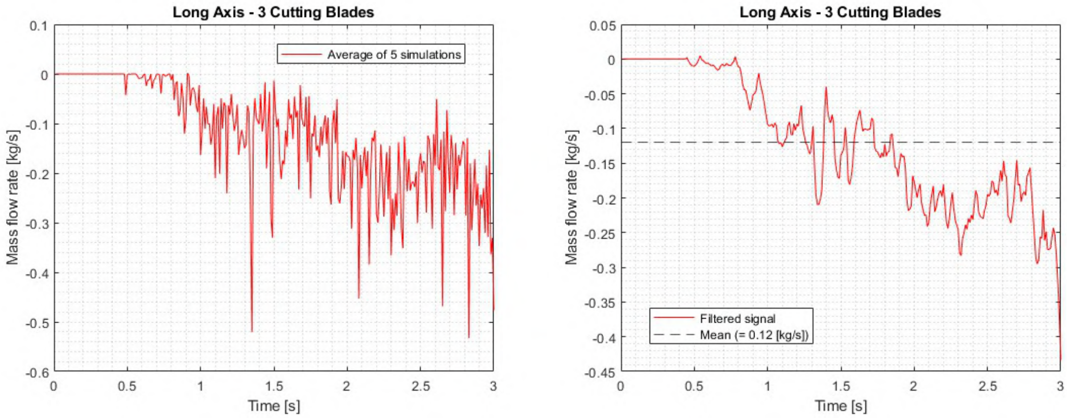

(a) Unfiltered data

(b) Filtered data

Figure 37: Sensed mass flow rate for geometry 2

### Comparing particle size distribution at exit

Figure 38 depicts the number of particles smaller than or equal to 3 [$mm$] relative to the total mass flow. It can be observed that both size distributions increase exponentially, with the overall mass flow rising faster than the mass flow containing dust. It is found that the total percentage of dust relative to the total mass leaving the system is 22.02 %. Compared to geometry 1 (20.81 % dust), this represents a slight increase. Thus, if one aims to minimize dust generation with a long shaft, geometry 1 is the better choice.

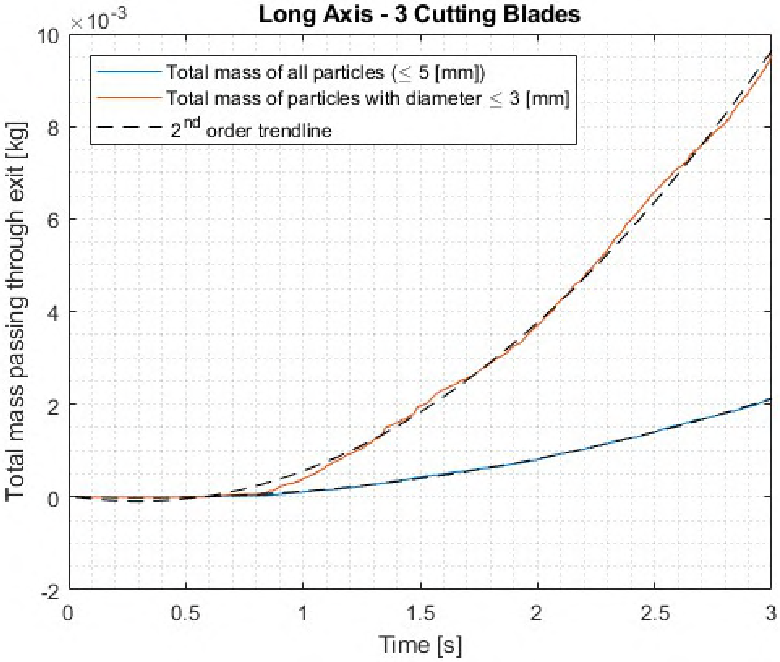

Figure 38: Particle size distribution for exiting material for geometry 2

### 6.1.3 Geometry 3: Short Axis - 2 Cutting Blades

The third geometry consists of a short rotating axis with two cutting blades attached to it. More details about this geometry can be found in appendix C.

#### Total amount of generated particles

Figure 39a shows the number of particles generated for geometry 3 using five repetitions. Remarkably, unlike as is occurring in geometries 1 and 2, the increase in the number of particles shows less deviation. This is due to the fact that the amount of cutting blades per length of axis is significantly higher in this case compared to the earlier geometries using a long axis. Consequently, the likelihood of a particle being reduced by one of the cutting blades is much greater, rather than it bouncing on the axis. Figure 39b displays the average of the five simulations. It is evident that the number of particles generated increases almost linearly.

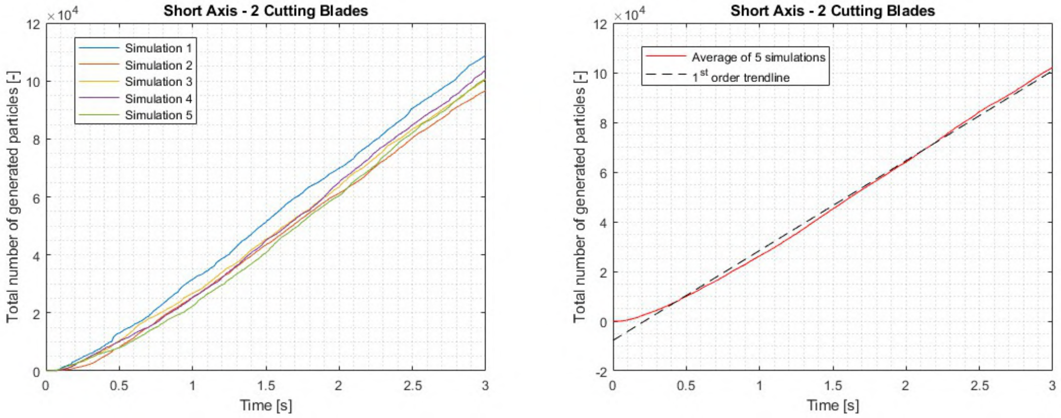

(a) Individual repetitions

(b) Average of five repetitions

Figure 39: Number of generated particles for geometry 3

#### Total loss of mass in system

Figure 40a illustrates the total loss of mass in the system. A notable occurrence is the sharp peak at t $= 0.04$ $[s]$. This peak can be attributed to the significant forces released at the moment of initial impact. To accurately determine the material's breaking behavior, the system therefore skips a time step. The system then compensates for this at the next time step.

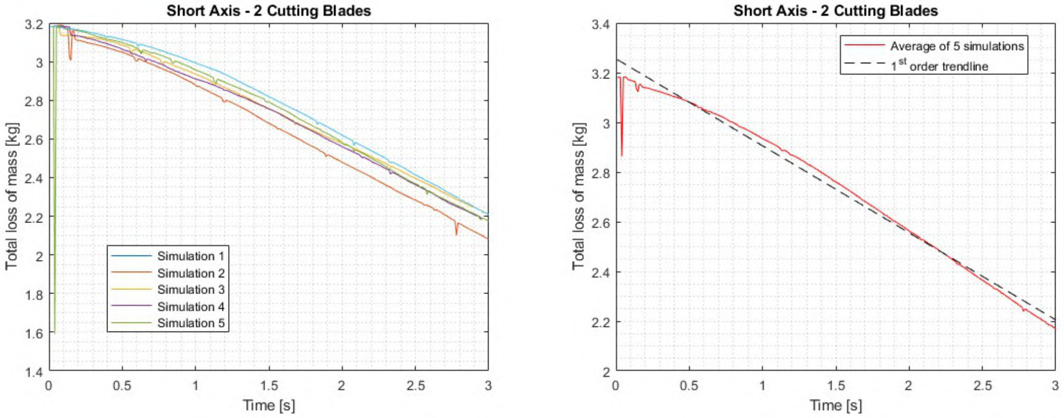

(a) Individual repetitions

(b) Average of five repetitions

Figure 40: Total loss of mass for geometry 3

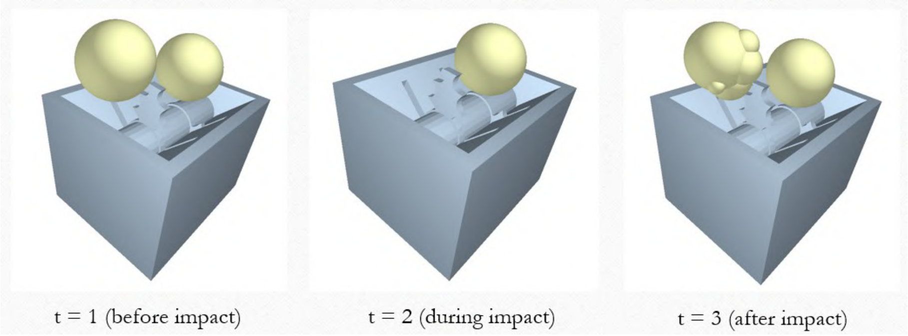

Figure 41: Loss of mass

This effect is also, to a lesser extent, visible at t = 0.15 $[s]$, as visualized in figure 41. When considering the average of the five repetitions, as shown in figure 40b, it becomes apparent that the total loss of mass decreases approximately linearly. This is in contrast to geometry 2, where this decrease occurs exponentially. Hence, it can cautiously be concluded that the quantity of blades influences the manner (linear or exponential) in which particles exit the system.

### Determining mass flow rate from total loss of mass

Figure 42a depicts the mass flow rate based on the total mass loss out of the system. It is noteworthy that the peak at the beginning of the figure exerts a significant influence on the average mass flow rate. Despite the narrowness of the peak, its considerable height greatly impacts the mean value of the mass flow rate. Hence, in this case, a filter has been employed, as shown in figure 42b. On the left side of the figure, the second-largest peak from figure 42a is visible. However, this peak exerts a much smaller influence on the average value compared to the first peak and therefore has been retained in the plot. Using a filter, the average mass flow rate out of the system has been calculated and has a value of 0.38 $[kg/s]$.

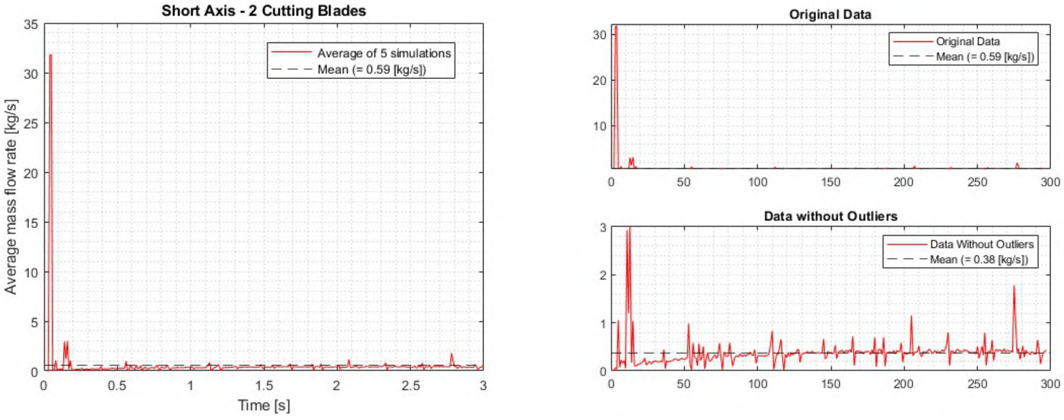

(a) Unfiltered data

(b) Filtered data

Figure 42: Differentiated mass flow rate for geometry 3

### Determining mass flow rate using sensor in EDEM

When a mass flow sensor is utilized at the bottom of geometry 3, figure 43 is obtained. It can be observed that the mass flow, apart from a few instances, fluctuates around an average value for the five repetitions.

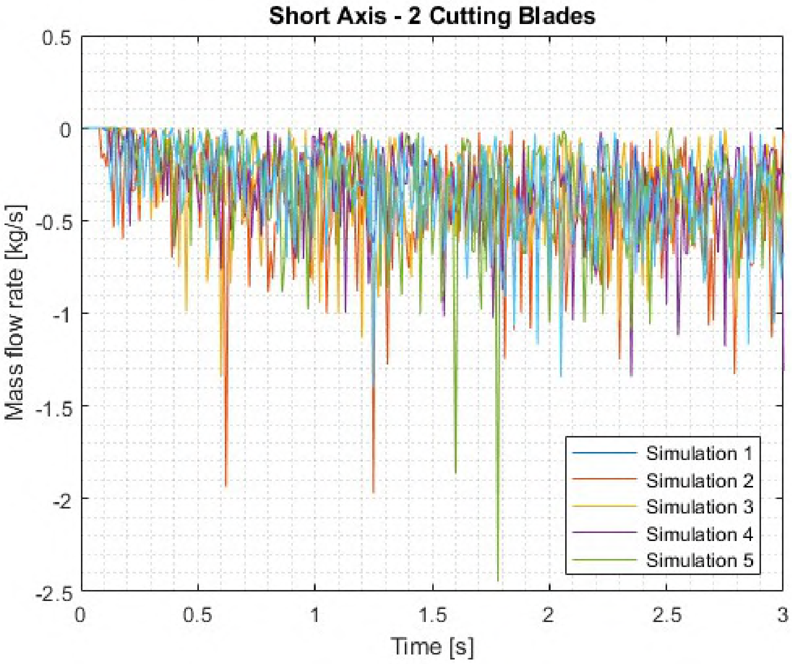

Figure 43: Sensed mass flow rate for individual repetitions for geometry 3

Upon determining the average mass flow rate of the five repetitions, figure 44a is obtained. When the signal is filtered using a Savitzky–Golay filter, figure 44b emerges. This figure bears a striking resemblance to figure 37b of geometry 2. In geometries 1, 2, and 3, a decreasing trend is noticeable before the mass flow stabilizes around an average value. However, in geometry 1 and 3 (figure 31b), it takes considerably shorter for the initial decrease to occur and for the average value to be reached. This is accompanied by a lower mass flow (0.15 $[kg/s]$ for geometry 1 and 0.12 $[kg/s]$ for geometry 2), compared to 0.34 $[kg/s]$ for geometry 3. This implies that a geometry with a short axis is more adept at generating a high mass flow at the exit (in the short term).

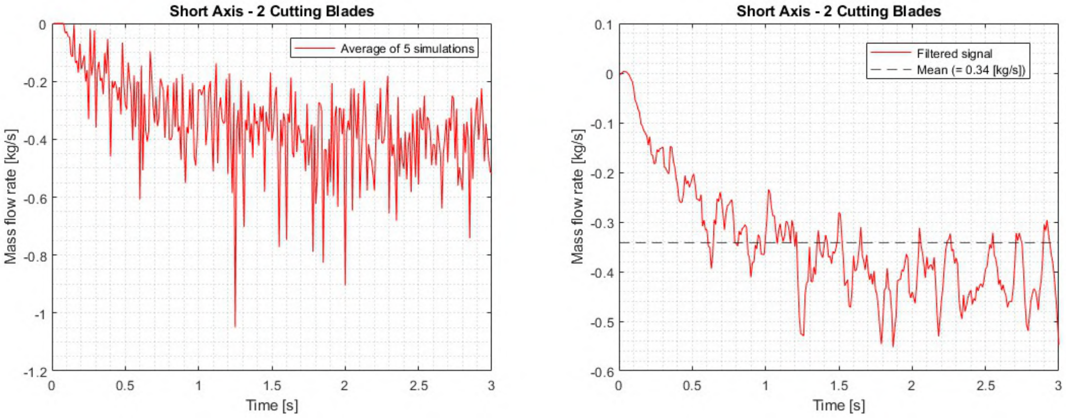

(a) Unfiltered data

(b) Filtered data

Figure 44: Sensed mass flow rate for geometry 3

### Comparing particle size distribution at exit

Figure 45 illustrates the particle size distribution at the exit of the geometry. It is notable that the trends of both size classes, similar to geometry 1 (figure 32), are almost linear. This is in contrast to geometry 2 (figure 38), where both classes increase exponentially. Thus, it appears that the use of two cutting blades has a different effect on the graph's trend compared to the use of three cutting blades. Regarding the ratio of dust to the total outgoing mass flow, all three geometries exhibit fairly similar values: 20.81 % dust for geometry 1, 22.02 % dust for geometry 2, and 19.75 % dust for geometry 3.

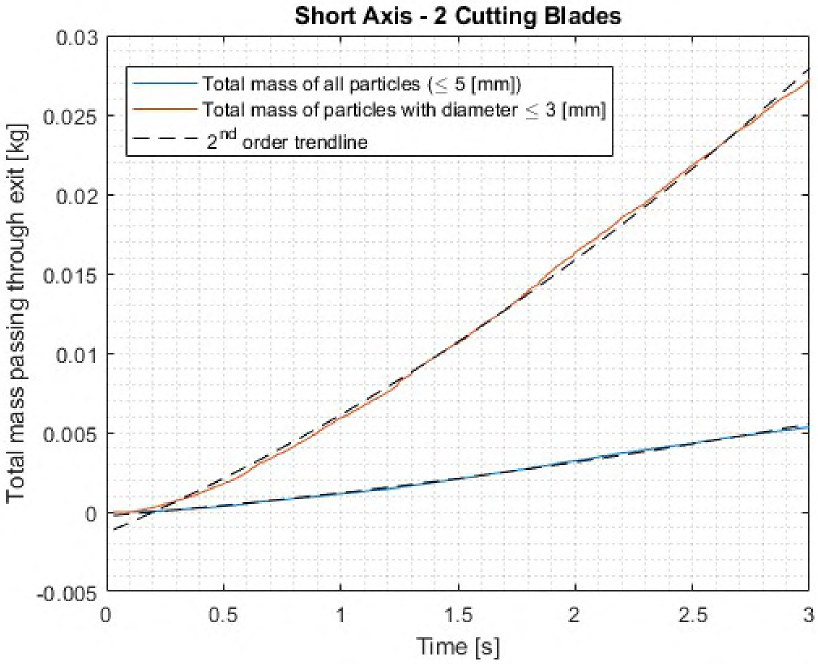

Figure 45: Particle size distribution of exiting material for geometry 3

### 6.1.4 Geometry 4: Short Axis - 3 Cutting Blades

The fourth geometry consists of a short rotating axis with three cutting blades attached to it. More details about this geometry can be found in appendix C.

#### Total amount of generated particles

Figure 46a illustrates the increase in the total number of generated particles for geometry 4. Again, as could also be seen in figure 39a, the different repetitions closely resemble each other. This is most likely due to the fact that there are more cutting blades per unit area, reducing the chance of particles remaining in motion within the geometry without being broken. Furthermore, it is noticeable that this geometry is the only one showing an exponentially decreasing trend, while the other geometries show an exponentially increasing trend (figure 27a and figure 33a) or a nearly linear trend (figure 39a). Figure 33b shows the average of five repetitions, making the exponentially decreasing trend even more evident.

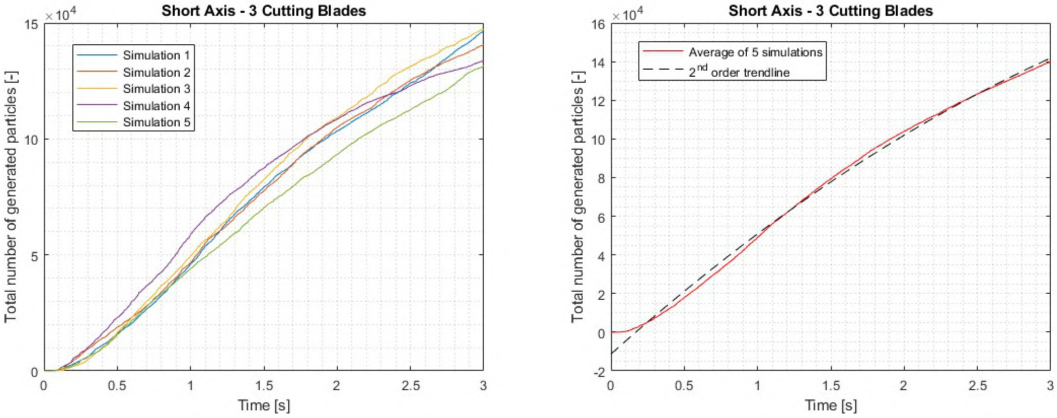

(a) Individual repetitions

(b) Average of five repetitions

Figure 46: Number of generated particles for geometry 4

#### Total loss of mass in system

Figure 47a depicts the total mass loss from geometry 4. Here again, the five repetitions closely align with each other. Additionally, of all four geometries, the most mass leaves the system here. The trend is steeper than that of geometry 3 (figure 40a) due to the presence of an extra cutting blade. Also, from the beginning of the simulation, there is immediately a decline visible in both geometries, whereas in geometry 1 (figure 28a) and geometry 2 (figure 34a), it takes longer. This is because in these geometries, the particles are not yet small enough to exit the system.

Figure 47b shows the average of the five repetitions. It is noticeable that the simulations using three cutting blades are more stable than those using two cutting blades. This may be due to the fact that forces are better distributed, and the simulation does not need to skip a time step to calculate forces and breakage patterns.

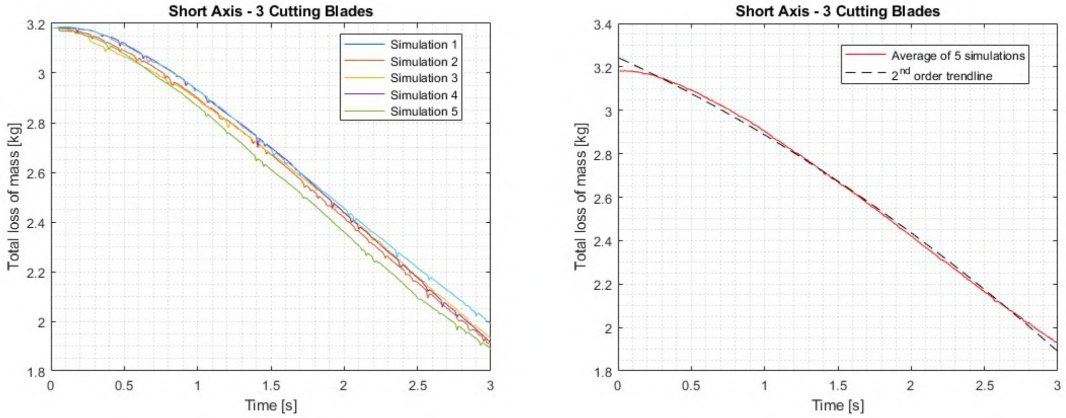

(a) Individual repetitions

(b) Average of five repetitions

Figure 47: Total loss of mass for geometry 4

### Determining mass flow rate from total loss of mass

When the derivative is taken of the total loss of mass in the system, figure 48 is generated. In this figure, it is clear that the average mass flow rate moves fairly consistently around the mean. This is consistent with figure 47b, where it was already indicated that the mass leaves the system in a linear approaching way. It is also noticeable that the mass flow rate for the geometry is the highest among all geometries. In this case as high as 0.43 $[kg/s]$

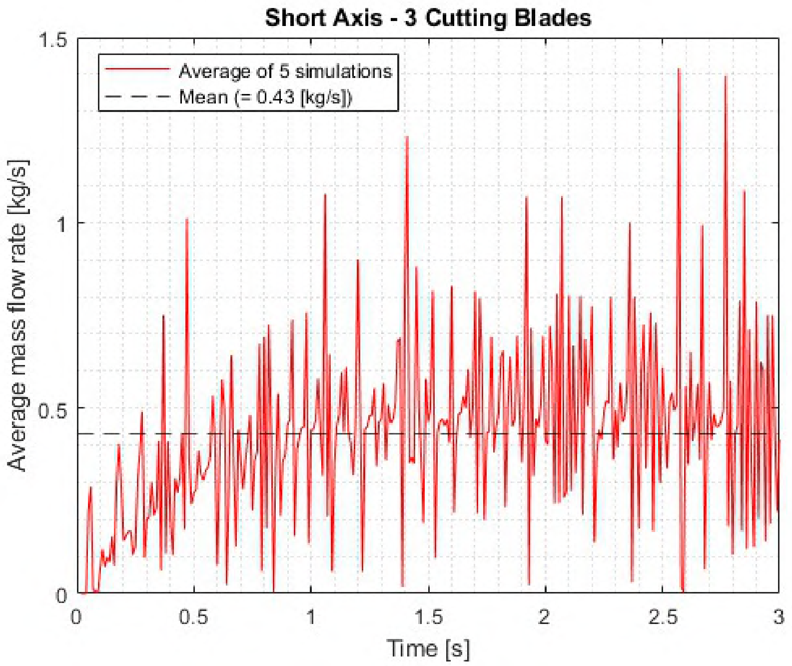

Figure 48: Differentiated mass flow rate for geometry 4

### Determining mass flow rate using sensor in EDEM

When the mass flow rate at the exit is measured using a sensor, figure 49 is generated. Also here, it can be seen that the simulations align well with each other, and there are no extreme individual outliers in the mass flow rate.

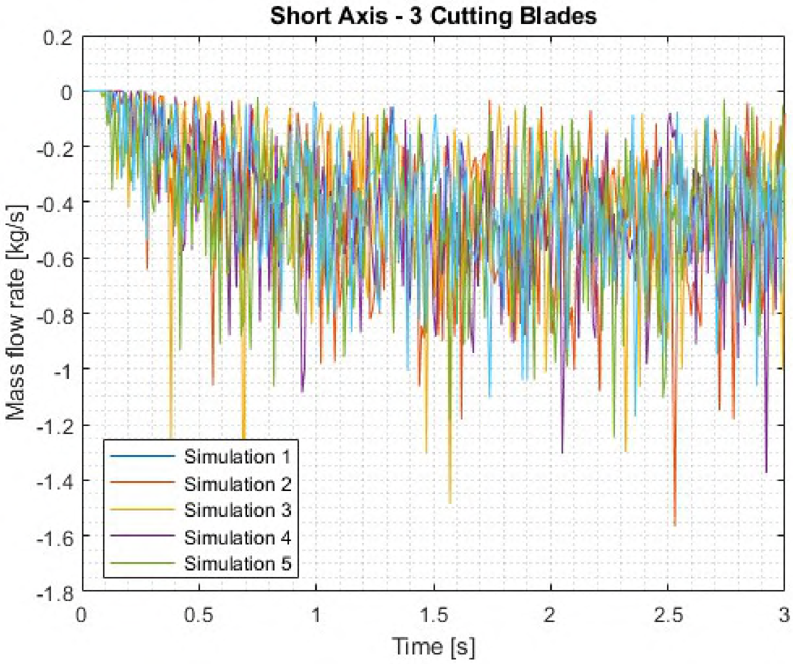

Figure 49: Sensed mass flow rate for individual repetitions for geometry 4

When the average is taken of the five repetitions, figure 50a is generated. Also here, a Savitzky-Golay filter has been used (figure 50b) to remove most of the noise. The pattern is similar to figure 44b, where it takes a certain amount of time for the particles to reach the bottom of the geometry, but then they move approximately constantly around a mean value. The value of 0.41 $[kg/s]$ given by the sensor of figure 50b corresponds well to the differentiated value of 0.43 $[kg/s]$ from figure 50a.

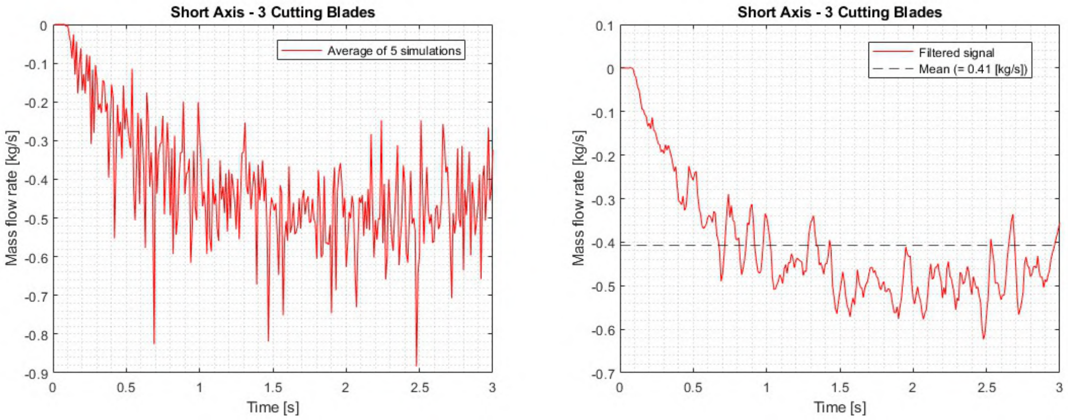

(a) Unfiltered data

(b) Filtered data

Figure 50: Sensed mass flow rate for geometry 4

### Comparing particle size distribution at exit

Figure 51 depicts the particle size distribution for geometry 4. What excels in this figure is that both lines also exhibit an exponential trend, contrary to geometry 1 (figure 32). This confirms the earlier suspicion that the number of cutting blades influences the trend of the graph. In this case, the percentage of dust (27.49 %) is also considerably higher than in the geometries with two cutting blades instead of three. This is due to the fact that more breakages occur before the material disappears through the bottom of the granulator.

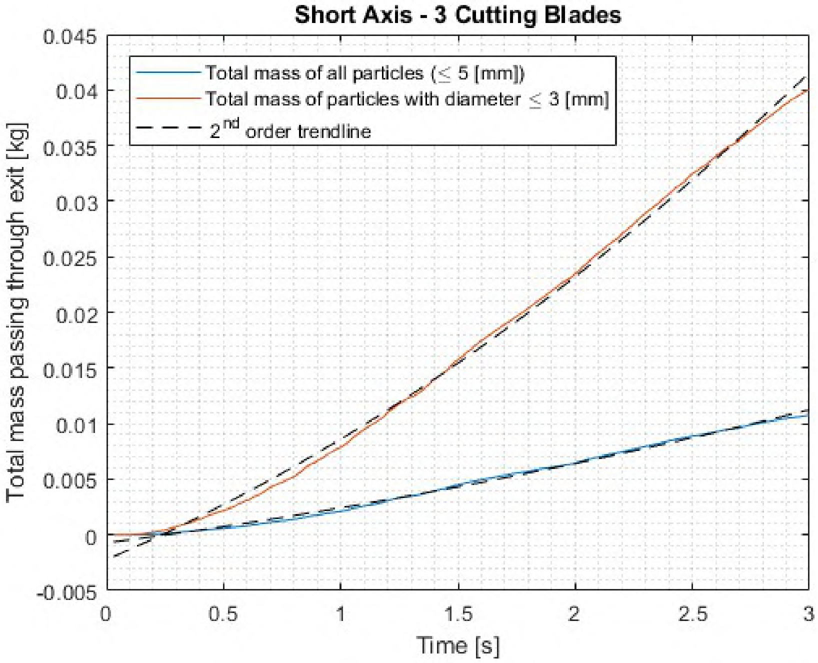

Figure 51: Particle size distribution of exiting material for geometry 4

### Overall comparison table

Table 6 and figure 52 compare the output and particle size distribution of the different geometries. In general, it can be stated that while a shorter axis and more cutting blades increase output, this will also be accompanied by the creation of more dust. This output increases significantly when more cutting blades are installed in combination with a short axis. When minimizing dust creation is desired, it is advisable to opt for geometry 3 (Short Axis - 2 Cutting Blades). When aiming for high output, it is wise to choose geometry 4 (Short Axis - 3 Cutting Blades). However, geometry 3 provides a relatively high output with a low amount of dust and will therefore be the best choice in most situations.

| **Geometry** | **Mass flow** $[kg/s]$ | **Amount of particle** $\leq$ **3** $[mm]$ |
|---|---|---|
| Long Axis - 2 Cutting Blades | 0.15 | 20.81 % |
| Long Axis - 3 Cutting Blades | 0.12 | 22.02 % |
| Short Axis - 2 Cutting Blades | 0.34 | 19.75 % |
| Short Axis - 3 Cutting Blades | 0.41 | 27.49 % |

Table 6: Overall comparison between different geometries

Figure 52 is a scatter plot of the four geometries. The x-axis represents the mass flow, and the y-axis indicates the amount of dust generated. It is clear that when a long axis is used, the difference between the mass flow and the amount of dust being generated is considerably small. In contrast, this difference is much larger when a short axis is being used. In this case, the mass flow is approximately the same, while the amount of generated dust is considerably larger when using three cutting blades instead of two.

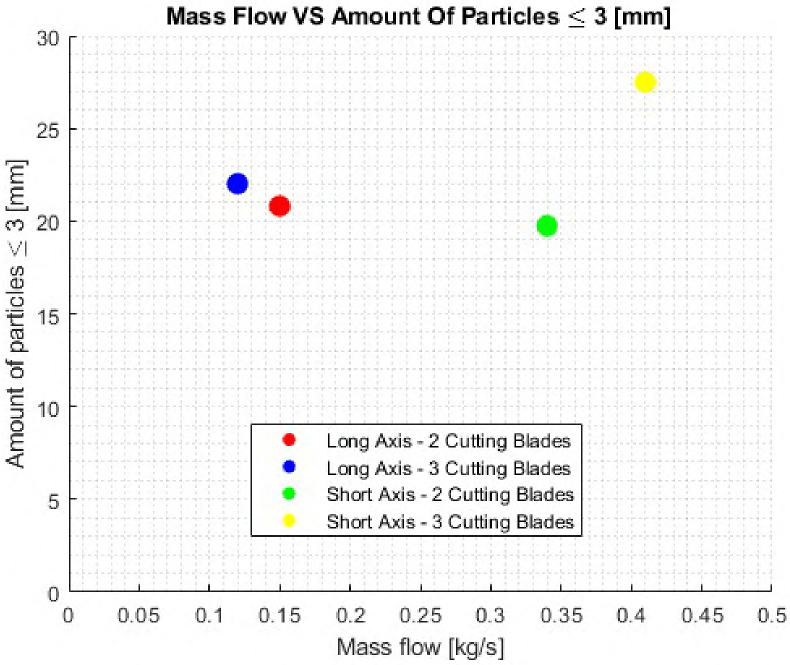

Figure 52: Overall geometrical performance comparison

## 6.2 Effect of rotational speed on granulating performance

From the four geometries, the best-performing geometry has been chosen. In this case, geometry 4 (Short Axis - 3 Cutting Blades) has been selected. This is despite the fact that this geometry generates more dust than geometry 3 (Short Axis - 2 Cutting Blades) and only offers a small increase in mass flow. The reason for this choice is the fact that GreenCycl B.V. currently aims to achieve the highest possible output and considers a reduction in the percentage of dust to be less significant.

In the initial setup, a rotation speed at full throttle (full speed) of 3600 $[deg/s]$ was assumed. In the subsequent simulation, the best performing geometry is set to rotate at half throttle (half speed), with a rotation speed of 1800 $[deg/s]$. Given the time-intensive nature of the process, it is decided to perform three repetitions in this case. This choice stems from the observation in previous simulations that, for this geometry, the results per repetition tend to cluster closely together.

### Total amount of generated particles

Figure 53a shows the total number of generated particles per repetition. It is notable that initially, the three runs closely follow almost the exact same pattern. However, as time progresses, the simulations diverge further apart. This is in contrast to the situation where the geometry is rotating at full speed (figure 46a). One explanation for this is that at a lower speed, there will be fewer fracture interactions per unit time, and the particles will move less dynamically through the geometry.

Figure 53b shows the average of the three repetitions. It is striking that, in contrast to the exponentially decreasing trend at full speed (figure 46b), an exponentially increasing trend is observed here. This is also due to the fact that fewer fracture interactions occur per unit time, and thus the particles will exit the system less quickly compared to when the geometry is rotating at full speed. Furthermore, it is noticeable that the total number of generated particles does not halve. At t = 3 $[s]$, there are $0.9 * 10^5$ particles for half speed compared to $1.4 * 10^5$ for full speed. This means that halving the speed still results in the creation of approximately 65 % of the number of particles compared to full speed.

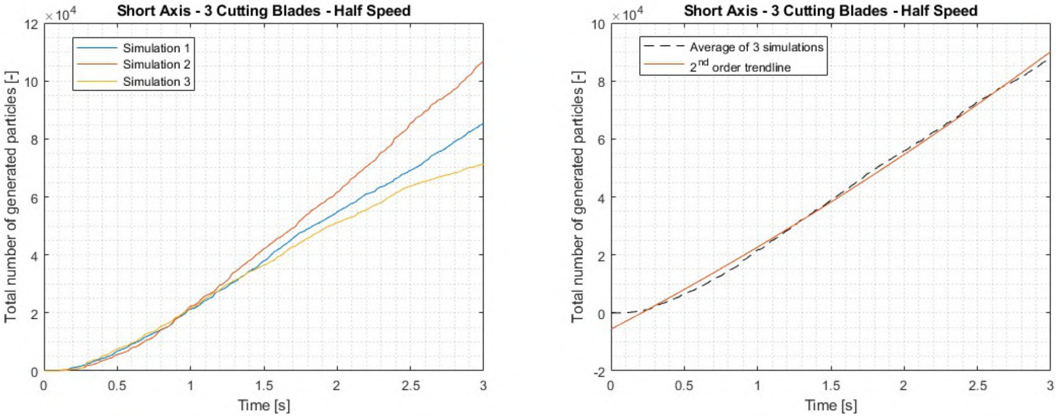

(a) Individual repetitions

(b) Average of three repetitions

Figure 53: Number of generated particles for geometry 4 with half speed

### Total loss of mass in system

Figure 54a shows the total mass loss for geometry 4 at half speed. Similar to the full-speed scenario, an exponentially decreasing trend is observed here as well. Interestingly, unlike the total number of generated particles in figure 53a, the total mass loss for the three repetitions closely matches.

Figure 54b displays the average of the three repetitions. Also here, the exponentially decreasing trend is clearly visible. It is notable that at t = 3 [$s$], there is still approximately 2.5 [$kg$] of mass remaining in the system. This is in contrast to the full-speed scenario, where at t = 3 [$s$], approximately 1.9 [$kg$] of mass remains in the system (figure 47b). This means that rotating at half speed results in only 55 % of the mass leaving the system compared to rotation at full speed.

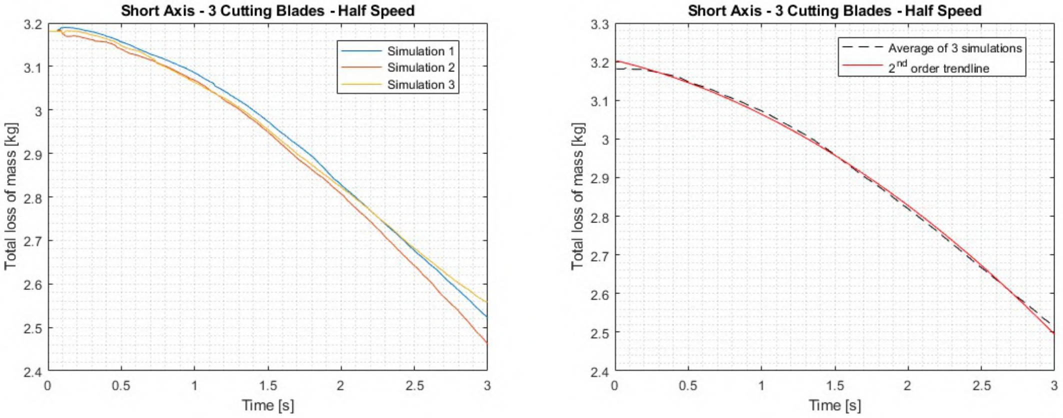

(a) Individual repetitions

(b) Average of three repetitions

Figure 54: Total loss of mass for geometry 4 with half speed

### Determining mass flow rate from total loss of mass

When the derivative of the total loss of mass is taken, the mass flow rate is obtained, as shown in figure 55. The figure illustrates that the mass flow rate increases initially and then stabilizes around an average value. The average mass flow rate here is 0.23 [kg/s]. This corresponds to approximately 55 % of the mass flow rate in the case of rotating at full speed (0.43 [$kg/s$]).

Figure 55: Differentiated mass flow rate for geometry 4 with half speed

### Determining mass flow rate using sensor in EDEM

When a mass flow sensor is used at the bottom exit of geometry 4 operating at half speed, figure 56 is generated. This figure plots the mass flow rate for all three repetitions. Also here, it is evident that as time progresses, the mass flow rate exhibits more outliers and consequently increases further.

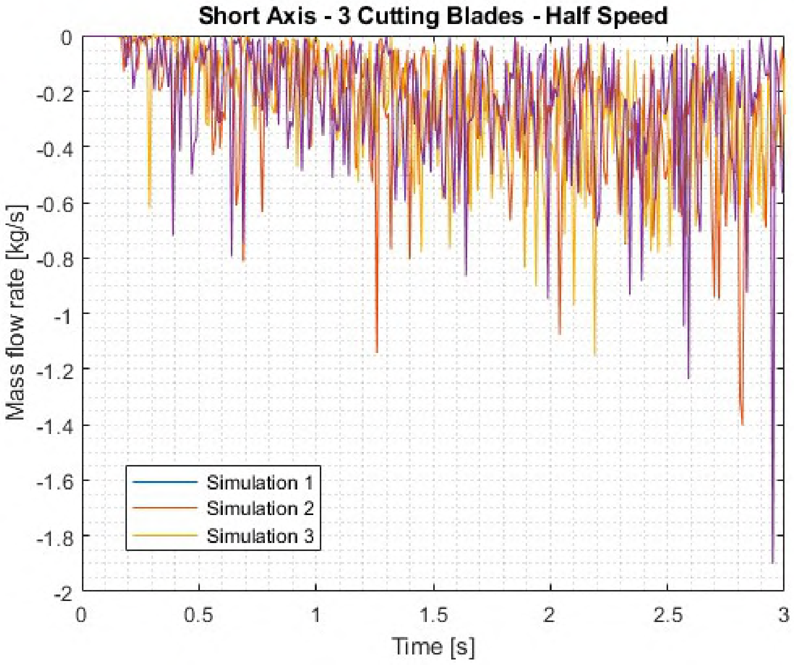

Figure 56: Sensed mass flow rate for individual repetitions for geometry 4 with half speed

Figure 57a shows the average of the three repetitions. When a Savitzky–Golay filter is applied to filter the signal, figure 57b is generated. Similar to figure 50b, it is evident that the mass flow initially increases and then stabilizes around a certain value. However, this decrease is much more gradual than at full speed. This is because at high speeds, more fracture interactions occur, causing particles to become small enough ($< 5$ $[mm]$) to exit the geometry at the bottom more quickly. The values between the derivative from the total loss of mass ($0.23$ $[kg/s]$) and the mass flow rate determined using a sensor ($0.24$ $[kg/s]$) also match well. Again, it is observed that the mass flow at half speed is approximately 55-60 % of the mass flow at full speed.

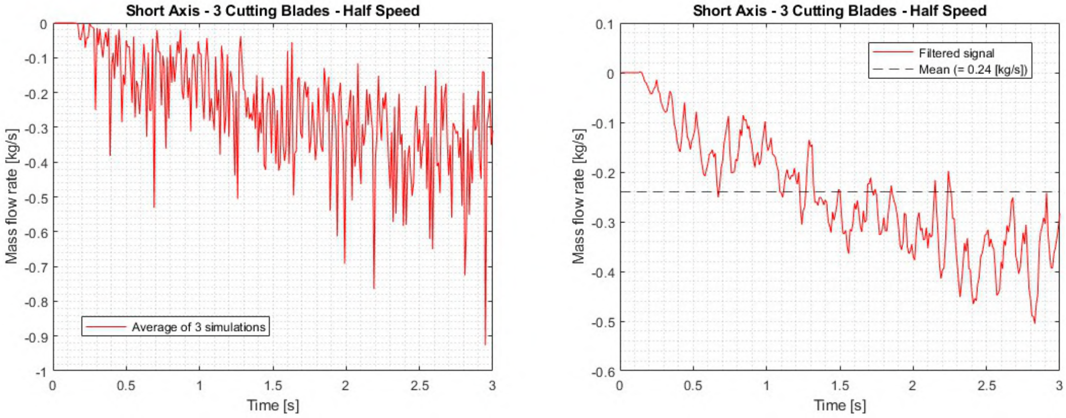

(a) Unfiltered data

(b) Filtered data

Figure 57: Sensed mass flow rate for geometry 4 with half speed

### Comparing particle size distribution at exit

Figure 58 displays the particle size distribution at the exit for geometry 4 at half speed. In contrast to rotating at full speed (figure 51), a stronger exponential trend is observed here for both the total amount of particles generated as well as the amount of dust created. Additionally, it is noticeable that the ratio between the amount of dust relative to the total amount of mass is much higher when rotating at half speed (50.21 %) compared to rotating at full speed (27.49 %).

The reason for this is that when operated at half speed, the granulator does not generate enough centrifugal force to effectively propel the material out of the cutting chamber. As a result, the material will spend more time within the cutting chamber, undergoing repeated cutting actions, leading to increased generation of dust. At full speed, the granulator operates with greater centrifugal force, which can effectively propel the material out of the cutting chamber more rapidly. This rapid expulsion of material results in less time for the material to undergo repeated cutting actions, hence reducing the generation of dust.

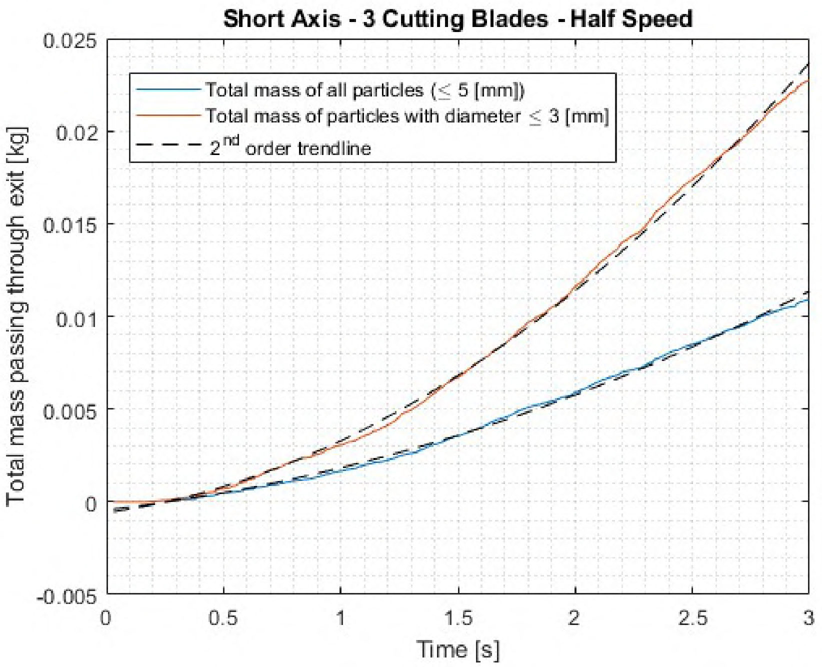

Figure 58: Particle size distribution of exiting material for geometry 4 with half speed

### Comparison between different rotation speeds

Table 7 provides an overall comparison between the different rotation speeds for geometry 4 (Short Axis - 3 Cutting Blades). It is observed that rotating at half the speed results in a mass flow output of 58.5 % compared to rotating at full speed. Furthermore, it can be seen that rotating at half speed leads to almost a doubling of the amount of generated dust. Therefore, it is most efficient to operate the granulator at full speed. Subsequently, the impact of the rotation speed on the power consumption will be examined.

| **Rotation speed** | **Mass flow** $[kg/s]$ | **Amount of particle** $\leq$ **3** $[mm]$ |
|---|---|---|
| Low speed | 0.24 | 50.21 % |
| High speed | 0.41 | 27.49 % |

Table 7: Overall comparison between different rotation speeds

## 6.3 Effect of filling technique on granulating performance

Besides the rotation speed, the way the granulator is being filled can also influence the mass flow rate and the particle size distribution of the output. Therefore, for the best performing geometry (Short Axis - 3 Cutting Blades), the influence of the filling technique is also examined. Two filling methods are chosen: 'simultaneous filling' and 'sequential filling'. The initial scenario involves simultaneous filling of the granulator, meaning two particles are added to the geometry at t = 0 [$s$]. The results of this filling technique have already been described. The scenario in this chapter will explore sequential filling. Here, one particle is added at t = 0 [$s$] and the second particle is added at t = 1.5 [$s$]. Given the proximity of the results from the five different runs in the initial scenario and considering the time required for each simulation, a decision is made to opt for three repetitions in this case as well, similar to the approach taken when assessing the impact of rotation speed.

Figure 59a depicts the total number of particles generated for geometry 4 using sequential filling. Similar to the case of simultaneous filling (figure 46a), the repetitions exhibit close agreement. In the figure, it is evident that at t = 1.5 [$s$], the graph exhibits a bend and begins to steepen. This phenomenon arises due to the addition of an extra particle, allowing for more breaking interactions to occur, consequently increasing the number of generated particles.

Figure 59b displays the average of the three repetitions. In contrast to figure 46b, which exhibits an exponential decrease, in the case of sequential filling, there is an exponential increase. This discrepancy arises due to the addition of an extra particle at a later stage, leading to the formation of new breakage interactions. Interestingly, the total number of generated particles between both simultaneous and sequential filling methods does not differ significantly. One might expect that during simultaneous filling, by adding two particles simultaneously, would allow more time for both particles to undergo breakage interactions, resulting in a considerably larger total number of generated particles compared to sequential filling. However, the values are $1.4 * 10^5$ at t = 3 [$s$] for simultaneous filling and $1.3 * 10^5$ at t = 3 [$s$] for sequential filling and thus do not differ significantly

### Total amount of generated particles

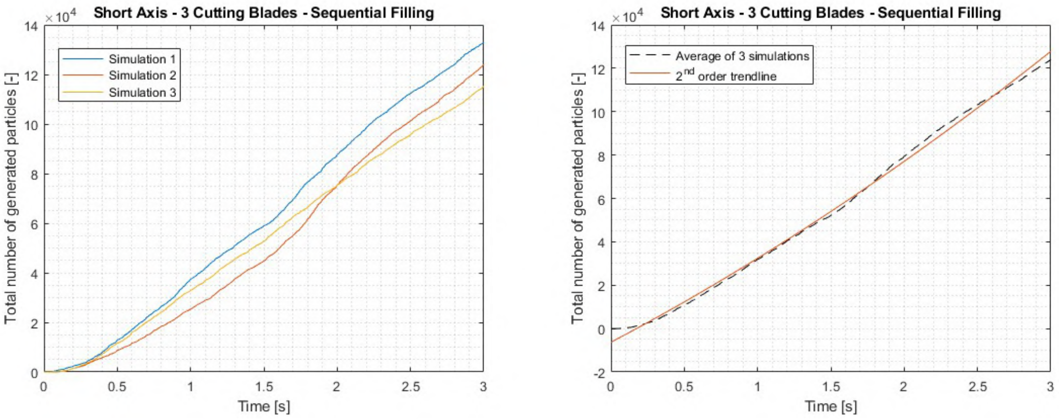

(a) Individual repetitions

(b) Average of three repetitions

Figure 59: Number of generated particles for geometry 4 with sequential filling

### Total loss of mass in system

Figure 60a shows the total loss of mass from geometry 4 when the sequential filling method is used. It is clearly visible that the present mass increases at t = 1.5 [$s$], as a second particle is added to the geometry at this time. Also in this case, it can be seen that the different repetitions overlap well with each other.

Figure 60b depicts the average of the three repetitions. It is notable that the graph exhibits an exponential trend before the second particle is added, and after the second particle is added, the graph follows a linear trend. Furthermore, it can be observed that at the end of the simulation, there is still 2.13 [$kg$] of mass remaining in the system. This is considerably more than in the initial scenario using simultaneous filling (1.93 [$kg$]). This is due to the fact that the second particle is added later, allowing less time for it to be reduced in a size small enough to exit at the bottom of the geometry. It is striking that, unlike the total number of created particles, which is comparable between both filling methods, the total mass present in the system does differ.

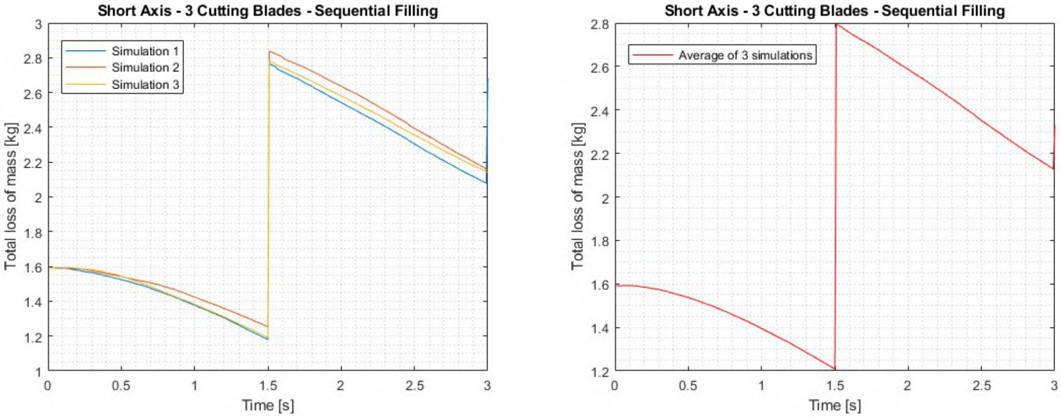

(a) Individual repetitions

(b) Average of three repetitions

Figure 60: Total loss of mass for geometry 4 with sequential filling

### Determining mass flow rate from total loss of mass

Figure 61 represents the total mass flow rate based on the differentiated total amount of mass present in the system. Due to the addition of a particle at t = 1.5 [$s$], a peak is observed here.

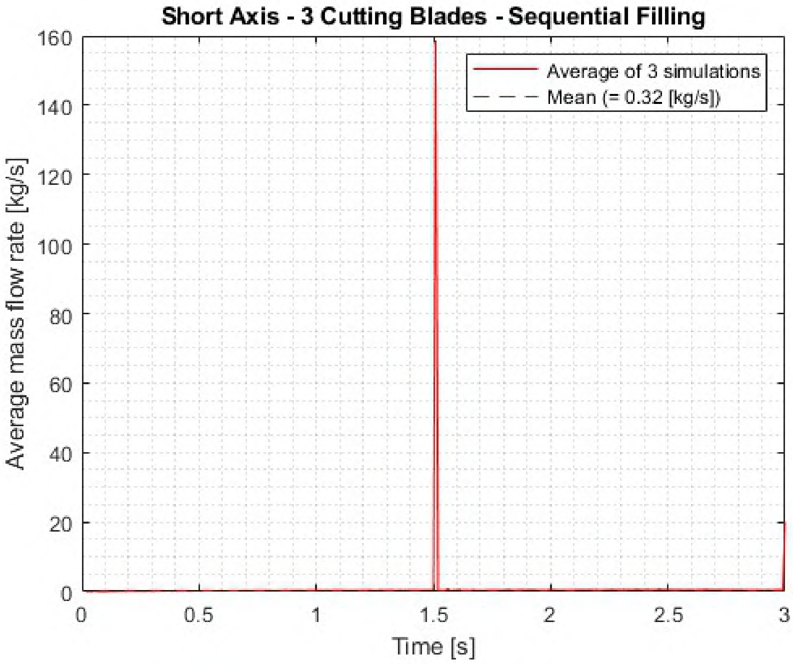

Figure 61: Differentiated mass flow rate for geometry 4 with sequential filling

### Determining mass flow rate using sensor in EDEM

When a mass flow sensor is installed at the outlet at the bottom of geometry 4 using sequential filling, figure 62 is obtained. The mass flow rate fluctuates around an average value for the three repetitions and only has two outliers at t = 0.89 [$s$] and at t = 2.34 [$s$]. The data corresponds to the initial scenario where simultaneous filling occurs (figure 49). Remarkably, in the case of sequential filling, the simulation has fewer outliers, but the outliers are larger. This could be due to various factors, including the accumulation effect of particles in certain parts of the system, larger individual additions of particles, and a possible lack of stabilization of the mass flow during filling.

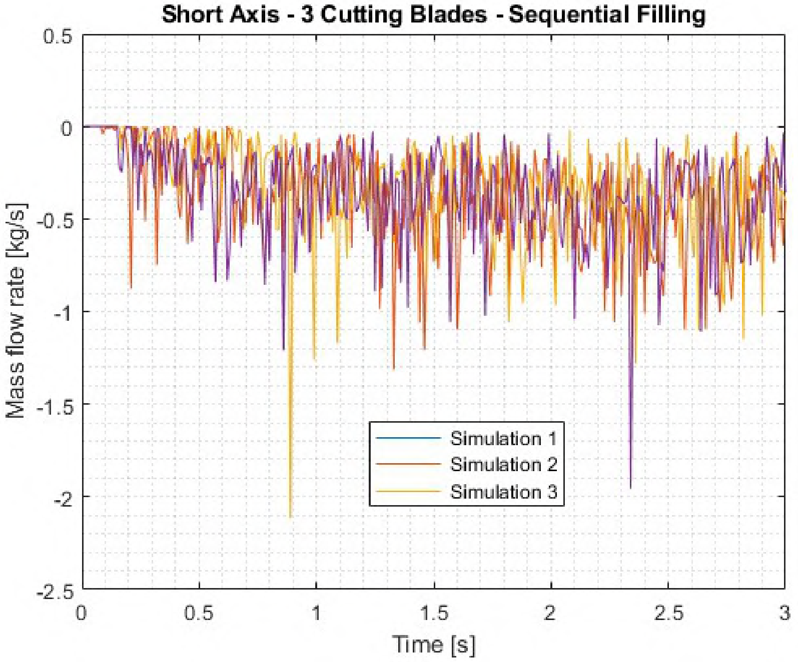

Figure 62: Sensed mass flow rate for individual repetitions for geometry 4 with sequential filling

Figure 63a displays the average of the three repetitions. The signal filtered by a Savitzky-Golay filter is depicted in figure 63b. The figures for both simultaneous filling (figure 50b) and sequential filling exhibit the same trend. A difference is that in the case of simultaneous filling, the figure flattens more quickly before fluctuating around an average value. With sequential filling, it takes longer to reach this steady state. This is because in the case of sequential filling, there is still action occurring after t = 1.5 [$s$], prolonging the time it takes to reach equilibrium. Furthermore, the mass flow rate in the case of simultaneous filling is higher (0.41 [$kg/s$]) compared to sequential filling (0.35 [$kg/s$]). This is also due to the fact that in the case of simultaneous filling, particles have more time to be reduced in size and exit the system, resulting in a higher mass flow rate.

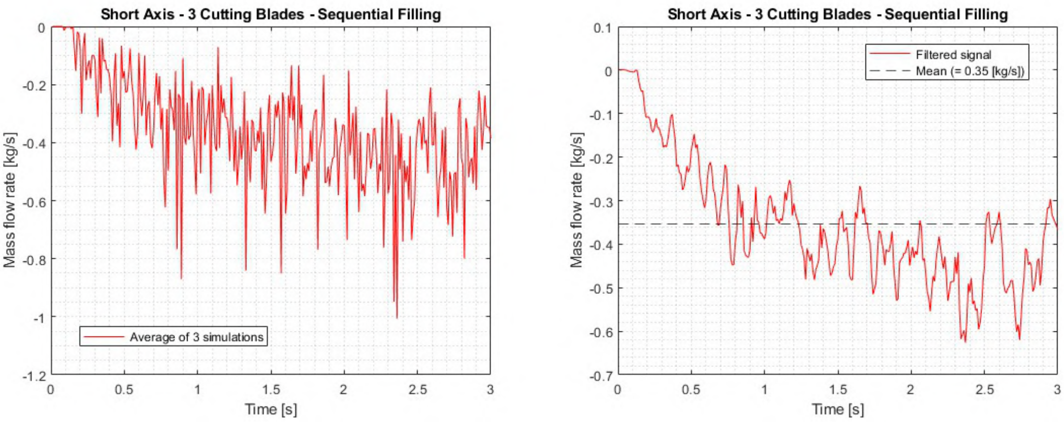

(a) Unfiltered data

(b) Filtered data

Figure 63: Sensed mass flow rate for geometry 4 with sequential filling

### Comparing particle size distribution at exit

Figure 64 illustrates the particle size distribution for geometry 4 with sequential filling. Notably, both the total mass and the mass of the dust exhibit a considerably higher level of instability upon exiting the system compared to simultaneous filling. Additionally, the trajectory of both mass flows appears more exponential than in the initial scenario. The quantity of dust is significantly greater in the case of sequential filling (52.73 %) in contrast to simultaneous filling (27.49 %). One plausible explanation for this discrepancy lies in the simultaneous filling process, wherein all raw materials are introduced simultaneously, potentially fostering a more uniform mixture and thereby mitigating dust formation, as opposed to sequential filling, which involves the incremental addition of raw materials.

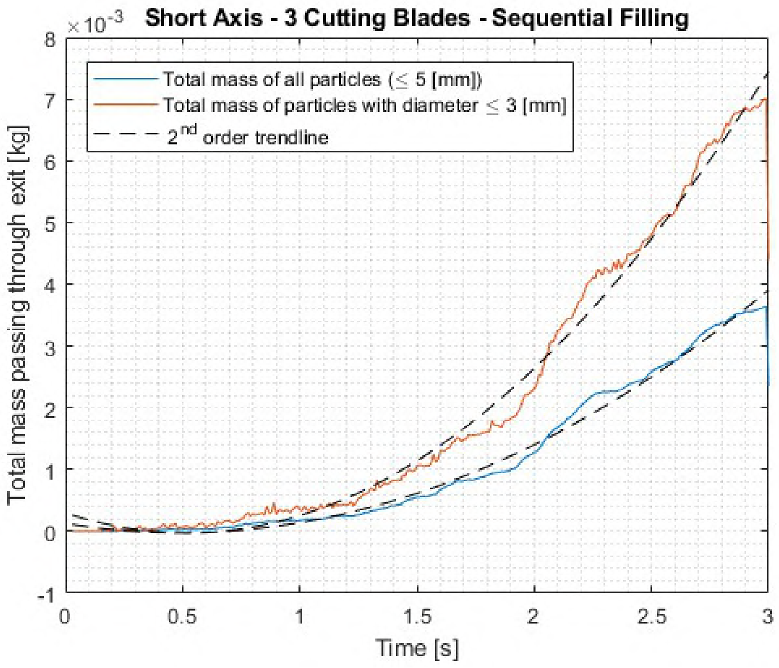

Figure 64: Particle size distribution of exiting material for geometry 4 with sequential filling

## 6.4 Overall comparison

### 6.4.1 Comparison between amount of particles generated for all geometries

Figure 65 provides an overview comparing the amount of generated particles across different geometries. It is clear from the figure that the majority of particles are produced in a geometry with a short axis and 3 cutting blades. On the other hand, a configuration with a long axis and three cutting blades yields the lowest number of generated particles.

Moreover, the length of the axis has a more significant impact on particle generation compared to the number of cutting blades. In general, when the axis is longer, the number of cutting blades has less influence on particle generation.

Overall, it can be concluded that a shorter length of the axis results in more particles being generated. For instance, the number of particles produced with a long axis and three cutting blades is only 29 % compared to a short axis with 3 cutting blades. Conversely, a short axis with two cutting blades produces 73 % of the particles compared to a short axis with three cutting blades. Additionally, a long axis with three cutting blades generates 90 % of the particles compared to a long axis with two cutting blades.

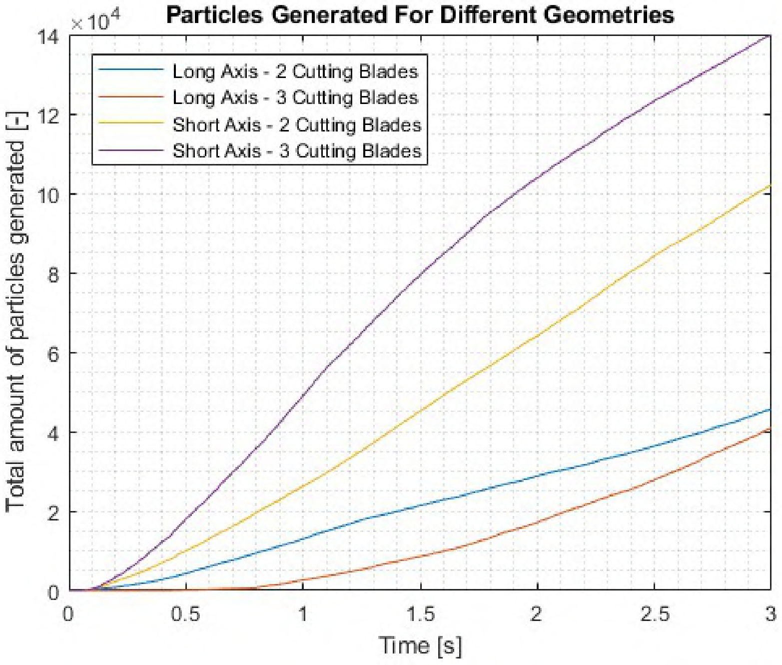

Figure 65: Total amount of particles generated for all geometries

### 6.4.2 Comparison between loss of mass for all geometries

The same observation holds true for the total loss of mass in the system. Here as well, the length of the axis proves to be more influential than the number of cutting blades. Similarly, the geometry with the short axis and three cutting blades demonstrates the best performance, while the geometry with the long axis and three cutting blades exhibits the poorest performance. This latter configuration only loses 31 % of its mass compared to the best-performing geometry.

Relative to the geometry with a long axis and two cutting blades, the geometry with a long axis and three cutting blades generates 76 % of the particles. Furthermore, the geometry with a short axis and two cutting blades produces 81 % of the particles compared to the short axis with three cutting blades. It is noteworthy that a long axis combined with three cutting blades results in a smaller quantity of generated particles and a lower mass flow out of the system compared to a long shaft combined with two cutting blades. However, in the case of a short axis, both the total quantity of generated particles and the mass flow rate out of the system increase more rapidly when using 3 cutting blades compared to 2 cutting blades.

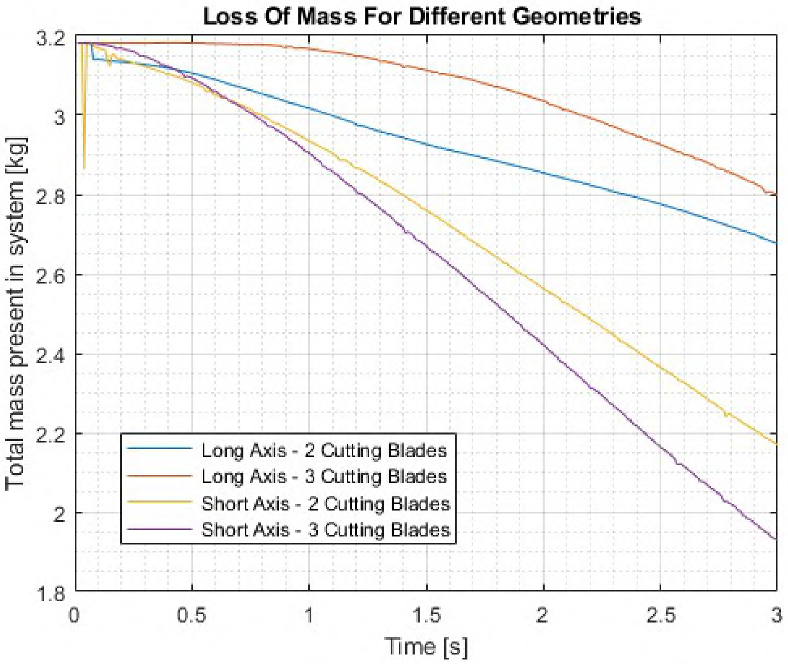

Figure 66: Total mass present in system for all geometries

## 6.5 Effect of operational parameters on granulating performance

### 6.5.1 Effect of rotational speed on total amount of particles generated

The impact of the rotation speed of the axis associated with geometry 4 can be observed in figure 67. It is clearly visible that an increase in rotation speed also leads to a greater number of generated particles. From the figure, it can be seen that halving the rotation speed results in the production of 63 % of the particles compared to full speed. It is striking that when the rotation speed is halved, the increase in the number of particles occurs approximately linearly. In contrast, at full speed, there is an exponential decrease.

The reason for both phenomena is that with a higher rotation speed of the granulator, the impact force on the input materials will be greater. This results in a more effective reduction of the materials and thus a greater production of particles. Therefore, the increase in rotation speed leads to a direct increase in the number of produced particles.

When the rotation speed is halved, the impact force of the granulator on the materials will significantly decrease. Consequently, the reduction of the materials will be less efficient, leading to a decrease in the number of produced particles. The effect of halving the rotation speed can thus be observed as a proportional decrease in the number of produced particles.

The difference in the relationship between rotation speed and particle production at full speed and halved speed can be explained by the complexity of the reduction process. At full speed, other factors such as material properties and machine design may also play a role in determining particle production, resulting in a more complex, non-linear relationship between rotation speed and production.

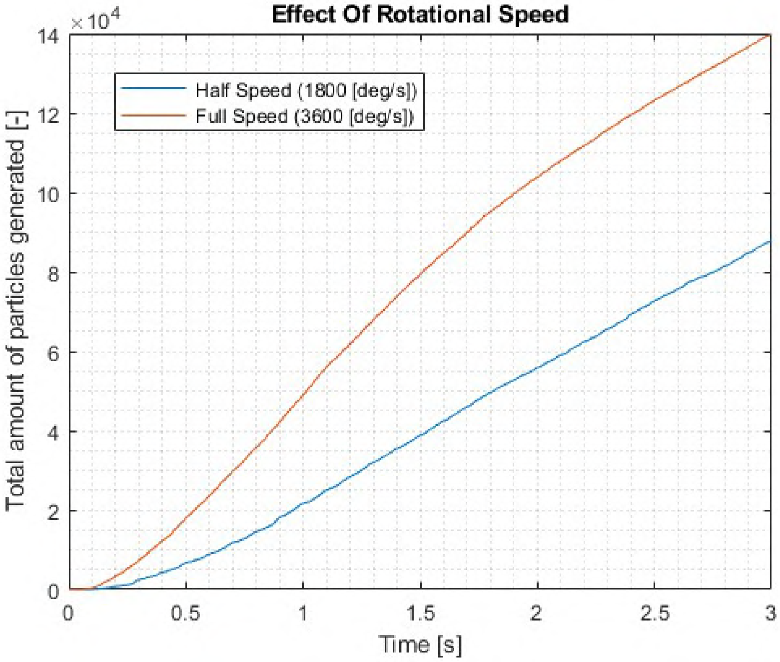

Figure 67: Total amount of particles generated - different speeds

### 6.5.2 Effect of rotational speed on mass flow rate

Apart from the number of generated particles, it is also interesting to examine the difference in output when a mass flow sensor is used at the geometry's outlet. Figure **??** displays the mass flow rate for both half speed and full speed of geometry 4 (Short Axis - 3 Cutting Blades). It is evident that the mass flow rate increases over time for both speeds. The mass flow stabilizes earlier at high rotation speeds than at lower rotation speeds. Furthermore, it is observed that the mass flow profile at half speed exhibits a more linear trend, while at full speed, it demonstrates a more exponential trend.

The reason behind this lies in the fact that at higher rotation speeds, the granulator possesses more kinetic energy, resulting in a more powerful impact on the input materials. This vigorous impact accelerates the reduction of materials, leading particles to reach the desired size sooner. Consequently, the mass flow stabilizes faster since less time is required to reduce a certain amount of material to the desired size. At half speed, the relationship between rotation speed and material reduction may be more linear because the impact force of the granulator on the materials decreases proportionally with the rotation speed, resulting in a more gradual reduction of materials and a linear trend in the mass flow. It is notable that the average mass flow rate at half speed is approximately 59 % compared to full speed.

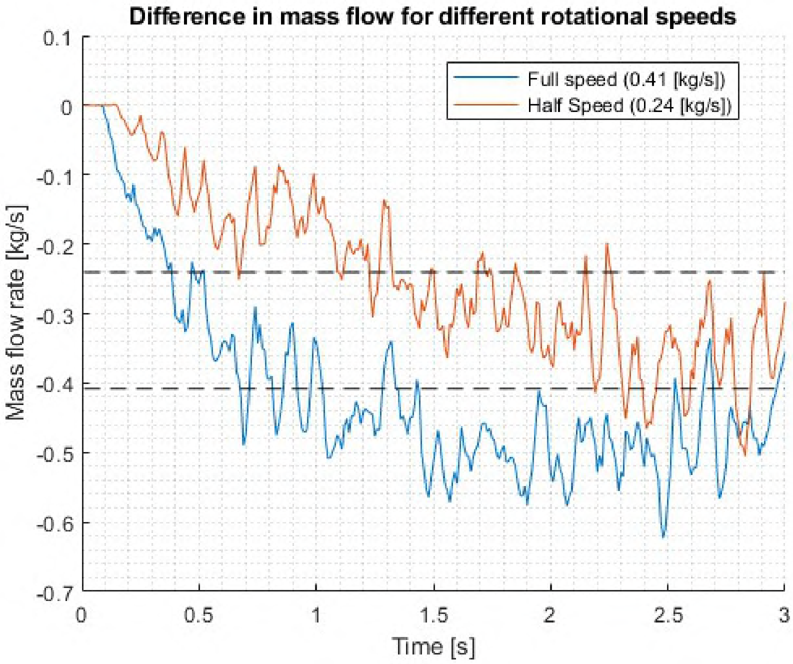

Figure 68: Mass flow rate for different rotation speeds

### Effect of rotational speed on particle size distribution at exit

Table 8 presents both the mass flow rate and the amount of produced dust for both speeds. It is noteworthy that at high speed, not only does the mass flow increase, but also the amount of produced dust decreases. For instance, the amount of produced dust at full speed is approximately 55 % compared to rotating the granulator at half speed.

This phenomenon can be explained by the following arguments:

- **Efficient Particle Size Reduction**: higher speeds result in greater kinetic energy, leading to more effective fragmentation of material into larger particles, reducing the generation of fine dust.
- **Material Agglomeration**: increased forces at higher speeds encourage particle compaction and agglomeration, minimizing the formation of fine dust particles.
- **Reduced Attrition**: higher speeds decrease the likelihood of particle-to-particle collisions, reducing dust generation through attrition

| **Rotation speed** | **Mass flow** $[kg/s]$ | **Amount of particle** $\leq$ **3** $[mm]$ |
|---|---|---|
| Half Speed | 0.24 | 50.21 % |
| Full Speed | 0.41 | 27.49 % |

Table 8: Overall comparison between different rotation speeds for geometry 4

### Effect of rotational speed on power consumption

In the paragraphs above, it has been described that a high rotation speed results in an increase in capacity of 171 % and a decrease in the amount of dust generated of 183 % compared to a rotation on half speed. However, a high rotation speed is also accompanied by a higher energy consumption. To determine the power consumption, the following formula has been used:

$$P = T * \omega \tag{82}$$

$P$ = power $[W]$
$T$ = torque $[Nm]$
$\omega$ = angular velocity $[1/s]$

Using EDEM, initially, the torque exerted on the rotating axis is determined. Figure 69a depicts the torque over time for an axis rotating at half speed, while figure 69b illustrates the torque over time for an axis rotating at full speed. In both cases, it can be observed that the torque rapidly increases and begins to fluctuate around an average value. Interestingly, the torque remains more or less constant in the case of full speed, whereas it exhibits a slight increase at half speed. An explanation for this phenomenon is the fact that torque remains more constant at full speed due to the more efficient and uniform processing of the material, while at half speed, there may be more variability in the process, resulting in a slight increase in torque.

From figure 69, it is evident that the average torque value for an axis rotating at half speed is 28284 $[Nm]$. Conversely, for an axis rotating at full speed, the average torque value is 21856 $[Nm]$. This indicates that an axis rotating at a lower speed has a higher torque. The torque exerted on an axis rotating at full speed is 77 % of the torque exerted on an axis rotating at half speed. The reason for this phenomenon is the fact that rotating at lower speeds causes reduced kinetic energy and impact forces, resulting in more resistance during the process.

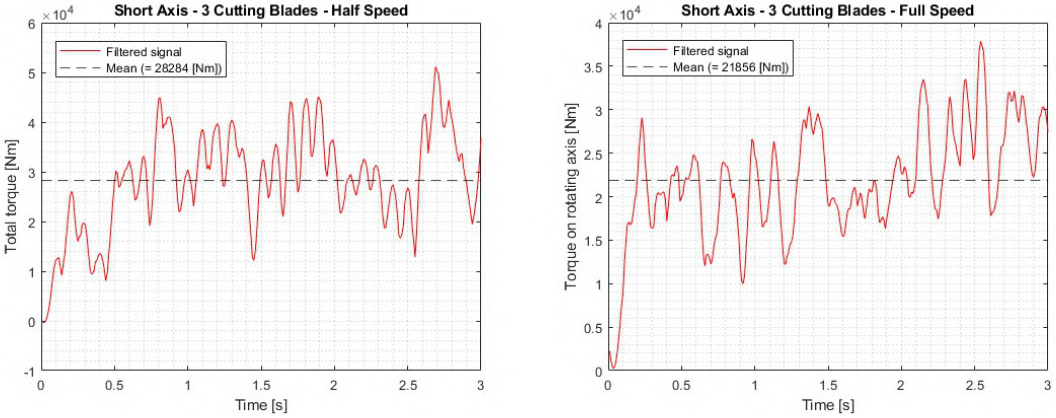

(a) Torque at half speed

(b) Torque at full speed

Figure 69: Comparison of required torque for different rotation speeds

The total power draw is not only dependent on the torque but also on the rotation speed. Figure 70 provides the power draw for both rotation speeds, calculated using equation 82. It can be observed that the power draws for both speeds fluctuate around an average value. The power draw at half speed remains more or less constant, while the power draw at full speed shows a slight increase. From the figure, the average power draw is found to be $8.9 * 10^5$ $(W)$ at half speed and $1.3 * 10^6$ $(W)$ at full speed. In other words, the energy consumption at half speed is approximately 68 % compared to full speed.

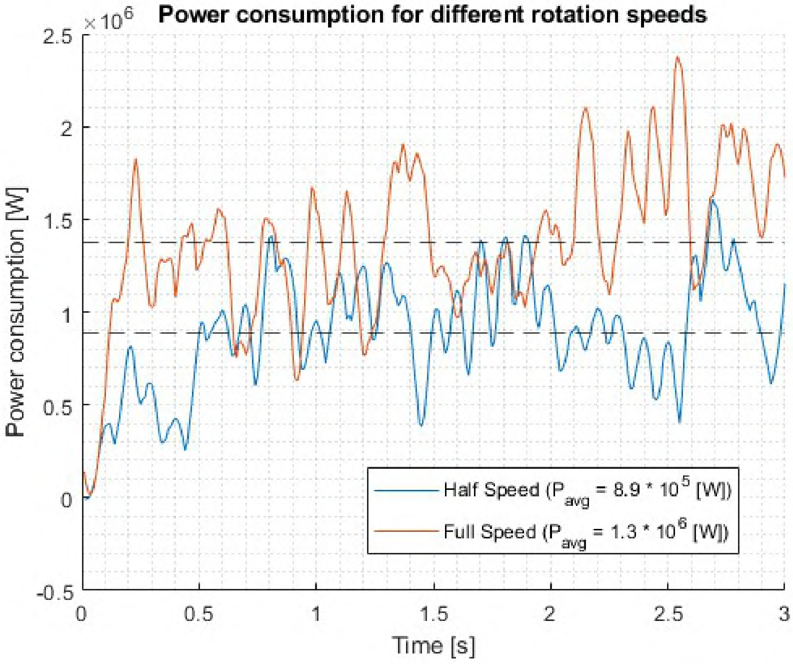

Figure 70: Total power consumption - different speeds

It has been shown that rotating at full speed results in approximately halving the amount of created dust compared to rotating at half speed. Now, it is also evident that the power consumption at half speed is not halved compared to the power consumption at full speed. In other words, for a mass flow of 59 % compared to rotation at full speed, 68 % of the energy is consumed compared to rotation at full speed. This implies that rotating at full speed not only yields higher output and better material properties but is also more energy-efficient compared to rotating at half speed.

### 6.5.3 Effect of filling principle on total amount of particles generated

The effect of the filling mechanism on the amount of particles generated for geometry 4 (Short Axis - 3 Cutting Blades) can be observed in figure 71. As described earlier, simulations were conducted for two filling techniques: simultaneous filling and sequential filling. In the figure, it can be seen that the number of generated particles increases more rapidly using simultaneous filling compared to sequential filling. This is logical because more mass is added at t = 0 [$s$].

When the second particle is added at t = 1.5 [$s$] using sequential filling, it can be observed that the number of generated particles increases, whereas for simultaneous filling, it decreases. Consequently, the graphs start to converge. Since the simulation was only conducted for 3 seconds, no statement can be made about the efficiency of the filling technique on the long term. However, a statement can be made about the efficiency on the short term.

In the figure, it can be seen that when using sequential filling, the number of generated particles after 3 seconds is 89 % compared to simultaneous filling. Therefore, the simultaneous filling technique is more efficient on the short term compared to the sequential filling technique. However, it is evident that the filling technique has less influence on the amount of particles generated compared to the rotation speed.

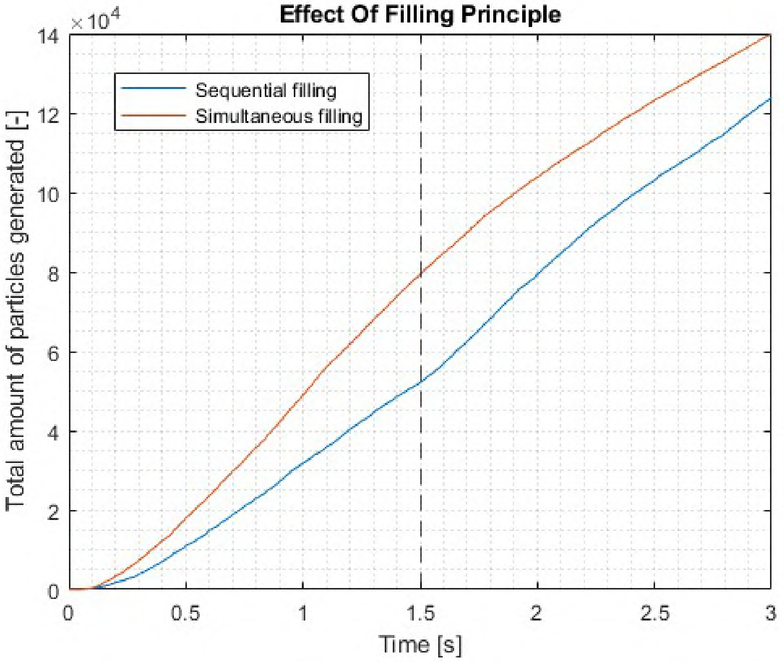

Figure 71: Total amount of particles generated - different filling techniques

### 6.5.4 Effect of filling principle on mass flow rate

More important than the number of generated particles is the speed at which the particles exit the geometry. Figure 72 illustrates the mass flow rate at the output of the geometry for both filling techniques. Both lines follow the same trend, initially decreasing and then stabilizing around a more or less constant value. The average mass flow rate is 0.41 [kg/s] for simultaneous filling and 0.35 [kg/s] for sequential filling. In other words, the mass flow rate using sequential filling is 85 % compared to simultaneous filling. This also indicates that the filling technique is less influential compared to the rotation speed.

Interestingly, at the beginning of the simulation, the mass flow rates for both simultaneous filling and sequential filling are approximately equal. This is despite only 50 % of the mass being present in the system for sequential filling compared to simultaneous filling. This suggests that factors other than the total mass contribute to the initial mass flow rates, such as the distribution and movement of particles in the system.

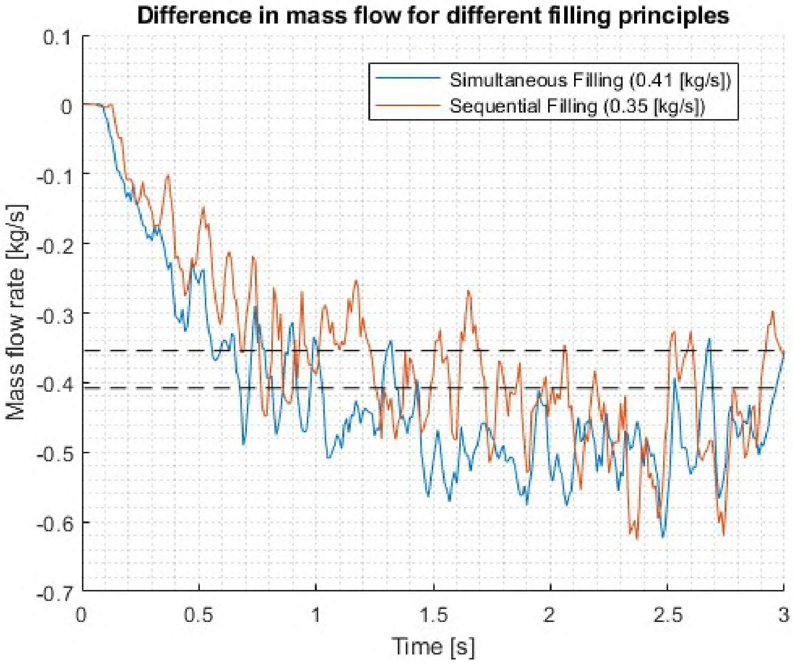

Figure 72: Mass flow rate for different filling principles

Apart from the mass flow rate, it is also important to examine the difference in particle size distribution of the output for both filling techniques. Table 9 presents the mass flow rate and the percentage of dust for geometry 4 (Short Axis - 3 Cutting Blades), comparing both simultaneous filling and sequential filling. It is evident that simultaneous filling is favored. Not only is the mass flow rate higher in this scenario, but the percentage of generated dust is also slightly more than half compared to the scenario involving sequential filling.

| **Filling method** | **Mass flow** $[kg/s]$ | **Amount of particle** $\leq$ **3** $[mm]$ |
|---|---|---|
| Simultaneous | 0.41 | 27.49 % |
| Sequential | 0.35 | 52.73 % |

Table 9: Overall comparison between different rotation speeds

# 7 Conclusion

In this study, the optimization of the granulator's performance at GreenCycl's recycling plant has been investigated through a comprehensive analysis of various operational and geometrical parameters. By addressing the five sub-research questions, a profound understanding of the factors influencing granulation performance and product quality has been achieved.

Beginning with an exploration of particle breakage mechanisms, it became evident that both loading and breakage mechanisms play pivotal roles. Material properties, geometric characteristics and environmental factors were identified as influential factors governing particle breakage behavior.

Subsequently, the investigation delved into crucial parameters in the design of comminution equipment. Geometric and operational parameters, such as axis length and the number of cutting blades, were found to significantly impact output and the generation of dust particles.

Implementation of an advanced particle breakage model facilitated simulation of breakage behavior, with consideration given to various calibration methods. Ultimately, calibration against experimental data provided a robust foundation for accurate simulation outcomes.

The focal point of this research lays in the analysis of operational and geometrical parameters' influence on granulator output. Findings revealed that employing a shorter axis with three cutting blades yielded the highest output, albeit with an increased dust generation. Moreover, higher rotation speeds and simultaneous filling improved output and reduced dust generation, leading to a more efficient process.

These findings bear critical importance for GreenCycl B.V., empowering the organisation to implement targeted enhancements in the granulation process to maximize output and enhance product quality. This research lays a solid groundwork for further optimization endeavors, contributing to the growth and sustainability of GreenCycl's recycling operations.

In conclusion, this study not only provides valuable insights into granulation optimization but also underscores the significance of considering operational and geometrical parameters in process enhancement strategies. As GreenCycl B.V. continues its mission towards sustainable recycling practices, the findings presented in this thesis will serve as a guiding light towards achieving operational excellence and environmental stewardship.

# 8 Recommendations

This chapter is divided into three parts. Firstly, the limitations of the research will be mentioned. Based on this, in the second part, recommendations for GreenCycl B.V. will be outlined to optimize the process based on this research. Thirdly, shortcomings of this study and recommendations for future research will be provided.

## 8.1 Limitations of the Research

The research presented provides valuable insights into optimizing granulator performance at GreenCycl B.V.'s recycling plant, yet it also has several limitations that should be considered:

- **Limited Scope of Operational Parameters**: this study primarily focused on rotation speed and filling technique as the key operational parameters affecting granulator performance. Other potentially influential parameters, such as feed rate and moisture content, were not explored. This limited scope may have overlooked other critical factors that could impact output and dust generation.

- **Simplified Geometrical Assumptions**: the research employed a simplified granulator geometry to reduce simulation time. While this approach facilitated quicker analysis, it may not fully capture the complexities of real-world granulator designs. The simplifications in geometry could lead to discrepancies between simulated and actual granulator performance.

- **High Gravitational Force in Simulations**: to prevent undamped movements of particles, the study applied a gravitational force 100 times higher than Earth's gravity. This artificial condition could introduce biases in the results, as it does not accurately reflect the actual forces experienced by particles in the granulator.

- **Estimation of Breakage Parameters for Polypropylene**: the breakage parameters for Tavares' breakage model are well-defined for minerals but not for polypropylene, which was the focus of this study. The research relied on estimated values for polypropylene, which may not be precise. Experimental determination of these parameters is necessary for more accurate simulations.

- **Short Simulation Times and High Rotation Speeds**: the study increased rotation speeds and used short simulation times to better observe breakage effects. While this approach provided quicker insights, it might not accurately reflect the granulator's behavior under normal operating conditions. Longer simulation times and lower rotation speeds could yield different results.

- **Standard Coefficients of Restitution and Friction**: the research used standard values for the coefficients of restitution, static friction, and rolling friction in simulations. These values may not accurately reflect the actual interactions between particles and between particles and granulator walls. More precise approximations of these coefficients are needed for realistic simulations.

- **Technical Challenges with Non-Spherical Particles**: applying Tavares' breakage model to non-spherical particles is currently technically challenging and requires significant computational resources. The inability to accurately model non-spherical particles limits the applicability of the findings to more complex and realistic scenarios.

- **Generalizability to Different Materials**: while the research focused on polypropylene, the findings may not be directly applicable to other materials with different physical and mechanical properties. Further research is needed to validate the conclusions for a broader range of materials used in recycling processes.

## 8.2 Recommendations for GreenCycl B.V.

Based on the findings of this research, several recommendations can be proposed to optimize the performance of the granulator at GreenCycl's recycling plant:

- **Adopt Optimal Geometrical Configurations**: implement a granulator design with a shorter shaft and three cutting blades to maximize output while neglecting dust generation. This configuration demonstrated the highest output in the analysis, albeit with a significant increase in dust production. By leveraging this design, GreenCycl B.V. can enhance productivity.

- **Optimize Operational Parameters**: fine-tune operational parameters such as rotation speed and filling technique to further enhance granulator performance. Increasing rotation speeds and adopting simultaneous filling strategies have been shown to improve output and reduce dust generation. GreenCycl B.V. should explore these adjustments to maximize efficiency and minimize environmental impact.

- **Continuous Monitoring and Adjustment**: establish a system for continuous monitoring of granulator performance and dust emissions. Regularly assess the effectiveness of operational and geometrical parameters in achieving desired output and dust control targets. Adjustments should be made as necessary to maintain optimal performance and compliance with environmental regulations.

- **Invest in Advanced Modeling and Simulation**: continue investing in advanced particle breakage modeling and simulation tools to refine granulator design and operational strategies. These tools enable predictive analysis of granulation dynamics, facilitating informed decision-making and optimization efforts. Calibration against experimental data should be an ongoing process to ensure the accuracy and reliability of simulation outcomes.

- **Promote Sustainability and Environmental Stewardship**: emphasize sustainability and environmental stewardship in all aspects of granulator operation and maintenance. Implement dust mitigation measures and pollution control technologies to minimize environmental impact. Additionally, explore opportunities for resource recovery and waste minimization to further enhance the sustainability of GreenCycl's recycling operations.

By implementing these recommendations, GreenCycl B.V. can optimize the performance of its granulator and position itself as a leader in sustainable recycling practices. Continual improvement and innovation are essential in achieving operational excellence and environmental stewardship in the recycling industry.

## 8.3 Recommendations for future research

- **Investigate Additional Operational Parameters**: while this study focused on rotation speed and filling technique as key operational parameters, future research could explore the influence of other operational variables, such as feed rate and moisture content, on granulator performance. By comprehensively assessing a broader range of operational parameters, a more nuanced understanding of their impact on output and dust generation can be obtained.
- **Incorporate Real-Time Monitoring and Control Systems**: the current study relied on simulation and experimental data to evaluate granulator performance. Future research could explore the implementation of real-time monitoring and control systems within the granulator to enable continuous optimization and adaptive control. This would provide valuable insights into dynamic process behavior and facilitate responsive adjustments to operational conditions.
- **Enhance Particle Breakage Modeling**: while the study employed advanced particle breakage models, such as Tavares' novel particle breakage model, there remains scope for further refinement and validation of these models. It is worth noting that for this study, a gravitational force 100 times higher than Earth's gravity was applied to prevent particles from making undamped movements. However, there is a need to develop improved strategies to handle particle damping forces more effectively. Additionally, it is important to acknowledge that the breakage parameters for Tavares' breakage model are currently only determined for minerals. During this research, an estimation of these values for polypropylene was made. Future research should conduct experiments to accurately determine these values through particle size distribution experiments to enhance the precision of simulations.
- **Address Uncertainties and Variability**: the study acknowledged the inherent uncertainties and variability associated with granulation processes. It is important to highlight that the rotation speed was increased in this study to better observe breakage effects within the short simulation time. Subsequent research could investigate breakage effects at lower rotation speeds and longer simulation times to capture a more comprehensive understanding of granulator behavior. Additionally, the study opted for a simplified geometry to reduce simulation time. Future research could explore retaining more details in the granulator geometry and investigate the effects on granulator performance. Furthermore, there is potential to examine the effects on the granulator itself through Discrete Element Method - Multi-Body Dynamics Co-simulations. Previous studies by R.J.P. Dekker have explored applications of this approach in other contexts, suggesting its relevance for granulator analysis.
- **Refine Coefficients of Restitution and Friction Parameters**: finally, it is worth noting that in the simulation, standard values for the coefficient of restitution, the coefficient of static friction, and the coefficient of rolling friction were used. In future research, more accurate approximations for these coefficients could be selected. These coefficients play a crucial role in determining the interactions between particles and between particles and the granulator walls. Better approximations of these coefficients could lead to more realistic simulation results, as they directly influence particle behavior, including bouncing, sliding, and rolling. Therefore, exploring methods to accurately determine and incorporate these coefficients into simulations is paramount for enhancing the fidelity and predictive capabilities of granulation models.
- **Promote Sustainability and Environmental Stewardship**: emphasize sustainability and environmental stewardship in all aspects of granulator operation and maintenance. Implement dust mitigation measures and pollution control technologies to minimize environmental impact. Additionally, explore opportunities for resource recovery and waste minimization to further enhance the sustainability of GreenCycl's recycling operations.

By addressing these recommendations, future research endeavors can further refine the simulation models and provide a more accurate representation of granulator behavior, ultimately contributing to the advancement of granulation optimization efforts in recycling operations.

### The use of spherical particles in Tavares' breakage model

Lastly, there is another significant shortcoming that needs to be addressed in this research and in Tavares' breakage model, requiring further investigation.

The research chose spherical particles due to their simple geometry and symmetry, which simplifies modeling and simulation. Spherical particles have uniform properties in all directions, making it easier to predict their behavior in simulations. Additionally, well-developed models and algorithms are available for predicting the behavior of spherical particles in various conditions.

Applying Tavares' breakage model to non-spherical particles in simulations like EDEM is challenging. This is because forces can no longer be evenly distributed over the particle's surface, as is the case with spherical particles. This introduces complexity in calculating forces and interactions between the non-spherical particles.

The lack of proportional force distribution over non-spherical particles can result in extremely high computational times when using models like Tavares' breakage model. This is because the software needs to perform detailed calculations to accurately model the complex force distribution over the particles. This increase in computation time can significantly slow down simulations and increase the required computational power, making it practically infeasible for many applications.

Although theoretically possible, applying Tavares' breakage model to non-spherical particles in EDEM is currently technically challenging and will take some time to become feasible due to the complexity and required optimizations in the software.

# Parametric analysis of comminution equipment - A DEM study

**R.J.P. Dekker**[1,✉]

[1] Faculty of Mechanical Engineering, Track Multi-Machine Engineering (MME), Delft University of Technology, Mekelweg 2, 2628CD Delft

**This research examines the performance of a granulator at GreenCycl B.V., focusing on both geometrical and operational parameters that affect particle breakage. Using the discrete element method (DEM) and Tavares' breakage model, simulations are conducted to study four different blade configurations. Based on the value and the particle size distribution of the output, the Short Axis - 3 Cutting Blades design was found to give the highest material output. Additionally, the study assessed the impact of rotation speed and filling techniques, concluding that a high rotation speed with simultaneous filling optimizes results despite higher power consumption. It has been demonstrated that utilizing a short axis relative to a long axis can result in an increase in mass flow rate by a factor of 3.4, accompanied by an increase in dust generation by a factor of 1.2. Furthermore, doubling the rotational speed leads to an increase in mass flow rate by a factor of 1.7, and sequential filling results in an increase in generated dust by a factor of 1.9 compared to simultaneous filling.**

**The study not only enhances the understanding of granulator dynamics but also provides practical recommendations for improving operational efficiency (i.e. high outputs with desired particle size distributions). By identifying optimal configurations and operational settings, GreenCycl B.V. can achieve higher productivity and better control over the particle size distribution, ultimately leading to a more efficient and cost-effective granulation process.**

**DEM | PP | PET | Comminution | Particle simulation | Granular behavior**

**Correspondence:** ***R.P.Dekker@student.tudelft.nl***

## Introduction

Addressing growing waste streams is crucial as raw materials become scarce and climate impacts worsen. Waste is categorized into post-consumer, industrial, agricultural, and hazardous waste, which all have different processing methods. Recycling rates are rising globally; in the Netherlands, plastic packaging is already routinely separated from residual waste for recycling. However, achieving a fully circular economy is challenging, especially considering hazardous waste, which is often incinerated, generating greenhouse gases. Hospitals, major producers of hazardous waste, contribute significantly to CO2-emissions due to their use of single-use medical disposables. A considerable part of this waste, even uncontaminated, is currently incinerated. Better separation could therefore increase recycling capacities. [1]

The GreenCycl Fieldlab has been established as a collaboration between Van Straten Medical and Delft University of Technology to conduct research on the recyclability of various medical waste streams. Urban mining, reclaiming materials from waste, offers a sustainable solution, particularly using hospital waste. Polypropylene (PP) medical wrapping paper, often incinerated despite being uncontaminated, is a significant waste stream. GreenCycl B.V. recycles medical wrapping papers into new products and is now expanding its operations to recycle PET-packaging, which saves energy as it can be granulated directly. This research paper explores optimizing granulators to improve efficiency and granulate quality using DEM simulations in combination with a novel particle breakage model.

## Problem definition

Recycling is a process that is becoming increasingly crucial for sustainability, conserving energy, reducing pollution, and preserving natural resources. However, it is also a costly process requiring a substantial amount of energy. Furthermore, the properties of the end product may differ compared to virgin material. Research is needed to minimize energy input while maximizing product quality. In GreenCycl's recycling facility, melting and comminution are key steps.

A major challenge lies in the comminution of recycled materials. The current Moditec Goliath Plus granulator struggles to efficiently process PP- and PET-packages due to their size and geometry. The granulator's blades tend to make only one cut, leading to a steady state where material becomes stuck, causing blockages (figure 1). To achieve desired granulate quality, it is crucial to optimize the granulator's efficiency by studying different geometries and operational parameters. The Discrete Element Method (DEM) allows for in-depth analysis, reducing the need for physical experiments. Parametric analysis and novel particle breakage models integrated into EDEM can simulate optimal granulator usage, facilitating scalability and moving towards a fully circular economy.

The research aims to gain insights and make recommendations to increase the performance of the granulator at GreenCycl B.V. by identifying key geometrical and operational parameters in comminution equipment and by implementing Tavares' Breakage Model in EDEM (figure 2).

**Fig. 1.** Granulator steady-state

## Research questions

Main Research Question:

- How to improve the granulating performance of polypropylene blocks at GreenCycl's recycling plant by analyzing comminution interactions using the Discrete Element Method (DEM)?

Sub-Questions:

- What factors influence particle breakage?
- What are the critical parameters in comminution equipment design?
- How can particle breakage models enhance comminution simulations?
- How can particle breakage be integrated into granulator interactions?

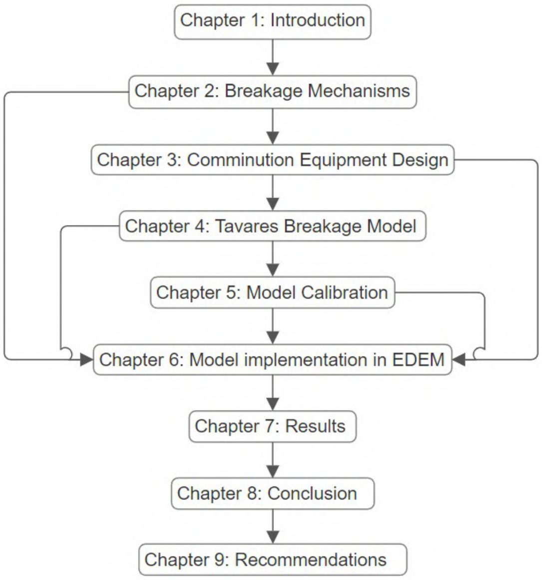

**Fig. 2.** Research flowchart

## Factors influencing particle breakage

The design of comminution equipment is crucial for reducing solid materials' particle size, vital across various industrial sectors like mineral ore processing and recycling. This process, known as 'comminution', separates valuable metals from waste rocks in ore processing and enables injection molding in recycling by reducing product size. Comminution also enhances processing efficiency by mechanically separating different materials.

Materials exist in crystalline or amorphous structures, with crystalline substances featuring ordered arrangements within a lattice. Under load, materials store potential energy until micro-cracks form, leading to material failure. Fracture mechanics classify materials as brittle or ductile based on crack propagation behavior, with brittle materials experiencing rapid crack propagation and ductile materials deforming before fracturing.

Comminution processes are energy-intensive, constituting a significant portion of energy consumption, especially in mining. Optimizing comminution performance is essential to minimize energy consumption and costs. Research focuses on enhancing efficiency from material and energy consumption perspectives.

Particle breakage results from loading mechanisms such as compression, shear, impact, and strike, inducing shattering, cleavage, or abrasion. Breakage behavior is influenced by factors such as particle size, particle shape, ore texture, loading mechanism intensity, temperature, and pre-treatment. While breakage behavior is believed to depend on ore texture, the applied load and pre-treatment may also play roles, though lacking scientific explanation.

## Important comminution design parameters

There are several key elements in the design of comminution equipment, essential for particle size reduction in industries such as mineral ore processing and recycling. There are various comminution machines, each with specific suitability based on their input and output particle sizes, capacity, and energy efficiency. Comminution equipment can be categorized by different loading mechanisms.

In mining, primary crushing often involves jaw crushers, gyratory crushers, or cone crushers, each with distinct advantages and limitations. While gyratory and cone crushers share similarities, jaw crushers operate differently, catering to specific ore types and mining scales. Other examples of comminution equipment are impact crushers, autogenous mills, and ball mills, each employing unique loading mechanisms such as impact or abrasion. However, the focus for this research remains on the compression loading mechanisms prevalent in jaw, gyratory, and cone crushers.

Operational parameters also play a crucial role on the crusher performance. Different studies define functions determining critical characteristics like operation speed, capacity, and power consumption. From all studied models, Rose and English's models are acknowledged for their accuracy in considering various variables. [2]

Key relationships derived from these studies, such as the impact of throw, critical speed, gap size, inclination angle, nip angle, set size, and pressure on capacity and power consumption, provide crucial insights. These relationships serve as a basis for setting up simulation and calibration experiments, aligning the thesis's findings with established research.

## Tavares' breakage model

DEM plays a crucial role in simulating the motion and interaction of particles, especially in scenarios involving bulk material handling and size reduction procedures [3], [4]. The software's applicability is expanding, notably in simulating particle breakage behavior. Professor Luis Marcelo Marques Tavares' breakage model [5], integrated into Rocky DEM and Altair EDEM, stands as a testament to DEM's importance. Developed from his extensive research, this model accurately captures fracture behavior and stress accumulation in brittle materials. By employing the Laguerre-Voronoi tessellation algorithm and probabilistic relations, DEM facilitates realistic simulations of particle breakage events, preserving mass and volume. Tavares' model defines critical parameters, such as particle-specific fracture energy, which is pivotal in understanding the relationship between particle size distribution and fracture energy. This foundational work enhances the accuracy of particle breakage representations in DEM simulations. Tavares' breakage model consists of the following formulas:

$$E_{50} = E_{\infty} * (1 + (\frac{d_0}{d_j})^{\phi}) \tag{1}$$

Equation 1 highlights that the median fracture energy is influenced by both the material properties represented by $E_{\infty}$ and the particle size distribution characterized by $d_0$ and $d_j$. It provides a quantitative understanding of how fracture energy varies with particle size.

$$P_0(E_{CS}) = \frac{1}{2} * (1 + erf(\frac{ln(E^*) - ln(E_{50})}{\sqrt{2 * \sigma}}) \tag{2}$$

Equation 2 calculates the probability that a particle will fracture when subjected to a specific contact energy $E_{CS}$. It utilizes the error function to standardize the calculation based on the difference between the natural logarithms of the specific breakage energy $E^*$ and of the 50% breakage energy $E_{50}$, divided by the square root of twice the standard deviation ($\sigma$) of the fracture energy distribution. It therefore captures the probabilistic nature of particle breakage, considering both the median fracture energy and the variability in fracture energies across particles. It provides a quantitative measure of the likelihood of particle fracture under given contact energies.

$$E^* = \frac{E_{MAX} * E_T}{E_{MAX} - E_T} \tag{3}$$

Equation 3 computes $E^*$ based on $E_{MAX}$ and $E_T$, representing the interplay between the maximum fracture energy and the specific fracture energy of the particle. As $E_T$ approaches $E_{MAX}$, $E^*$ increases, indicating that particles with higher specific fracture energies require more energy to fracture. Conversely, as $E_T$ decreases, $E^*$ decreases accordingly.

As a result, equation 3 allows for the determination of the energy threshold necessary to induce particle fracture, considering the material-specific fracture energy and the distribution characteristics of fracture energies. It facilitates the accurate representation of particle breakage behavior in DEM simulations by incorporating these energy thresholds into the modeling process.

$$D = (\frac{2 * \gamma}{2 * \gamma - 5 * D + 5} * \frac{E_{CS}}{E_T})^{\frac{2 * \gamma}{5}} \tag{4}$$

Equation 4 describes how damage accumulates in a particle as a result of exposure to contact specific energy ($E_{CS}$) that does not lead to immediate fracture. The sustained damage ($D$) is influenced by the ratio of $E_{CS}$ to $E_T$, where higher ratios result in greater damage accumulation. The term $\frac{2 * \gamma}{2 * \gamma - 5 * D + 5}$ acts as a scaling factor, adjusting the rate of damage accumulation based on the current damage level.

Equation 4 provides insights into the progressive deterioration of particle strength over time due to repeated loading and contact with other particles or surfaces. It allows for the modeling of particle behavior under sustained mechanical stress, contributing to the accurate representation of particle breakage phenomena in DEM simulations.

$$E_{NEW} = E_{OLD} * (1 - D) \tag{5}$$

Equation 5 adjusts the original mass-specific fracture energy ($E_{OLD}$) based on the level of sustained damage ($D$). As damage accumulates in the particle, reducing its structural integrity, the new fracture energy ($E_{NEW}$) decreases proportionally. Specifically, the equation calculates $E_{NEW}$ by multiplying $E_{OLD}$ by the complement of the sustained damage fraction (1 - $D$).

This relationship reflects how the particle's susceptibility to fracture increases as it sustains damage over time due to mechanical loading. By updating the fracture energy accordingly, the model accounts for the evolving mechanical properties of the particle.

$$t_{10} = A*(1-e^{-b*E_{CS}}) \tag{6}$$

Equation 6 describes how the proportion of material passing through a specific screen size ($t_{10}$) is influenced by the specific comminution energy ($E_{CS}$). As the comminution energy increases, more material is reduced to sizes smaller than one-tenth of the original particle size, resulting in a higher value of $t_{10}$.

The exponential term $e^{-b*E_{CS}}$ quantifies the reduction in particle size due to the comminution energy, with higher values of $E_{CS}$ leading to a greater reduction in particle size and consequently, a higher proportion of material passing through the specified screen size.

This equation provides valuable insights into the relationship between comminution energy and particle size distribution, improving the fidelity of particle fracture depiction within DEM simulations.

In summary, the equations outlined provide a fundamental understanding of Tavares' breakage model and its relevance in studying comminution processes. While they offer valuable insights into particle breakage dynamics, their practical application depends on validation against real-world data. Continuous refinement is necessary to address the complexities of various materials and operational conditions. These equations find practical utility in simulation software like EDEM, enabling accurate modeling of breakage interactions in granular systems.

## Breakage model implementation in DEM

The Discrete Element Method (DEM) algorithm involves several steps to simulate particle interactions within a defined geometry. First, the user specifies particle properties like shape, size distribution, and material properties such as density and Young's modulus. Then, the geometry where interactions occur is defined, potentially imported from CAD software. Simplifying the geometry can reduce simulation time. A 'factory', a virtual volume for particle generation, is also defined, allowing users to control particle generation parameters. Plug-in factories can customize particle generation beyond standard options. Next, a suitable contact model is chosen to describe interactions between particles, between particles and geometry, and body forces. This model includes base and friction models, with options for additional models or plug-ins for specific needs. The choice of contact model is informed by evaluating existing models and their pros and cons.

Thorough analysis of various models led to the selection of the Hertz-Mindlin (no slip) model with standard rolling friction and the Tavares URFJ Breakage model, tailored to the specific requirements of particle breakage simulation in EDEM. The Hertz-Mindlin model ensures physical accuracy by calculating contact forces based on particle geometry and material properties, while the Tavares URFJ Breakage model accurately tracks particle fracture behavior. These well-validated models offer an accurate simulation foundation for granular material dynamics.

Simulation settings in DEM software, such as time step and integration methods, play crucial roles in achieving accurate and efficient particle simulations. Balancing computation time with accuracy is essential, often guided by the critical time step and considerations for particle breakage. Integration methods like Euler and Verlet impact both accuracy and computational cost. Longer simulations increase computational demands, emphasizing the importance of data storage intervals. Additionally, CPU-GPU coupling can enhance computational power, ultimately optimizing settings to achieve accurate results within practical constraints.

## Importing the geometry

After converting the SolidWorks files to CAD geometries, they can be imported into EDEM one by one. Each part needs to be correctly positioned relative to each other, with possible translations and rotations. To prevent particles from escaping during the breakage process, a virtual funnel is added above the axis and casing, similar to the Moditec Goliath Plus 2 granulator.

In Figure 3, the rotating axis is shown as a cylinder without teeth to save computational resources, as the teeth do not significantly affect the breakage performance. In DEM simulation, it is important to balance capturing essential features and maintaining computational efficiency. Therefore, the rotating axis has been simplified, leaving a small gap between the axis and the fixed geometry to allow small particles to exit the simulation environment.

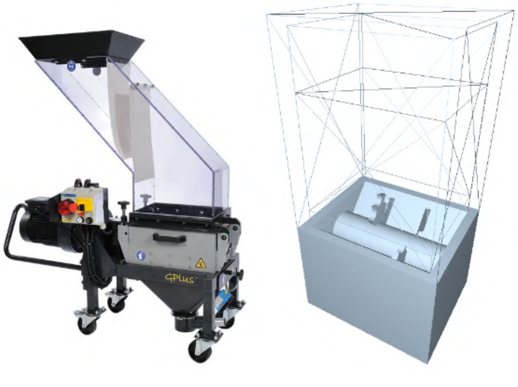

**Fig. 3.** Granulator geometry imported in EDEM

## Results

The results will be divided into three parts. The first part will assess the effect of geometrical parameters on granulating performance by evaluating the four different geometries in terms of the number of generated particles, total mass loss, mass flow at the system exit and particle size distribution at the exit.

In the second part, the performances of these geometries will be compared to select the design with the highest capacity output. In the third part, this optimal geometry will be used to investigate the impact of operational parameters, such as axis rotation speed and filling technique, to determine the most efficient combination of geometry and operational parameters.

The goal is to produce a final product that is uniform in size to minimize clogging during the injection molding process. Since maintaining a single size during the granulation process is not feasible, the threshold is set for particles with a diameter of 3 [mm] $\leq$ d $\leq$ 5 [mm] as desired, while particles with d < 3 [mm] are considered dust and are therefore undesirable. Figure 4 illustrates the difference between uniformly shaped pellets and dusty granulate.

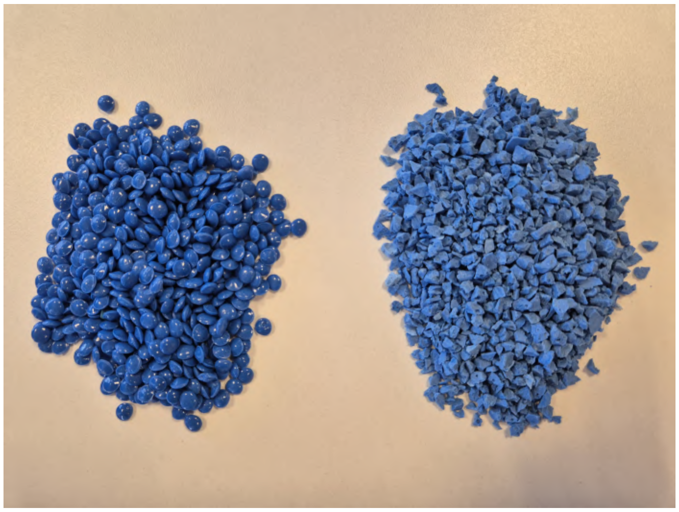

**Fig. 4.** Uniformly shaped pellets (left) and granulate (right)

Figure 5 shows the number of particles generated across different geometries. A simultaneous filling principle with full rotation speed (3600 [deg/s]) are used as starting conditions.

The configuration with a short axis and three cutting blades produces the most particles, whereas a long axis with three cutting blades yields the fewest. The length of the axis has a more significant impact on particle generation than the number of cutting blades. Specifically, a shorter axis results in more particles being generated. For example, a long axis with three cutting blades produces only 29 % of the particles compared to a short axis with three cutting blades.

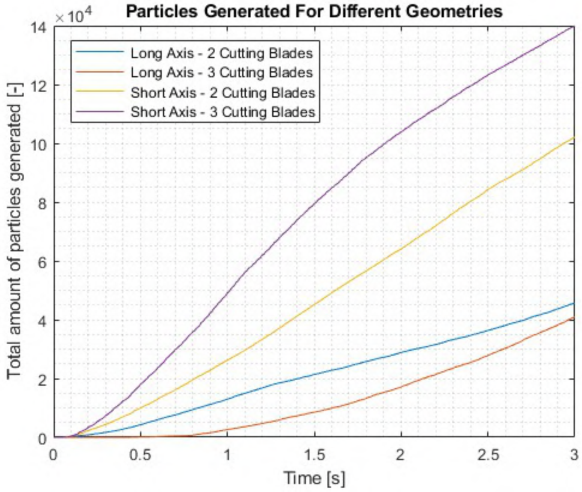

**Fig. 5.** Total amount of generated particles for all geometries

Conversely, a short axis with two cutting blades generates 73 % of the particles compared to a short axis with three cutting blades. Additionally, a long axis with three cutting blades generates 90 % of the particles compared to a long axis with two cutting blades.

The total mass loss in the system follows a similar pattern (figure 6). The same starting conditions are used here. The length of the axis again proves more influential than the number of cutting blades. The geometry with a short axis and three cutting blades performs best, while the long axis with three cutting blades performs the least, losing only 31 % of its mass compared to the best-performing geometry.

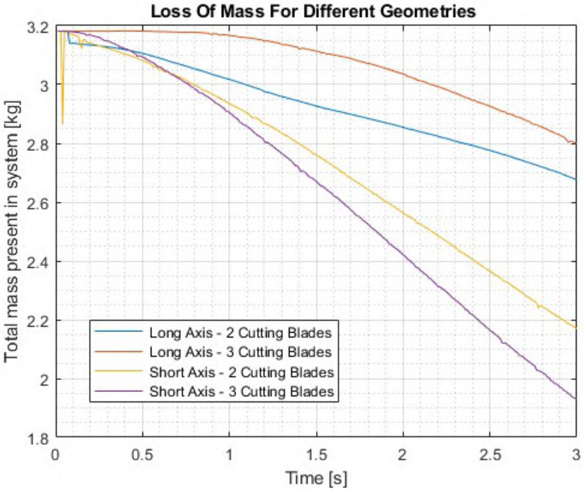

**Fig. 6.** Total loss of mass for all geometries

The operational parameter of rotational speed significantly influences granulating performance, as observed in the study. Figure 7 demonstrates a direct correlation between rotation speed and the total amount of particles generated. Increasing the rotation speed leads to a proportional increase in particle production, attributed to the greater impact force exerted on the input materials by the granulator.

## Discussion

The analysis reveals that fluctuations in the mass flow rate are less pronounced at lower rotational speeds, indicating a more consistent granulator performance. The reduction in impact force at lower speeds results in a slower reduction process but also leads to more uniform particle generation. Conversely, halving the rotation speed results in a significant decrease in particle production due to reduced impact force and less efficient material reduction. This relationship highlights the critical role of rotation speed in determining granulating efficiency. Moreover, the complexity of the reduction process, influenced by factors like material properties and machine design, contributes to the non-linear relationship between rotation speed and particle production, particularly evident at full speed.

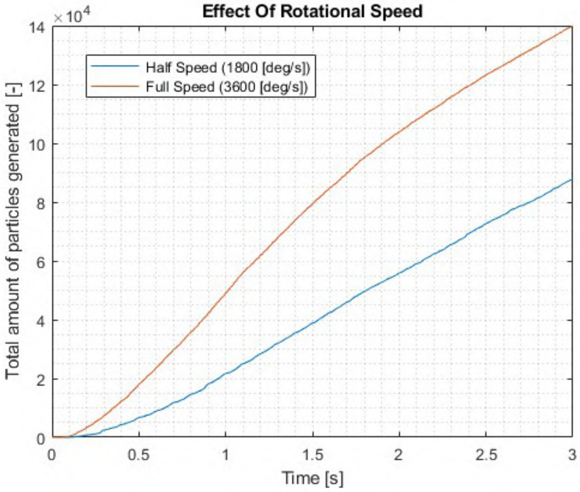

**Fig. 7.** Total amount of particles generated - different speeds

The effect of rotational speed on mass flow rate, as observed in the study, reveals intriguing insights into granulator performance. Figure 8 illustrates how the mass flow rate evolves over time at different rotation speeds for geometry 4 (Short Axis - 3 Cutting Blades). Notably, the mass flow rate increases over time for both half and full speeds, with the latter stabilizing earlier than the former. This disparity in stabilization times is attributed to the higher kinetic energy at higher rotation speeds, accelerating material reduction and thus hastening the attainment of desired particle sizes. Consequently, the mass flow stabilizes faster at higher speeds. Conversely, at half speed, the reduction process is more gradual due to reduced impact force, resulting in a more linear trend in mass flow rate. Overall, the average mass flow rate at half speed is approximately 59 % compared to full speed, highlighting the significant influence of rotational speed on granulator efficiency.

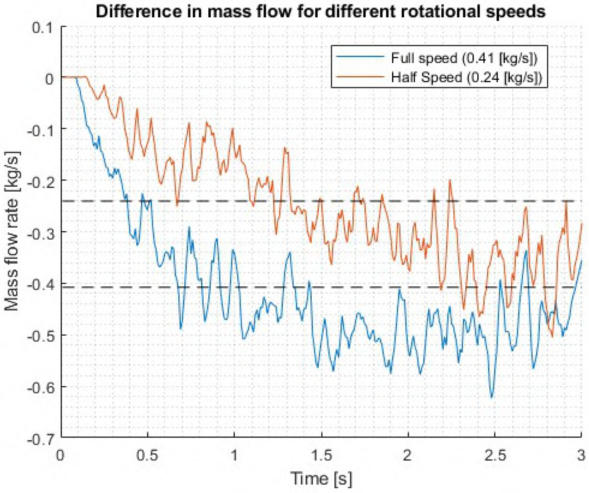

**Fig. 8.** Mass flow rate for different rotation speeds

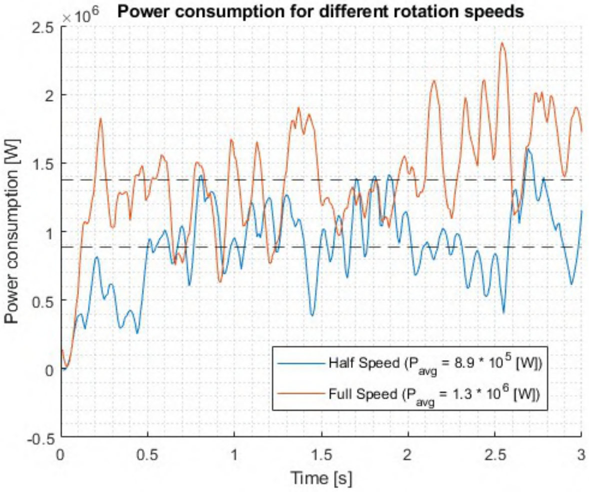

**Fig. 9.** Power consumption for different rotation speeds

The study revealed that rotating the granulator at full speed leads to approximately halving the amount of generated dust compared to half speed rotation (figure 9). However, it is also noted that power consumption at half speed is not halved compared to full speed; specifically, for a mass flow of 59 % compared to full speed, 68 % of the energy is consumed. This indicates that full-speed rotation not only results in a higher output and improved material properties but also proves to be more energy-efficient than half-speed rotation.

The study also exposed the effect of filling principles on the total amount of particles generated for geometry 4 (Short Axis - 3 Cutting Blades). Figure 10 illustrates the comparison between simultaneous and sequential filling techniques. It demonstrates that simultaneous filling results in a more rapid increase in particle generation compared to sequential filling, attributed to the simultaneous addition of more mass at t = 0 $[s]$. However, as sequential filling progresses and additional particles are added, the graphs begin to converge.

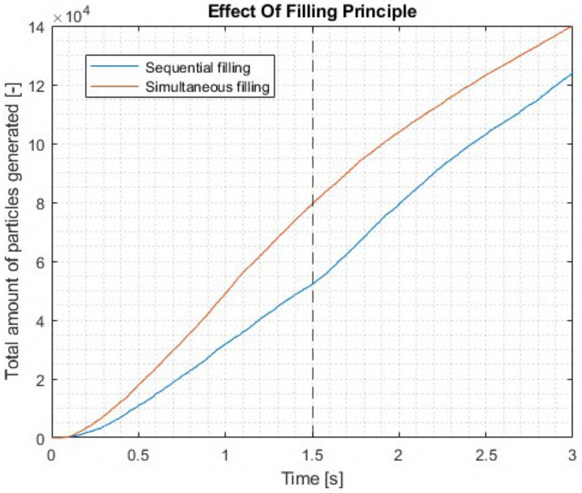

Fig. 10. Total amount of particles generated - different filling techniques

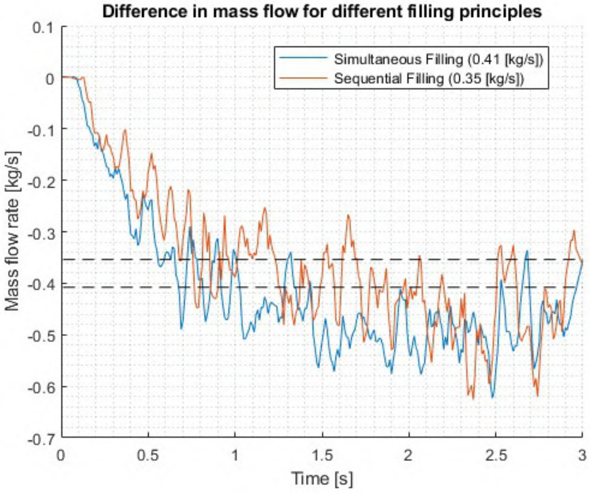

Fig. 11. Mass flow rate for different filling principles

While the simulation only covers 3 seconds, indicating the short-term efficiency of filling techniques, it is noted that after this period, sequential filling results in 89 % of the particles generated compared to simultaneous filling. Thus, while simultaneous filling proves to be more efficient in the short term, the filling technique has less impact on particle generation compared to the rotation speed.

Furthermore, the effect of filling principles on mass flow rate have been delved in to, emphasizing its significance over the sheer number of generated particles. Figure 11 showcases the mass flow rate at the geometry output for both simultaneous and sequential filling techniques. Both techniques exhibit a similar trend of an initially decreasing mass flow rate followed by a stabilization at a relatively constant value. Notably, the average mass flow rate is 0.41 [kg/s] for simultaneous filling and 0.35 [kg/s] for sequential filling, indicating that the mass flow rate using sequential filling is approximately 85 % compared to simultaneous filling.

This underscores the lesser influence of the filling technique compared to the rotation speed on the mass flow rate. Intriguingly, despite only half the mass being present in the system for sequential filling compared to simultaneous filling, the initial mass flow rates for both techniques are nearly equal. This suggests that factors beyond the total mass present in the system, such as particle distribution and movement within the system, contribute to the initial mass flow rates.

## Conlusion

This study investigated the optimization of the granulator's performance at GreenCycl's recycling plant by analyzing various operational and geometrical parameters. By addressing five sub-research questions, it provided a deep understanding of factors affecting granulation performance and product quality.

Key findings include:

- Both loading and breakage mechanisms, influenced by material properties, geometric characteristics, and environmental conditions, are crucial in particle breakage behavior.
- Geometric and operational parameters, such as axis length and the number of cutting blades, significantly impact output and dust generation.
- A shorter axis with three cutting blades produced the highest output but also increased dust generation.
- Higher rotation speeds and simultaneous filling improved output and reduced dust generation.

These results are important for GreenCycl B.V., allowing the company to enhance its granulation process for better output and product quality. This research provides a strong foundation for future optimization efforts, aiding GreenCycl's growth and sustainability.

In conclusion, this study highlights the importance of operational and geometrical parameters in granulation optimization and will guide GreenCycl B.V. in achieving operational excellence and environmental stewardship.

## Recommendations

Based on the findings of this research, several recommendations can be proposed to optimize the performance of the granulator at GreenCycl's recycling plant. Firstly, adopting optimal geometrical configurations entails implementing a granulator design with a shorter axis and three cutting blades to maximize output, despite increased dust generation. Operational parameters should be fine-tuned, including rotation speed and filling technique, to further enhance performance, with higher rotation speeds and simultaneous filling strategies improving output while reducing dust generation. Continuous monitoring and adjustment systems should be established to ensure optimal performance and compliance with environmental regulations. Investment in advanced modeling and simulation tools is crucial for refining design and operational strategies, with ongoing calibration against experimental data ensuring accuracy and reliability. Promoting sustainability and environmental stewardship involves implementing dust mitigation measures and pollution control technologies, exploring opportunities for resource recovery, and waste minimization.

The research maintains a high level of accuracy by focusing on theoretical models. The decision to target specific variables such as calibrating particle breakage models for polypropylene and evaluating the impact of simplifications aims to establish a robust foundation for future practical applications. This approach is crucial for gaining insights into the fundamental mechanisms that influence granulator performance, including the effect of axis patterns on efficiency. By concentrating on these theoretical aspects, a solid groundwork is laid for future research aimed at practical implementations and optimizations in industrial settings. This model incorporates many simplifications, the effects of which should be demonstrated in future research. These simplifications are necessary to streamline the theoretical framework, yet their impact on the accuracy and applicability of the results remains a critical area for further investigation.

Additionally, future research should investigate additional operational parameters and incorporate real-time monitoring and control systems within the granulator to enable continuous optimization and adaptive control. Further refinement and validation of advanced particle breakage models, along with addressing uncertainties and variability, refining coefficients of restitution, static friction, and rolling friction parameters are also recommended for enhanced performance and realism in simulations.

## Bibliography

[1] Van Straten, B., Van der Heiden, D.R., Robertson, P.D., Riekwel, C., Jansen, F.W., Van der Elst, M., & Horeman, T. (2021). Surgical waste reprocessing: Injection molding using recycled blue wrapping paper from the operating room. Journal of Cleaner Production, 322.

[2] Rose, H.E., & English, J.E. (1967). Transactions of the Institution of Mining and Metallurgy, 76, C32.

[3] Altair Engineering Inc. (2022). Tavares Breakage Model. In EDEM 2022.1 Release Highlights. Retrieved from Altair Community.

[4] Schott, D., Mohajeri, J., Jovanova, J., Lommen, S., & de Kluijver, W. (2021). "Design framework for DEM-supported prototyping of grabs including full-scale validation." Journal of Terramechanics, 96, 29-43. doi:10.1016/j.jterra.2021.04.003.

[5] Tavares, L.M. (2009). Modeling Comminution Processes. University of Rio de Janeiro.

# B Contact Models

## B.1 Contact base models

When using DEM software (in the following chapter specifically EDEM), the user can chose between six different types of base contact models for multi-spherical and sphero-cylindrical particle shapes:

- Hertz-Mindlin (no-slip)
- Hertz-Mindlin with JKR
- Hertz-Mindlin with JKR V2
- Hysteretic Spring
- Linear Spring
- Edingburgh Elasto-Plastic Adhesion

### Hertz-Mindlin (no-slip)

The Hertz-Mindlin (no-slip) is the default contact model used in EDEM, since it allows for accurate and efficient calculation of forces. It is a non-linear elastic model and is thus well suited to model non-cohesive interactions. The model consists of a spring force (caused by particle stiffness), a damping force and a friction coefficient. The forces consist of two components. The normal component is based on the Hertzian contact theory and the tangential force is based on the the contact theory of Mindlin-Deresiewicz. Both forces are being damped with a damping coefficient that is dependent on the coefficient of restitution (i.e. the ratio of the final to initial relative speed between two particles after collision). The tangential friction force follows the Coulomb law of friction model. The rolling friction is implemented as the contact independent directional constant torque model. The model tends to produce the most accurate results, but takes more computational time due to smaller time steps being necessary.

The model uses the following formulas to determine the normal force and tangential force acting on the particles:

$$F_N = \frac{4}{3} * E_{EFF} * \sqrt{R^*} * \delta_N^{\frac{3}{2}} \tag{83}$$

$F_N$ = normal force $[N]$
$E_{EFF}$ = effective Young's modulus $[N/m^2]$
$R^*$ = effective radius $[m]$
$\delta_N$ = normal displacement $[m]$

$$F_T = -S_T * \delta_T \tag{84}$$

$F_T$ = tangential force $[N]$
$S_T$ = tangential stiffness $[N/m]$
$\delta_T$ = tangential displacement $[m]$

### Hertz-Mindlin with JKR

Hertz-Mindlin with JKR (Johnson-Kendall-Roberts) is a cohesion contact model that allows users to model strongly adhesive systems, such as dry powders or wet materials, and takes the impact of Van der Waals forces inside the contact zone into consideration. The implementation of the normal elastic contact force is based on the Johnson-Kendall-Roberts theory. Simplified DEM simulations make use of a linear contact model where a constant spring stiffness is applied to all contacts. However, in order to increase accuracy, many researchers use a Hertzian contact model. This model uses a non-linear force deformation relationship at the contacts to account for the variation in contact area with contact force.

### Hertz-Mindlin with JKR V2

Depending on the kind of bond created, there are various ways in which particles can stick to one another. Van der Waals forces become substantial for very small particles (less than 100 $[nm]$), and particles have a propensity to stick together. When estimating the contact forces acting on elastic and adhesive particles, Johnson-Kendal-Roberts theory of adhesion, often known as the JKR Model, makes the assumption that the attractive forces are short-range. The JKR model has been used in several researches on numerous distinct particle systems.

However, the majority of the researches make use of a condensed form of the JKR model that depends on the surface energies of the interacting particles as well as for situations where materials of the same kind are involved. The Hertz-Mindlin with JKR Version 2 (JKR V2) model used in EDEM accurately applies the JKR theory and captures the behavior of different materials. It applies to contacts involving very small particles because it determines the additional work needed to break the contact after physical detachment of the particles. The model can be used for both elastic and adhesive systems.

### Hysteretic spring

Calculation of the Hysteretic Spring normal force is based on the Walton-Braun theory. When plastic deformation behaviors are incorporated into the contact mechanics equations using the hysteretic spring contact model, particles behave elastically up to a predetermined stress. The particles react as though they are undergoing plastic deformation once this tension is exceeded. As a result, significant overlaps are possible without excessive forces acting on them, indicating a compressible material.

### Linear spring

The work of Cundall and Strack served as the foundation for the damped linear spring contact force model. A dashpot with a coefficient of c is parallel to a linear spring with a stiffness of k. A mechanical device called a dashpot, commonly referred to as a damper, uses viscous friction to oppose motion. The resulting force, which works in the opposite direction and is proportionate to the velocity, slows the motion and savors energy. A dashpot is commonly seen in combination with a spring. The parameters needed for this model are the spring stiffness and the dashpot coefficient. It is customary to estimate the spring stiffness and determine the dashpot coefficient based on this stiffness. Then, using the spring stiffness, the simulation time step is estimated. The normal force between two particles, $F_N$, has the following definition:

$$F_N = K_N * \delta_N + C_N * \dot{\delta_N} \tag{85}$$

$F_N$ = normal force $[N]$
$K_N$ = normal stiffness $[N/m]$
$\delta_N$ = normal displacement $[m]$
$C_N$ = normal damping coefficient $[N * s/m]$
$\dot{\delta_N}$ = time derivative of normal displacement $[m/s]$

The tangential force is defined as:

$$F_T = min(K_T * \delta_T + C_T * \dot{\delta_T}, \mu * F_N) \tag{86}$$

$F_T$ = tangential force $[N]$
$K_T$ = tangential stiffness $[N/m]$
$\delta_T$ = tangential displacement $[m]$
$C_T$ = tangential damping coefficient $[N * s/m]$
$\dot{\delta}_T$ = time derivative of tangential displacement $[m/s]$
$\mu$ = coefficient of friction $[-]$

There is no general agreement upon the perfect contact model. Due to minimal computational costs, the linear spring model is simpler than the Hertz-Mindlin model. However, energy dissipation is poor in systems with small relative velocities, and the contact force in both models is discontinuous at the first and last points of contact. A higher force is obtained for the same time step in a Hertz-Mindlin model than in a linear spring model for the same stiffness. Therefore, a linear spring contact model can be employed with a bigger time step.

### Edingburgh Elasto-Plastic Adhesion

The Edinburgh Elasto-Plastic Adhesion Model (EEPA) is able to capture the most important characteristics and history dependence of cohesive particles. The model uses a non-linear hysteretic spring model to capture the elastic to plastic contact deformation. Furthermore, an adhesive force is used which is a function of the plastic contact deformation. The model can be used in both linear and non-linear modes. The material characteristics of cohesive solids are dependent on the material stress before consolidation (i.e. a gradual change in volume due to a change in pressure).

For polyhedral particles, the following contact models can be used:

- Hertz-Mindlin Nassauer-Kuna
- Hertz-Mindlin Effective
- Volume Spring Model

The polyhedral particle contact models will be disregarded for this study, as the Tavares UFRJ Breakage Model is not yet able to perform calculations with non-spherical particle shapes.

## B.2 Contact friction models

The resistive force that slows down the speed of a rolling object is known as rolling friction. It is advisable for most simulations to include a rolling friction component to account for the materials resistance to rolling since rotational resistance and energy loss during rotation are substantial. Only one rolling friction model can be applied to a single simulation. Solely multi-sphere models can use rolling friction models. For polyhedral models, spinning friction should be added instead.

### B.2.1 Contact models voor multi-sphere particles

For multi-sphere particles, the following friction models can be used:

- Standard Rolling Friction
- Type C Rolling Friction
- RVD Rolling Friction (Deprecated)

**Standard Rolling Friction**

In simulations where rolling friction is significant, rolling friction is taken into consideration by adding a torque to the contacting surfaces. This torque can be described by the following standard formula:

$$\tau_i = -\mu_R * F_N * R_i * \omega_i \tag{87}$$

$\tau_i$ = torque $[Nm]$
$\mu_R$ = rolling friction coefficient $[-]$
$F_N$ = normal force $[N]$
$R_i$ = distance from contact point to center of mass of rolling object $[m]$
$\omega_i$ = angular velocity at contact point $[rad/s]$

**Type C Rolling Friction**

By integrating a non-viscous element in the damping torque equation, the Type C rolling friction model developed by Ai differs from the traditional EDEM rolling friction model. A non-viscous damping torque vector plus a viscous damping torque vector make up the total damping torque vector in this case. The relationship between the rolling stiffness and the relative particle rotation angle determines the non-viscous damping torque vector. The viscous damping torque will only be applied when the magnitude of the non-viscous torque falls below a specific threshold. The use of Type C rolling friction may produce a more physically accurate behavior and increased stability of the EDEM model in situations where significant non-viscous rolling resistance is anticipated at particle contacts, such as when contact forces are high or the modeled material contains mostly angular particles.

**RVD Rolling Friction**

An alternate of rolling friction calculation to the standard EDEM Rolling Friction model is the RVD (Relative Velocity Dependent) rolling friction model. According to Zhou, the rolling friction in this model is influenced by the relative rotational velocity of two elements in contact. By exerting a constant force on the contacting surfaces, this contact model takes rolling friction into consideration. The torque is determined by the relative rotational velocities of the two particles that are in contact.

With one exception in the way the relative rotational velocities of two elements in contact are calculated, this RVD Rolling Friction model is presented as a 3D generalization of the "Type A: Directional Constant Torque" model type discussed in the paper of Ai. In contrast to Ai, where the relative rotational velocity is tracked from the point of contact, the EDEM RVD Rolling Friction model calculates the relative rotational velocity from the values of the instantaneous rotational velocities of two elements in contact. Without increasing the computing cost, this implementation detail ensures proper functionality in three dimensions.

### B.2.2 Contact models for polyhedral particles

**Spinning Friction**

The friction that develops if a particle face rotates against another particle or geometry is taken into account using the concept of spinning friction. Calculating the contact area is necessary in order to determine the torque acting on the particles. This calculation is done, using the following formula which takes into account an effective disk radius:

$$M = \frac{2}{3} * \mu * F_N * R_{DISK} \tag{88}$$

$M$ = moment of torque $[Nm]$
$\mu$ = coefficient of friction $[-]$
$R_{DISK}$ = effective disk radius $[m]$

When the contact is approximated as a disk with an area equal to the typical area of the overlap region, the effective disk radius is obtained. This relation between normal area of the overlap region and effective disk radius is given by the following relation:

$$R_{DISK} = \sqrt{\frac{A_{CONTACT}}{\pi}} \tag{89}$$

$A_{CONTACT}$ = normal area of overlap region $[m^2]$

The torque acts in the opposite direction of the normal portion of the relative angular velocity. To prevent oscillatory behavior when the angular velocity is low, a limit is given to this torque. This is accomplished by identifying the torque that, in a single time step, would entirely cancel out the angular velocity.

### B.2.3 Additional contact models

DEM software also has the option to add additional contact models for the simulation. A base model, which might be one of the built-in models or a unique API model, is necessary when using these optional models. However, some of the models are restricted to Sphero-Cylinder (cylindrical shape with rounded ends) and Multi-Sphere simulations. The following models can be added:

- Archard Wear
- Relative Wear
- Oka Wear
- Bonding (legacy) (Deprecated)
- Bonding V2
- Linear Cohesion V2
- Heat Conduction
- Electrostatics
- Tribocharging
- Spray Coating
- Tavares UFRJ Breakage

**Archard Wear**

The Archard Wear model adds an estimation of wear depth for geometry surfaces to any base model. The model follows from the work by John F. Archard, and it makes use of the notion that the frictional work done by particles moving over a surface will be proportional to the amount of material removed from the surface.

**Relative Wear**

The Relative Wear model helps to pinpoint areas of high impact (normal) and abrasive (tangential) wear on the machinery. It is estimated using the velocities and forces that exist between the machinery and the bulk material. One can use the data from this model to identify the areas where wear is occurring. While the model is able to give numerical numbers to compare between two or more design iterations, it does not explicitly calculate the rate of material removal. Normal Cumulative Contact Energy, Tangential Cumulative Contact Energy, Normal Cumulative Force, and Tangential Cumulative Force are the four relative wear properties. The total energy caused by a substance impacting or sliding is measured by the normal and tangential energy. The chosen time step will affect the tangential cumulative force. The cumulative force increases with decreasing time steps. Because the size of each element is not taken into account by the Relative Wear model, a wide range in mesh sizing may result in astounding outcomes.

### Oka Wear

The Impact Wear model adds the ability to estimate the depth of erosion for geometric surfaces caused by particle impacts to any base model. The work of Oka and Yoshida is the foundation of this model. When foreign objects hit the equipment surfaces, erosive wear occurs. The Oka wear model can be used to simulate this form of wear since it predicts the volume of material removed as a result of particle impact as a function of particle size, impact velocity, and impact angle. The model only needs the worn material's Vicker's hardness and an empirical wear constant as input parameters. Similarly to the Archard wear model, the findings in DEM software are reported in terms of wear depth on geometry mesh elements.

### Bonding (Legacy) (Deprecated)

Spheres are connected using the bonding contact model. At the beginning of the formation process, bonds are formed between particles. The Bonding contact model can be used to join particles with a 'glue' bond of a defined size. Up to a maximum normal and tangential shear stress, this bond can withstand normal and tangential movement before it fractures. The particles then engage in hard sphere interactions. This model is based on the work of Potyondy and Cundall. Especially when simulation constructions made of rock and concrete, this model is insightful.

Bonds are formed according the bond parameters. Once the bond time has elapsed, no further bonds will be established. This only happens once per simulation. The contact radius should be adjusted to be greater than the actual radius of the spheres since the bonds involved in this model can still function even when the particles are no longer physically in contact. This model is restricted to be used exclusively among particle to particle interactions.

Both the original and the modified bonding model are available in DEM software. The original (legacy) model is marked as deprecated to be removed in a later version, because it is not GPU-compatible. Bonding V2, an improved model that is GPU-compatible, has been added. The Bonding V2 model has more recent physics capabilities than the original Bonded model.

### Bonding V2

Based on the original Bonding physics model, Bonding V2 is an upgraded GPU-compatible model. Bonds are created based on two methods: 'current time' or 'fixed time'. While bonded materials can be created dynamically in the present (current time method), they can also be created at a single user-defined time in fixed time (fixed time method).

Similar to the bonding legacy model, bonds are formed according the bond parameters. Also in this model, once the bond time has elapsed, no further bonds will be established. This only happens once per simulation. Identical to the bonding legacy model, the contact radius should be adjusted to be greater than the actual radius of the spheres since the bonds involved in this model can still function even when the particles are no longer physically in contact. This model is also restricted to be used exclusively among particle to particle interactions. One should note that, using this model, the ends of the sphero-cylinders cannot yet physically overlap. Therefore there must be a tiny space between each cylinder in the bonded structure.

### Linear Cohesion V2

Cohesion refers to the affinity of particles to adhere to each other. In the past, a model was developed to map the effect of cohesion. This model has been added as an additional model in DEM software. However, the model offered room for improvement. Therefore, an updated version was launched: the Linear Cohesion V2 model. This model is an enhancement over the Linear Cohesion model due to its improved performance for non-uniform particle size distributions. Similar to the Linear Cohesion model, the Linear Cohesion V2 model modifies the Base Contact Model by adding a normal cohesion force.

### Heat Conduction

The Heat Conduction model uses the individual temperature of particles together with their amount of overlap to calculate the heat flux. The heat flux is the amount of energy flow per unit area per unit time. The Heat Conduction model is able to calculate the heat flux of both particle to particle and particle to geometry interactions. The Heat Conduction model must be used together with the Update Temperature particle body force to ensure the function of the heat conduction algorithm. Convective heat transmission predominates in simulations of the dilute phase, and conduction between the particles or the wall can be disregarded. However, in dense phase, particle interactions are important enough that conductive heat transmission must be considered. An external heat source may be included because of the Temperature Update particle body force. Based on the heat flux predicted in the contact model and a known external heat flux, the temperature of each particle can be determined. Only particles are affected by the computed heat flux. In other words, while the particle temperature will update according to the predicted heat flux, the geometrical temperature will never change.

### Electrostatics

By including an Electrostatics model in the particle body force section, electrostatic forces can be added to the already existing kinematic forces. Electrostatic force, which is force exerted by two electrically charged objects, can be either attracting or repulsive. While opposite charges attract one another, like charges repel one another. To determine the magnitude of the force between two charges, Coulomb's law is being utilized. Coulomb's force is inversely proportional to the distances from the centres of both particles to each other. Therefore the size of a screen must be provided when applying the model. Depending on the value of the charge, a consideration will be made whether or not to include particles in or outside the screen.

### Tribocharging

The Tribocharging model enables one to mimic how a particle's charge changes when it comes into contact with another material. Tribocharging can occur with differing amounts of charge transfer for all solid materials with all contacts including sliding. A saturation charge level is attained for repeated interactions and depends on both charge creation and dissipation processes. Triboelectricity is the primary method for charge creation in the majority of electrostatic discharge (ESD) issues. For each material created in DEM software, the work function (the smallest amount of energy required to remove an electron to infinity from the surface of a given solid) needs to be specified. Tribocharging (triboelectric charging) will occur if the work functions of two materials differ. There will not be a charge transfer if the work functions remain the same. The calculations conducted in the DEM software are based on the work of Greason.

### Spray Coating

The Spray Coating model allows one mass to be added to another mass during contact. When the Spray Coating model is used, the volume of the spray material will also be added to the target particle. The added mass and volume will be distributed evenly over the target particle. After contact, the spray particle will be removed. The spray particles do not exert any force on the target particle or on the geometry. Because DEM software automatically calculates the appropriate timestep based on the smallest particles present, it is wise to determine the timestep manually. As a result, the simulation will not take an unnecessarily lengthy amount of time. Because no force is exerted by the spray particles, it is sufficient to select the correct time step for the target material.

### Tavares URFJ Breakage

The model this paper revolves around is the Tavares UFRJ breakage model. This model was the last to be added to DEM software and is discussed in detail within this paper.

## B.3 Particle body force

Besides the particle to particle and particle to geometry interaction forces, DEM software also offers the possibility to define particle body forces. Particle body forces are forces exerted on particles by the environment, this excludes forces exerted by other particles or by the geometry. When a specific condition is met, such as when particles are in specific places or are moving at a specific speed, a particle body force can be configured to act on the particles. The following particle body force models can be added:

- The Temperature Update model
- The Schiller and Naumann Drag model
- The Morsi and Alexander Drag model
- The Haider & Levenspiel Drag model
- The Ganser Drag model
- The Saffman Lift model
- The Magnus Lift model

**The Temperature Update model**

This built-in model enables the modeling of external heat sources acting on the particles. After calculating all of the heat fluxes, each particle's explicit temperature change over time is updated. The Temperature Update model is not strictly referring to a force. The Temperature Update model has originally been designed and validated using the Hertz-Mindlin Base model. As it completes the computation of heat transport between particles in contact, the Temperature Update model must be used in conjunction with the Hertz-Mindlin with Heat Conduction contact model.

**Drag models**

Drag force is primarily responsible for the motion of particles in practically all particle-laden flows. Therefore, an accurate calculation of this force is required for proper simulation of particle-fluid fluxes. DEM software allows for an inclusion of a desired drag model. One should bear in mind that only one drag model can be used per simulation.

**The Schiller and Naumann Drag model**

The Schiller and Naumann model is used for modelling of drag between fluid phases in a multiphase flow. The drag function f is given as:

$$f = \frac{C_D * Re}{24} \tag{90}$$

$f$ = drag function $[-]$
$C_D$ = drag coefficient $[-]$
$Re$ = Reynolds number $[-]$

When a fluid experiences relative internal movement as a result of various fluid velocities, the ratio of inertial forces to viscous forces is known as the Reynolds number. Schiller and Naumann based their calculations on a relative Reynolds number for the primary phase and secondary phase. The desired drag coefficient is also based on the Reynolds number. An imported velocity vector field or user-defined flow field is necessary for this drag model. One also needs to specify the fluid's density, viscosity, and particle scale factor.

### The Morsi and Alexander Drag model

The Morsi and Alexander Drag model uses the same equation to calculate the drag function as Schiller and Naumann (equation 90). However, drag coefficients will have different relations to the Reynolds number compared to the model of Schiller and Naumann. An imported velocity vector field or user-defined flow field is also necessary for this drag model. Furthermore, one needs to specify the fluid's density, viscosity, and particle scale factor.

### The Haider & Levenspiel Drag model

The work of Haider and Levenspiel is another way of calculating the amount of drag. This model can be used for both spherical and non-spherical particles. The user must define the degree of sphericity. As with the previous two models, a velocity vector field or a user defined flow field need to be imported. Additionally, one must specify the fluid density, viscosity and particle scale factor used.

### The Ganser Drag model

The Ganser Drag model can, like the model of Haider and Levenspiel, also be used for both sperical and non-spherical particles. As with all previously mentioned models, an imported velocity vector field or a user defined flow field need to be imported. Furthermore, the fluid density, viscosity and particle scale factor need to be specified.

### Lift models

The lift force is the force that a flowing gas or liquid exerts on a body perpendicular to the direction of the flow. Lift is generated due to the fluid shear and/or particle rotation. Simulations can contain lift models in addition to the previously defined drag models.

### The Saffman Lift model

The Saffman lift force is produced by the pressure difference on a particle in a non-uniform shear velocity field. The user needs to enter the flow field's density and viscosity. If the particles have been enlarged, the user may also enter the particle scale. In order to calculate the Staffman lift force, a vorticity vector field must be imported to the DEM software. The model additionally needs a user-defined steady state flow field or a velocity field to be applied.

### The Magnus Lift model

Particle rotation is the cause of the Magnus lift force. As with Saffman's lift model, the user needs to enter the flow field's density and viscosity. Furthermore, if the particles have been enlarged, the user may also enter the particle scale. The Field Data Manager must be used to import a vorticity vector field into the DEM software in order to calculate the Magnus Lift force. The model additionally needs a user-defined steady state flow field or a velocity field to be applied. This makes the application of both Saffman's en Magnus's Lift models similar.

It is essential to acknowledge that while the contact models discussed previously may offer valuable insights for particular applications, their relevance to the present research is limited. Consequently, given the constraints imposed by simulation time, the decision has been made to omit their incorporation. This deliberate choice underscores a commitment to optimizing efficiency and relevance within the research framework, thereby judiciously allocating computational resources to areas where their utilization can yield maximal contributions toward realizing the research objectives.

**Environment**

After stating the boundary conditions, the environment can be defined. The user can choose to create temporary boundaries. These boundaries can be linear or cylindrical. An alternative is a dynamic domain. Simulating extensive beds of material is necessary for some applications (e.g. agricultural or off-road), which might lengthen simulation time frames. One of the most sophisticated DEM processing technologies is the Dynamic Domain. The Dynamic Domain technology allows users to concentrate all of their processing resources on where the action is taking place. This is done by generating an active region around equipment pieces, in contrast to conventional DEM tools that need the user to solve all particle connections at all times throughout a simulation. This enables the user to produce enormous beds and quantities of material without raising computing costs.

# C Geometry Design

In this appendix, the four different designed geometries will be explained in more detail. The explanation will begin with the long axis equipped with both two and three cutting blades. Subsequently, the short axis equipped with both two and three cutting blades will be examined. The difference between the long axis and the short axis is the fact that the long axis is 1.5 times larger than the short axis.

## C.1 Long Axis - 2 Cutting Blades

This geometry consists of five parts: three axis sections and two cutting blades. All three axis sections are 150 $[mm]$ long. The diameter of the axis is 91 $[mm]$. This is due to the fact that the opening in the casing without a rotating axis is 101 $[mm]$ in size. To maintain an opening of 5 $[mm]$ on both sides, the axis must therefore have a diameter of 91 $[mm]$. The two cutting blades have a width of 15 $[mm]$. Figure 73a shows a render of the assembly, and figure 73b depicts a technical drawing with the dimensions of the rotating axis. Both figures were created in SolidWorks.

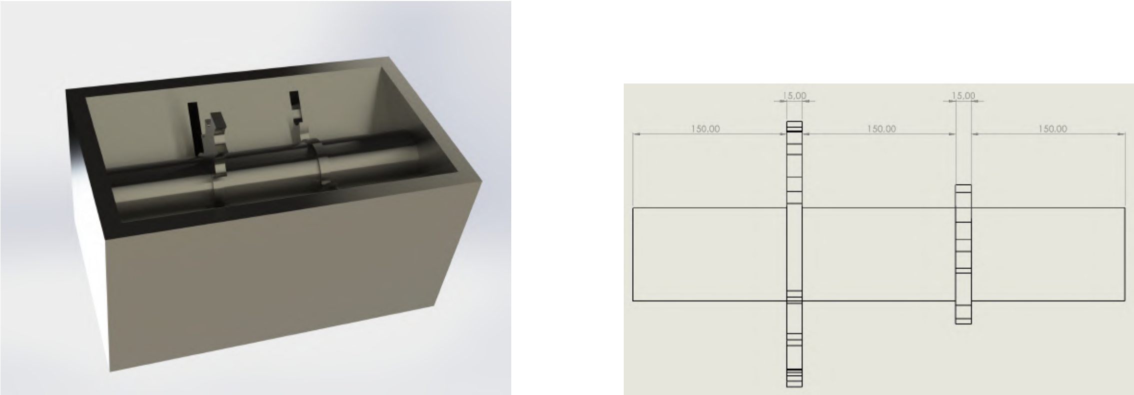

(a) SolidWorks render

(b) Schematic drawing of rotating axis

Figure 73: Long Axis - 2 Cutting Blades

## C.2 Long Axis - 3 Cutting Blades

This geometry consists of seven parts: four axis sections and three cutting blades. The two axis sections in the middle are 150 $[mm]$ long. The two axis sections on the sides are 10 $[mm]$ long. This distance is designed so that particles larger than the thickness of the blade can still be granulated. The diameter of the axis is 91 $[mm]$. The three cutting blades have a width of 15 $[mm]$. Figure 74a shows a render of the assembly, and figure 74b depicts a technical drawing with the dimensions of the rotating axis. Both figures were created in SolidWorks.

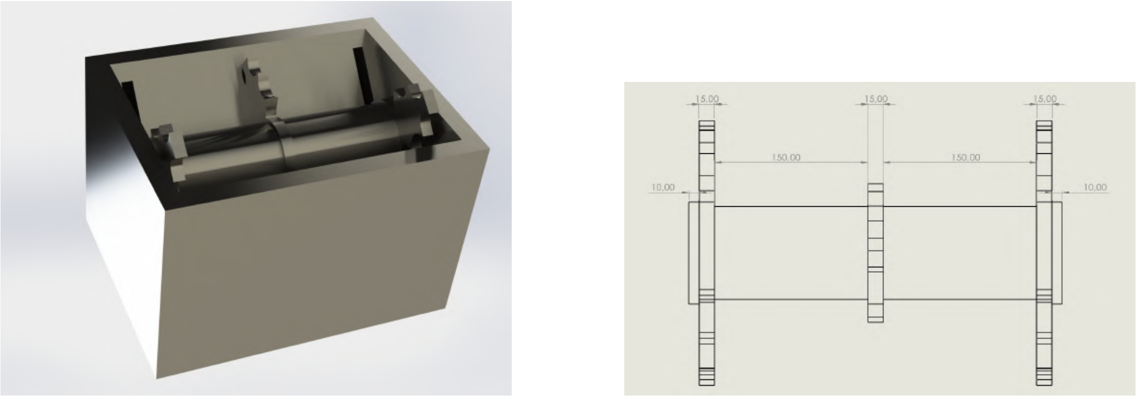

(a) SolidWorks render

(b) Schematic drawing of rotating axis

Figure 74: Long Axis - 3 Cutting Blades

## C.3 Short Axis - 2 Cutting Blades

This geometry consists of five parts: three axis sections and two cutting blades. All three axis sections are 100 $[mm]$ long. The diameter of the axis is 91 $[mm]$. The two cutting blades have a width of 15 $[mm]$. Figure 75a shows a render of the assembly, and figure 75b depicts a technical drawing with the dimensions of the rotating axis. Both figures were created in SolidWorks.

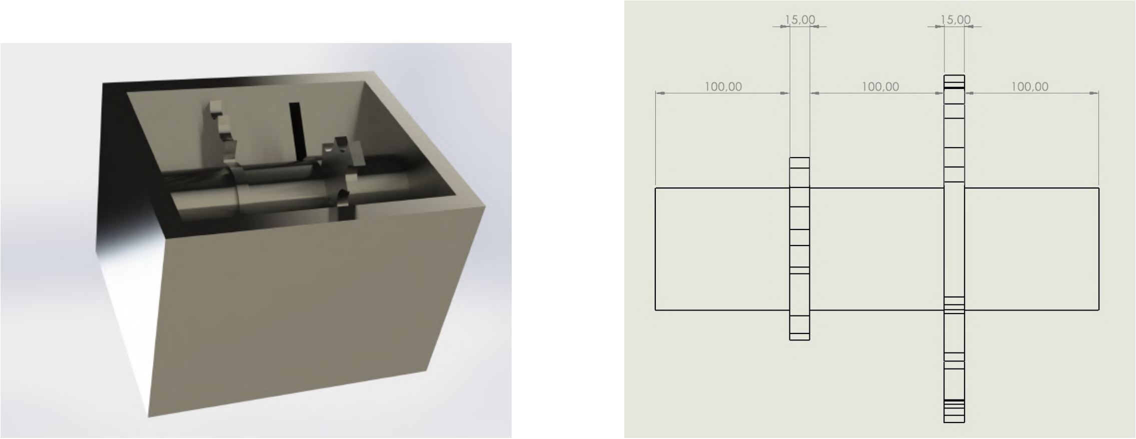

(a) SolidWorks render

(b) Schematic drawing of rotating axis

Figure 75: Short Axis - 2 Cutting Blades

## C.4 Short Axis - 3 Cutting Blades

This geometry consists of seven parts: four axis sections and three cutting blades. The two axis sections in the middle are 100 $[mm]$ long. The two axis sections on the sides are 10 $[mm]$ long. The diameter of the axis is 91 $[mm]$. The two cutting blades have a width of 15 $[mm]$. Figure 76a shows a render of the assembly, and figure 76b depicts a technical drawing with the dimensions of the rotating axis. Both figures were created in SolidWorks.

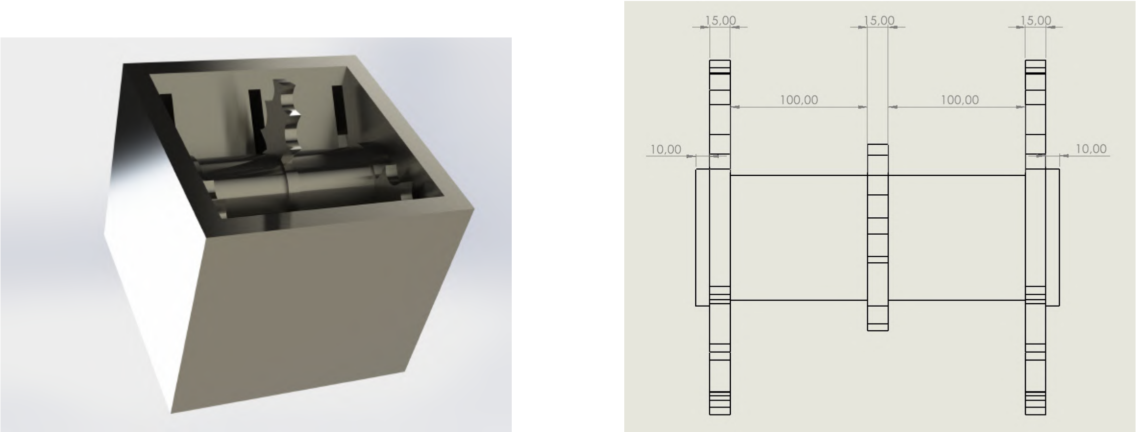

(a) SolidWorks render

(b) Schematic drawing of rotating axis

Figure 76: Short Axis - 3 Cutting Blades

# D Sensors In EDEM

In EDEM, a distinction can be made between different sensors. In this research, two sensors play a primary role: the total mass sensor and the mass flow sensor.

## D.1 Total mass sensor

The total mass sensor provides real-time data on the cumulative mass of particles or objects within a defined region or throughout the entire simulation domain. In this research, the total mass sensor is defined as a cube encompassing the entire geometry. This means that the total mass of all present particles is captured by this total mass sensor.

Based on the decrease in total mass within the system, information can be obtained about the mass flow out of the system. This is done by differentiating the total mass. Using this, the mass flow out of the entire system can be determined. An example of a total mass sensor used in this study is shown in figure 77

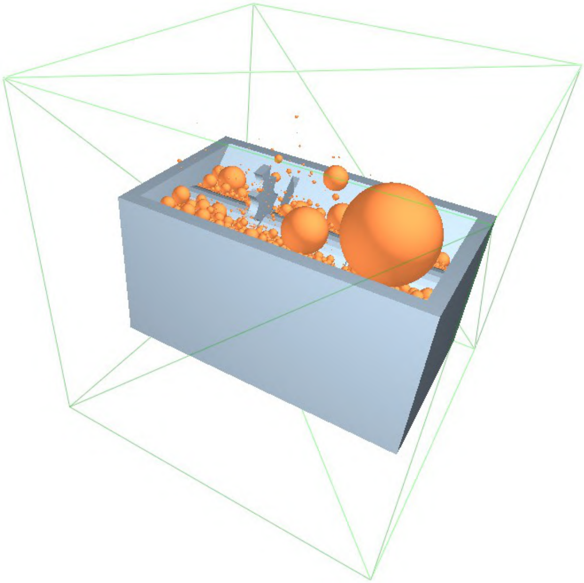

Figure 77: Example of total mass sensor

## D.2 Mass flow sensor

The mass flow sensor is a tool used to measure and analyze the flow rate of materials within a simulation.

In this study, it has been decided to place a mass flow sensor at the bottom of the granulator. After all, this is the location where the particles should fall through after granulation. To determine whether the mass leaving the entire system actually corresponds to the mass exiting the bottom of the granulator, the results of the differentiated total mass and mass flow are compared with each other. An example of a mass flow sensor used in this study is shown in figure 78.

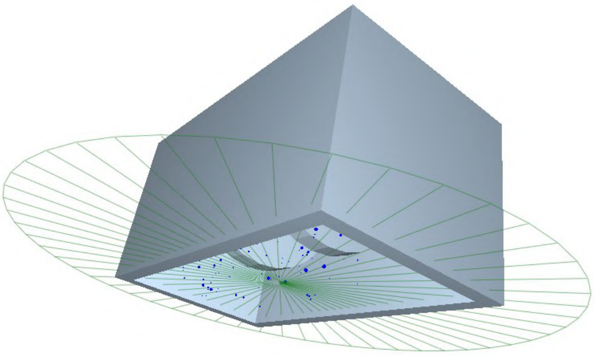

Figure 78: Example of mass flow sensor

# References

[1] Image of jaw crusher, gyratory crusher and cone crusher, https://savree.com/en/encyclopedia/gyratory-crusher.

[2] Roll Crushers. In *Mineral Processing Design and Operations*, pages 169–188. Elsevier, 2016.

[3] Luís Marcelo Tavares. Chapter 1 Breakage of Single Particles: Quasi-Static, 2007.

[4] Tim Napier-Munn. Is progress in energy-efficient comminution doomed? *Minerals Engineering*, 73:1–6, 3 2015.

[5] Parisa Semsari Parapari, Mehdi Parian, and Jan Rosenkranz. Breakage process of mineral processing comminution machines – An approach to liberation. *Advanced Powder Technology*, 31(9):3669–3685, 9 2020.

[6] B A Wills and K Atkinson. SOME OBSERVATIONS ON THE FRACTURE AND LIBERATION OF MINERAL ASSEMBLIES. Technical Report 7, 1993.

[7] Modeling and Simulation of Mineral Processing Systems. Technical report.

[8] X. Ye, S. Gredelj, W. Skinner, and S. R. Grano. Regrinding sulphide minerals - Breakage mechanisms in milling and their influence on surface properties and flotation behaviour. *Powder Technology*, 203(2):133–147, 11 2010.

[9] C B Holt. Powder Technology. 3s (19Sl) 59-63 0 Elaevier Sequoia S.A., Iausanze-Printed in the Netherlands. Technical report.

[10] Bond-F-C-1961-Crushing-and-Grinding-Calculations.

[11] F Milstein, B Farber, K Kim, L Van Den Berg, and W F Schnepple. INFLUENCE OF TEMPERATURE UPON DISLOCATION MOBILITY AND ELASTIC LIMIT OF SINGLE CRYSTAL HgI2 *. Technical report, 1983.

[12] S. Chehreh Chelgani, M. Parian, P. Semsari Parapari, Y. Ghorbani, and J. Rosenkranz. A comparative study on the effects of dry and wet grinding on mineral flotation separation–a review, 9 2019.

[13] Jaw Crusher. In *Mineral Processing Design and Operations*, pages 123–152. Elsevier, 2016.

[14] Hersam EA. Trans AIME 1923;68;463.

[15] Rose HE, English JE. Trans IMM 1967;76:C32.

[16] Taggart AJ. Handbook of mineral dressing. New York: John Wiley; 1945.

[17] Broman J. Eng Mining J June 1984;69.

[18] Kelly EG, Spottiswood DJ. Introduction to mineral processing. Kalgoorlie: Mineral Engineering Services; 1989.

[19] Dejan Todorovic, Maja Trumic, Ljubisa Andric, Vladan Milosevic, and Milan Trumic. A quick method for bond work index approximate value determination. *Physicochemical Problems of Mineral Processing*, 53(1):321–332, 2017.

[20] Lynch AJ. Mineral crushing and grinding circuits. Amsterdam, New York: Elsevier Science Publishing; 1977.

[21] Morrell S, Napier-Munn TJ, Andersen J. In: Kawatra SK, editor. Communition theory and practice. Littleton Colorado: AIME; 1992.

[22] Andersen JS, Napier-Munn TJ. 3rd Mill operators conference, Cobar, Australia; 1988.

[23] Gyratory and Cone Crusher. In *Mineral Processing Design and Operations*, pages 153–168. Elsevier, 2016.

[24] Gauldie K. Engineering, London 1953;(Oct 9):456.

[25] Gauldie K. Engineering, London 1954;(April 30):557.

[26] Mishra SK. Private Commun; 1980.

[27] Hersam EA. Trans AIME 1923;68:463.

[28] Rose HE, English JE. Trans Inst Mining Metallurgy 1967;76:C32.

[29] Motz JC. In: Mular AL, Bhappu RB, editors. Mineral processing and plant design. New York: SME/AIMME; 1980. p. 203–238.

[30] Schönert K. In: Somasundaran P, editor. Advances in mineral processing. New York SME/AIME; 1986. p. 19–31. [Chapter 1].

[31] Schönert K. 4th Tewksbury Symp., Melbourne; 1979. p. 3.1.

[32] Vladimir N. Malyshev. Tribological aspects in friction stir welding and processing. In *Advances in Friction-Stir Welding and Processing*, pages 329–386. Elsevier Ltd, 10 2014.

[33] Wills BA. Mineral processing technology. 2nd ed Oxford, New York Pergamon Press; 1981.

[34] Perry RH, Chilton CH. Chemical engineering handbook. New York 5th ed McGraw-Hill; 1973. p. 8–22.

[35] Otte O. Proc. Third Mill Operators Conf., Australasian Institute of Mining and Metallurgy: Cobar; May, 1988. 131–6.

[36] Schönert K and Knoblock OR, Zement-Kalk-Gipps II, 1984. p. 563.

[37] Beisner K, Gemmer L, Kellerwessel H, Zisselmar. European Patent 0 084 373. 1983.

[38] Battersby M, Kellerwessell H, Oberheuser G. International conf. in extractive metallurgy of gold and base metals. Kalgoorlie: Aus.I.M.M; 26–28 October, 1992. p. 159–65.

[39] Klymowsky R, Patzelt N, Knecht J, Burchardt E. Proc. mineral processing plant design practice and control. SME conf., Vancouver, 1, 2002, p. 636–68.

[40] Morrell S, Lim W, Shi F, Tonda L. In: Kawatra SK, editor. Comminution practices. Littleton: SME/AIME; 1997. p. 117–126.

[41] Seebach M, Knobloch OR. SME annual meeting. Denver, Feb. 1987.

[42] Klymowsky IB, Liu J. In: Kawatra SK, editor. Comminution practice. Littleton: SME/AIME; 1997. p. 99–105. [Chapter 14].

[43] the-principles-of-chemical-engineering-1923-walker-lewis-mcadams_compressed.

[44] Zeki. Berk. *Food process engineering and technology.* Elsevier/Academic Press, 2009.

[45] L M Tavares and R P King. Single-particle fracture under impact loading. Technical report, 1998.

[46] L M Tavares and R P King. Modeling of particle fracture by repeated impacts using continuum damage mechanics. Technical report, 2002.

[47] Cundall, P. A., & Strack, O. D. L. (1979). A discrete numerical model for granular assemblies. Geotechnique, 29(1), 47–65.

[48] Moditec Goliath Plus 2, https://www.moretec.nl/32-producten/randapparatuur.